Conformational behaviour of amphiphilic molecules in aqueous solution and at a water/air interface: computational studies at the molecular level

Philip Michael Anderson

Conformational Behaviour of Amphiphilic Molecules in Aqueous Solution and at a Water/Air Interface: Computational Studies at the Molecular Level

Philip Michael Anderson

Ph.D. Thesis

University of Durham

Chemistry Department

January 2004

Submitted in partial fulfilment of the requirements

for the degree of Doctor of Philosophy

Abstract

Conformational Behaviour of Amphiphilic Molecules in Aqueous Solution and at a Water/Air Interface: Computational Studies at the Molecular Level

Philip Michael Anderson

Previous experimental studies have indicated that the amphiphilic graft copolymer polynorbornene-*g*-poly(ethylene oxide) (PNB-*g*-PEO) undergoes interesting conformational behaviour when placed at a water/air interface. This polymer adopts different conformations depending upon surface concentration, as elucidated through neutron reflectometry measurements. The work in this thesis details the preparation for, and execution of atomistic molecular dynamics simulations of this system at a range of surface concentrations.

Three commonly used water models were assessed for computational expense and accuracy in the reproduction of key experimental properties, particularly density. It was found that the TIP4P water model was the most appropriate, and was therefore used to generate a water/vapour interface configuration.

The OPLS-AA force field was then examined in detail on the basis of *ab initio* structural optimisation calculations on 1,2-dimethoxyethane (DME), a model molecule for poly(ethylene oxide) (PEO). Torsion parameters for the O-C-C-O and C-O-C-C dihedral potentials were fitted to these *ab initio* data in an attempt to obtain a force field capable of reproducing the conformational behaviour of DME in the bulk liquid as measured previously by experiment.

Using this fitted force field, fully atomistic simulations of PNB-*g*-PEO at the water/vapour interface were performed at a range of surface concentrations coinciding with the experimental study. Excellent agreement was found between simulated and experimental neutron reflectivity profiles for low surface concentrations. Agreement at higher concentrations was slightly poorer, but still much better than that obtained in a previous simulation study without explicit water.

Four force fields were then compared in simulations of a PEO chain in aqueous

solution. Dihedral angle analysis was performed on these PEO chains and compared to the behaviour of the PEO side chains in PNB-*g*-PEO. Agreement with conformational populations was confirmed between the two studies, however the frequency of conformational transitions was found to differ significantly between the two sets of simulation.

Declaration

The material contained within this thesis has not previously been submitted for a degree at the University of Durham or any other university. The research within this thesis has been conducted by the author unless indicated otherwise.

Philip Michael Anderson

January 2004

Acknowledgments

There are many people I wish to thank for their help and support during my PhD. The first of these is the Engineering and Physical Sciences Research Council (EPSRC) for the studentship that made this work possible. I also wish to thank EPSRC for the grants which provided the high-powered computers used throughout this study.

I am deeply indebted to my supervisor, Dr. Mark Wilson, whose scientific and computational expertise is second to none. Mark provides an excellent environment in which to work, and as a result, the last three years of research have been an absolute pleasure. I would also like to thank all past members of Mark's research group who have provided helpful input to this project, particularly Dave Earl, Dave Cheung, Lorna Stimson and Jaroslav Ilnytskyi.

Within Durham University, I am grateful to Dr. David Tozer and Prof. Randal Richards for helpful discussions relating to various aspects of this work. Thanks also go to Dr. Lydia Heck, Dr. Karen Brazier, Dr. Duncan Rand and Durham University's Information Technology Service for assistance with computational problems. I gratefully acknowledge M. Imran for the original Lyx thesis template.

I would also like to thank my family for their help and support, particularly Mam, Dad, Grandma and Grandad. Thanks to Helen and Simon for your friendship, as well as amusing Monday evenings watching chinchillas racing around your living room!

Finally, my friends Andrew, Stephen and Barry deserve a mention. Thanks for your friendship and all the crazy discussions.

Every attempt to employ mathematical methods in the study of chemical questions must be considered profoundly irrational and contrary to the spirit of chemistry.... if mathematical analysis should ever hold a prominent place in chemistry – an aberration which is happily almost impossible – it would occasion a rapid and widespread degeneration of that science.

Auguste Comte

If the automobile had followed the same development cycle as the computer, a Rolls-Royce would today cost $100, get a million miles per gallon, and explode once a year, killing everyone inside.

Robert X. Cringely

Contents

List of Figures

List of Tables

Chapter 1

An Introduction to Polymers

1.1 What are Polymers?

Any large molecule exhibiting a regular repeating pattern of atoms and bonds in its structure is classified as a *polymer*.[1] The small repeated sections are known as *monomers*, and a single polymer molecule may be composed of many thousands of these monomer units. Polymeric materials are used today in almost every industry and home; materials such as plastics and rubbers (also known as elastomers) are polymeric in nature.

The wide variety of applications of polymers ensures that we encounter them almost every day of our lives. Polymers are used in such diverse applications as food packaging,[2] vehicle tyres[3,4] and medicine.[5–7] Polymers play a very important role in all aspects of life today.

As well as having diverse physical properties, polymers may also be classified on a molecular level. There are several different types of polymer molecule, including block copolymers, dendritic polymers (dendrimers) and graft copolymers. Copolymers are large molecules, or *macromolecules*, made up of two or more monomer types. A typical random copolymer, for example, would have these monomer units distributed throughout the molecule in a purely random fashion. Block copolymers are rather more ordered, being made up of alternating segments of single monomer type. Graft copolymers are more interesting materials, and are in the simplest cases, composed of two monomer types. One of the monomers generally forms a long chain

known as the *backbone*, and the other monomer forms secondary chains (*side-chains*) which radiate out from this backbone, at branching points. Figure 1.1 shows four common polymer structures.

A key geometric quantity in polymer studies is the (instantaneous) *radius of gyration*, which quantifies the physical extent of a polymer chain in a particular conformation. The radius of gyration, R_g, is defined as

$$R_g = \sqrt{\sum_{i=1}^{n} \frac{S_i^2}{n}}, \tag{1.1}$$

where n is the number of atomic sites in the polymer and S_i^2 is the square of the distance between atomic site i and the centre of mass of the polymer.

Due to thermal fluctuations and molecular collisions, polymer molecules do not remain in any particular conformation for significant periods of time. As a result, experiments are usually restricted to the measurement of the *mean radius of gyration* (time-average *radius of gyration*).

1.2 Hydrophobic, Hydrophilic and Amphiphilic Polymers

Many polymers are classified as hydrophobic, meaning that molecules do not mix well with water. Such polymers are generally composed of hydrogen and carbon, and are therefore non-polar. As a result, these polymers will not engage in favourable non-bonded interactions with polar solvent molecules. Hydrophobic molecules will attempt to avoid water molecules as much as possible, preferring to pack together. Polyethylene (sometimes called polymethylene), shown in figure 1.2, and composed of a chain of methylene units, capped at each end by methyl groups, is a typical hydrophobic polymer.

There are, however, a large number of polar polymeric systems, such as proteins, which contain more electronegative elements. In order to dissolve in, or be miscible with highly polar water molecules, a solute molecule must be able to engage in energetically favourable interactions with the surrounding solvent molecules. Typically,

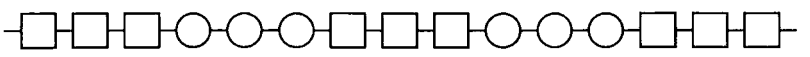

(a) Block copolymer

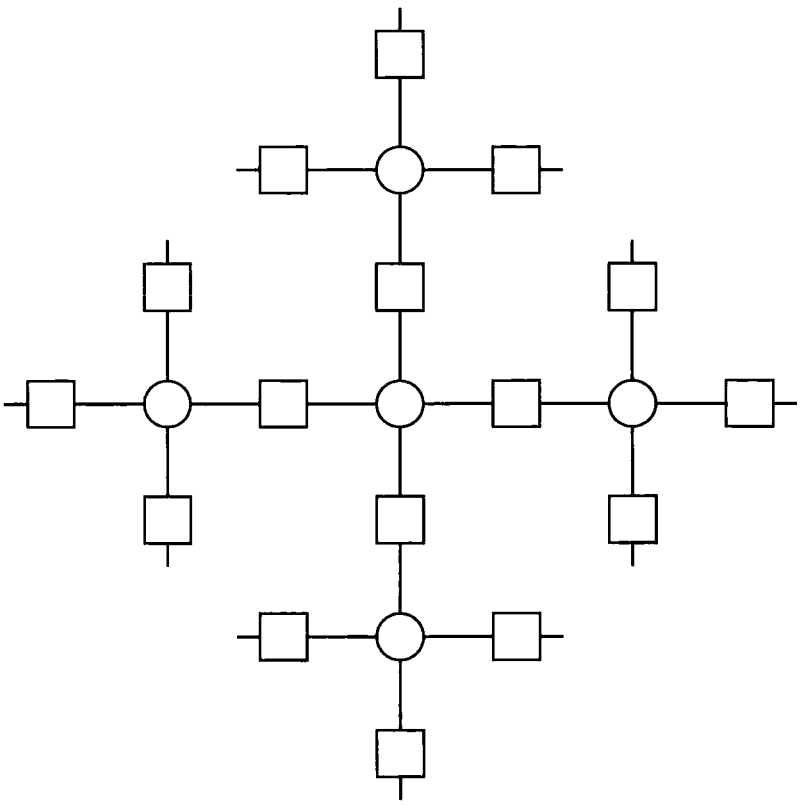

(b) Dendritic polymer (dendrimer)

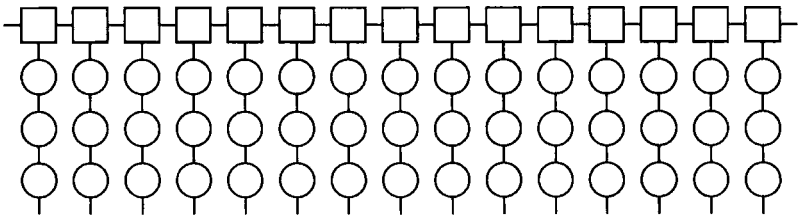

(c) Graft copolymer

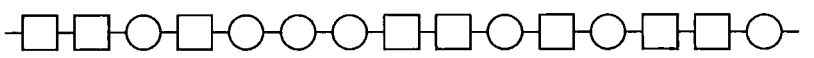

(d) Random copolymer

Figure 1.1: Four common polymer types. Dangling bonds imply continuation of repeat patterns. Squares and circles are chemically distinct repeat units, e.g. ethylene oxide and styrene.

the interaction between the solvent and solute must be at least as energetically and entropically favourable as the solvent-solvent and solute-solute interactions, in order that the network of non-bonded associations present in both groups may be broken up to allow solvation to take place. Any polymer that can interact favourably with, and therefore dissolve in water is labeled hydrophilic. Hydrophilic polymers are based on molecules composed of a more varied set of atoms; such a molecule will likely have greater electrostatic charges on its atoms. One of the most well-known hydrophilic polymers is poly(ethylene oxide) (PEO), and can be seen in figure 1.3. Poly(ethylene oxide) is similar in form to polyethylene, the difference being that every third methylene group has been replaced by a much more electronegative oxygen atom.

In general, if the polymer-solvent interactions are more favourable than the polymer-polymer and solvent-solvent interactions, then the solvent is said to be a *good solvent* for this polymer. If the polymer-polymer and solvent-solvent interactions are more favourable then this solvent is a *poor solvent* for the polymer. A *theta solvent* is one in which the polymer-solvent interactions are equally favourable to the polymer-polymer and solvent-solvent interactions. Thus, a polymer molecule in a good solvent will tend to swell as it allows itself to be fully solvated. A polymer molecule in a poor solvent will reduce in volume, in order to maximise the ratio of polymer-polymer to polymer-solvent interactions.

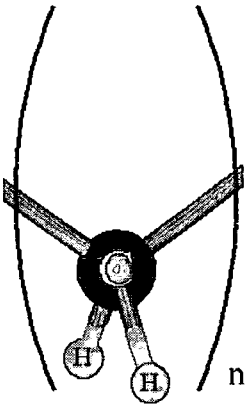

Figure 1.2: Polyethylene, a hydrophobic polymer, is a simple straight chain of methylene units, forming long n-alkane molecules.

Amphiphilic polymers show properties of both hydrophilic and hydrophobic poly-

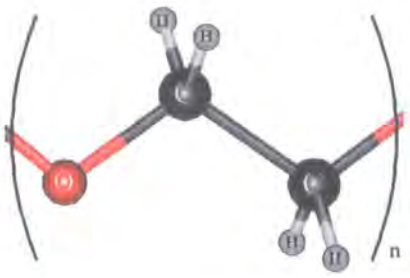

Figure 1.3: Poly(ethylene oxide), a hydrophilic polymer, is made up of a long chain of monomer units composed of one oxygen atom and two methylene groups.

mers. Typically, an amphiphilic polymer will be a copolymer, with some of its monomers hydrophobic and others hydrophilic in nature. A good example of an amphiphilic polymer would be a graft copolymer with a hydrophobic backbone, say polynorbornene, and poly(ethylene oxide) side chains. Such a polymer would display interesting behaviour when placed at a water/air or water/oil interface.[8,9] In this case, the poly(ethylene oxide) side chains will attempt to immerse themselves completely in water to maximise the favourable non-bonded interactions, while the backbone would minimise its energy by avoiding the water (remaining in the air phase) or allowing the oil phase to solvate it. The result is a system where the backbone remains at the surface, while the side chains penetrate into the aqueous phase, as shown in figure 1.4.

Such amphiphilic behaviour is not limited to graft copolymers; block copolymers with at least one hydrophobic and one hydrophilic component will arrange themselves at an hydrophobic/hydrophilic interface in such a way that the various sections of the polymer chain are surrounded by whichever solvent has the most favourable interactions with each particular block.

1.3 Polymers at Interfaces and Tethered Polymers

The behaviour of polymers at interfaces is an important field of study; processes involved in lubrication[10–12] are often polymer-mediated, and of great interest in relation to reducing friction in machines with moving parts. Polymers can also have the opposite effect at an interface, by significantly increasing friction, leading to

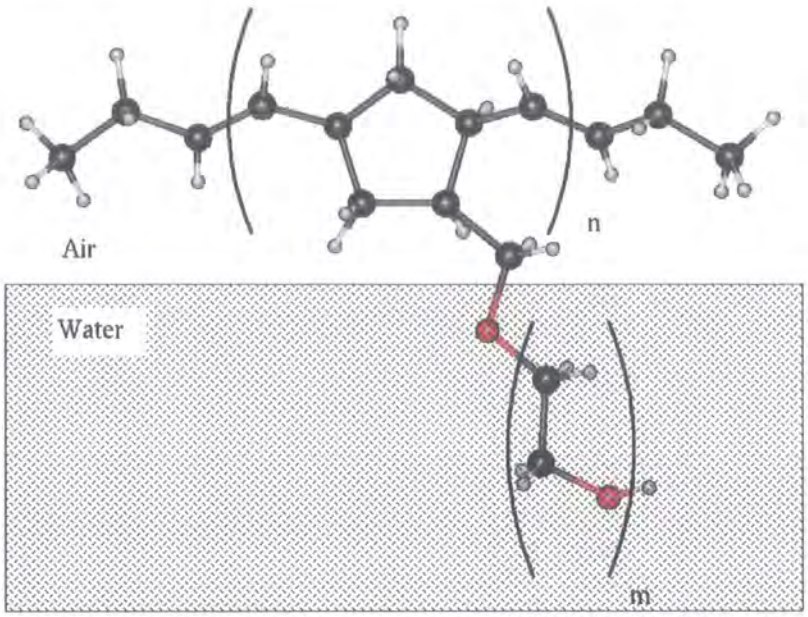

Figure 1.4: An amphiphilic polynorbornene-*g*-poly(ethylene oxide) graft copolymer at an air/water interface.

adhesion.[13–15] Medical science is also making use of polymeric systems and their behaviour at interfaces; drug delivery can be rate-controlled by encasing pharmaceutical compounds within a polymeric shell that gradually degrades within biological systems.[5–7] Polymer interfaces also find uses in the construction of electronic devices[16] and gas sensors.[17]

Interesting effects are observed when polymer molecules, usually simple straight-chains, are tethered to a plane or surface either by chemical bonding, or simple adsorption. Polymer chains grafted to a solid surface, and the amphiphilic graft copolymers at water interfaces mentioned in section 1.2, can be classified as "tethered polymers". Depending upon the graft density at the surface, the polymer chains can adopt a number of different conformations, some of which are shown in figure 1.5. For example, if the space between the graft points is larger than the radius of gyration of the chains (isolated chains), then one of two conformational situations may arise. The first of these is the so-called "mushroom" conformation, and occurs when the polymer molecule adopts a curled-up structure. This arises when the polymer-polymer and polymer-solvent interactions are more favourable than interaction between the polymer and the surface. Grafted polymers typically form

mushrooms at low grafting density in good solvents, when the average inter-graft distance is greater than the radius of gyration of the chains. The second conformation is the "pancake", which is obtained when the chain is able to minimise its energy by lying at the surface. Again, this typically occurs at low grafting density, when the chains are so far apart as to be non-interacting.

There is a third conformation, which occurs when the space between graft points is smaller than the radius of gyration. The chains cannot spread out laterally due to the proximity of neighbouring chains, so they must extend in the direction perpendicular to the surface, and form a "brush". This confinement of chains by their neighbours is known as the *excluded volume interaction*, and arises from the fact that polymer chains cannot overlap with one another.

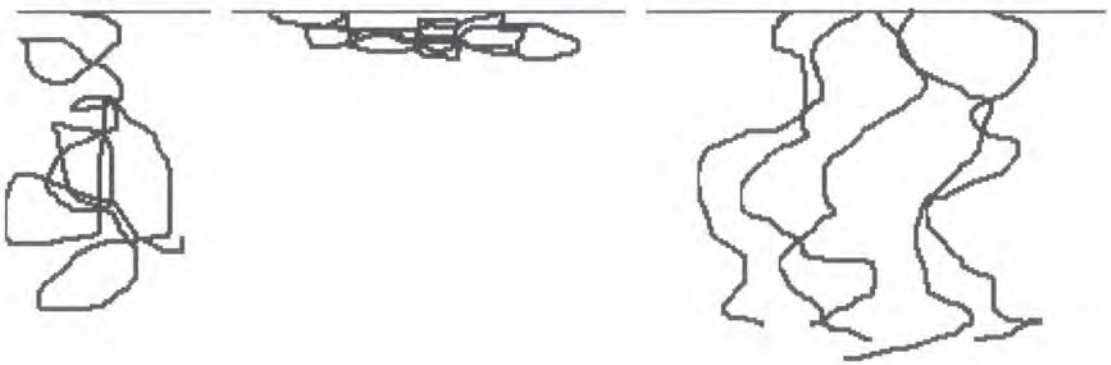

(a) mushroom (b) pancake (c) brush

Figure 1.5: The three major morphologies of a tethered polymer.

The nature of the surface or interface at which the system is tethered can influence the behaviour of the polymer also. Such interfaces can affect the nature of transitions in the polymer, for example the pancake-to-brush transition.[18]

1.3.1 Neutron Reflectometry

As a method for studying polymeric materials at interfaces,[19,20] neutron reflectometry is very useful.[21,22] The technique has also been used to study liquid metal

surfaces,[23] surfaces of liquid-liquid mixtures[24] and the magnetic/structural properties of metallic thin films.[25,26]

The neutron reflectometry process involves firing a beam of neutrons at a surface, and measuring the reflectivity of the interface by analysing the specularly reflected beam's properties relative to those of the incident beam. By monitoring the changes in reflectivity as a function of probe depth, the molecular structure normal to the interface can be profiled. The processes involved are analogous to those in optical reflectivity experiments, however the key quantities involved take different forms; the *wavevector*, Q, is the analogue of scattering angle, while *scattering length*, b, is analogous to refractive index. Since neutron scattering is very sensitive to nuclear identity (including isotopes), the scattering length varies significantly from nuclide to nuclide. The *scattering length density* is a quantity that encompasses both scattering length and number density of a particular species.

The wavevector is defined as the magnitude of the vector between the specularly reflected beam and the transmitted beam at the interface. This quantity can be related to the wavelength of the incident beam, as well as the angle of incidence by equation 1.2,

$$Q = \frac{4\pi}{\lambda} sin\theta, \tag{1.2}$$

where λ is the wavelength of the incident neutron beam, and θ is the angle of incidence.

In neutron reflectometry experiments, reflectivity is measured as a function of wavevector. The wavevector can be changed by varying both the angle of incidence and the wavelength of the incoming neutron beam.

The most important factor in a neutron scattering experiment is the big difference between the scattering lengths of hydrogen and deuterium. The latter has a positive scattering length, which results in a coherent, amplified reflected beam. The negative scattering length of the former results in a poorly reflected beam that merges with the background.

By preparing various contrasts through isotopic substitution, the reflectivity can be analysed as a function of composition allowing the observer to deduce further

Nucleus	b / 10^{-4} Å
C	0.67
O	0.58
^{1}H	-0.37
^{2}H	0.68

Unit	$\sum$b / 10^{-4} Å	ρ / 10^{-6} Å^{-2}
H_2O	-1.68	-0.56
D_2O	1.92	6.35
Air	0	0
Ethylene oxide (H)	0.41	0.56
Ethylene oxide (D)	4.58	6.33
Norbornene	1.78	0.89

Table 1.1: Scattering lengths (b) and scattering length densities (ρ) of units present in the amphiphile/interface system of interest. (H) is hydrogenous and (D) is deuterated.

information on the system's structure without perturbing the structure itself. For example, the experiment can be used to analyse the reflectivity of the system shown in figure 1.4. A fully hydrogenous copolymer molecule at a D_2O interface would have reduced reflectivity compared to pure D_2O, since the deuterium atoms (significant contributors to reflectivity) are reduced in population as hydrogenous material is added. A copolymer with deuterated PEO side-chains placed at the same interface would display a negligible reduction in reflectivity, since now one species of deuterated material (D_2O) is being replaced by another (deuterated PEO). The only causes of reduction in reflectivity in this latter combination would be the hydrogenous polynorbornene backbone and the slightly lower ρ value of the ethylene oxide repeat unit with respect to D_2O.

Due to the opposing signs in the scattering length densities of H_2O and D_2O, it is possible to mix these two species in such a ratio that the overall scattering length density (and reflectivity) is zero. This mixture is known as *null reflecting water* (nrw), and can be used to eliminate all coherent scattering due to the water subphase. In this way, the scattering due to the PEO side-chains can be observed more directly.

1.3.2 Other Techniques

There are many useful techniques for characterising and understanding the behaviour and organisation of materials at surfaces and interfaces. A few of the more commonly used ones are mentioned very briefly here.

1.3.2.1 The Langmuir Trough

The Langmuir trough is not so much an experimental technique itself but a tool which can be used to set up polymer films of varying surface concentrations. The trough is filled with a liquid (typically pure water), and has a movable barrier to allow easy variation of the surface area of the liquid within. Studies of surfactants at water surfaces are often undertaken using Langmuir troughs, where surface concentration can be altered by moving this barrier. At the beginning of a study, a molecular monolayer of surfactant is introduced to the water in the trough by slow dripping of a solution of the amphiphile onto the water surface. A volatile solvent that is immiscible with water (such as diethyl ether or chloroform) is used for this, to ensure that the only species present are the water and the amphiphile upon evaporation of the solvent. The surfactant molecules then remain at the water interface where their surface concentration can be freely altered using the barrier. Neutron reflectivity studies are often performed on materials in a Langmuir trough.

1.3.2.2 Surface Quasi-Elastic Light Scattering (SQELS)

Although they often appear smooth and flat on a macroscopic scale, liquid surfaces are not so at the microscopic level. For example, the surface of water is continuously roughened by tiny perturbations known as *capillary waves* with amplitudes of a few angstroms. The exact behaviour of capillary waves on a liquid surface is dictated by many factors, including the liquid's density, surface tension and viscosity. This behaviour can be analysed using the SQELS technique.

Layers of foreign material (such as amphiphilic polymer films at water surfaces) affect the behaviour of capillary waves. Light is scattered to a significant degree by these waves, and as a result, the nature of the surface in question can be deduced by analysing the relationships between specularly reflected and scattered light.

SQELS has been used to study the behaviour of amphiphilic block[27] and graft[28] copolymers at the water-air interface.

1.3.2.3 Surface Pressure Analysis

Surface pressure is defined as the difference between the surface tension of the pure subphase material A (e.g. water) and that of the material's surface with a covering film of material B (amphiphile). The variation of surface pressure with surface concentration of surfactant can be measured using a Langmuir trough.

Surface pressure is measured using a *Wilhelmy plate* that often takes the form of a simple piece of filter paper. This plate is connected to a device that can accurately measure forces acting on the former due to the surface tension of the liquid phase. Since the surface tension of water is reduced by the introduction of an amphiphilic species to the surface, the force acting on the Wilhelmy plate will vary with the composition of the surface being studied. Forces are measured for a range of surface concentrations, and used to calculate surface pressure values.

Surface pressure isotherms are plotted from these data, showing the variation in surface pressure with surface concentration (figure 1.6). When relatively small molecules are present at the liquid surface, discontinuities are often seen in these plots as the surface material undergoes the two-dimensional analogs of phase transitions. Gaseous regimes are seen when surface concentration is low, and the surfactant molecules do not interact with one another to any great degree, while two-dimensional liquid behaviour is seen at higher concentrations. Monolayers of different surfactant materials can be compared using their surface pressure isotherms.[29]

1.4 Scope of Thesis

The aim of this project is to simulate an amphiphilic graft copolymer at a water/air interface, using the molecular dynamics simulation technique. Attempts will be made to relate the behaviour of the simulated molecules to their real-world counterparts, through the analysis of density and neutron reflectometry profiles. Several surface concentrations of the amphiphile have been simulated in line with previous

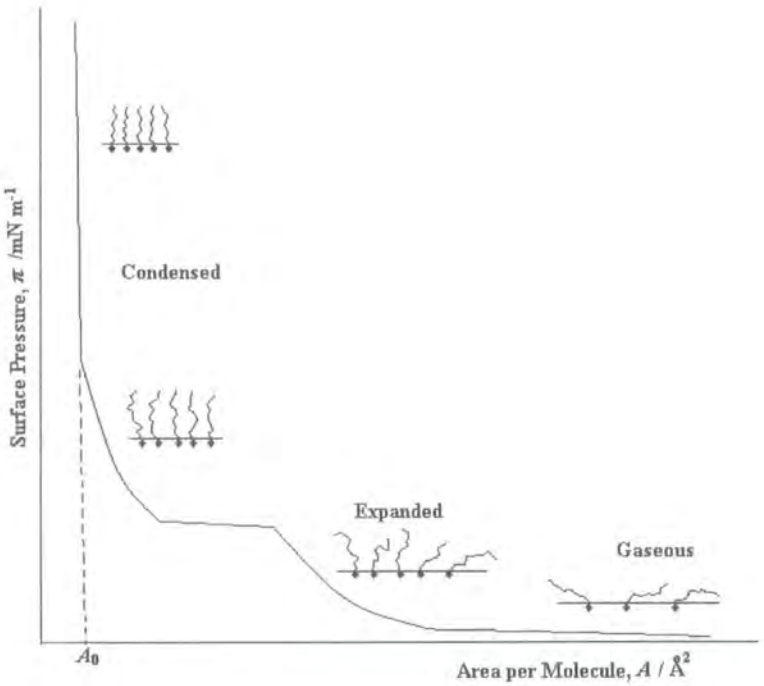

Figure 1.6: A typical surface pressure isotherm for a material at a surface, showing the three different monolayer states: gaseous, expanded and condensed. A_o represents the minimum area per molecule.

experiments,[30–32] and these results are used to assess the viability and applicability of computer simulation to these systems.

Chapter 2 gives a brief introduction to computer simulation, including the ideas behind force fields, molecular dynamics and Monte Carlo. A brief overview of polymer simulation is also presented, along with some of the concepts and models involved in coarse-graining a simulation.

Various models for the simulation of liquid water are discussed in chapter 3. Three of the most commonly used models are assessed in depth through the use of molecular dynamics simulation, where various properties, particularly density, are compared to experimental measurements. Equilibrated systems of bulk water, and a water/air interface are also set up for use in later simulations with the polymers of interest.

In chapter 4, a standard simulation model (force field) for simple organic systems is studied in detail. By performing high-level *ab initio* structure optimisation calculations on 1,2-dimethoxyethane (DME) (a model molecule for PEO), a set of conformational energies were acquired for the former. These energies were subsequently used in fitting force field torsion parameters for the O-C-C-O and C-O-C-C dihedral interactions that are present in both DME and PEO. The results of these fits are assessed on the basis of agreement in conformational populations between simulation and experiment in the condensed phase of DME. Additional analysis and reverse-engineering is also performed on the force field in an attempt to introduce further improvements.

Chapter 5 outlines the simulation studies of the amphiphilic copolymer at the water/air interface, along with structural analysis involving the previously mentioned density and neutron reflectivity profiles. The optical matrix method is used to generate reflectivity profiles using simulation data.

Simulations of poly(ethylene oxide) in solution have also been performed under four different force fields, and are discussed in chapter 6. Comparisons are made between the behaviour of free PEO chains and the tethered chains studied in chapter 5.

Finally, a summary is presented in chapter 7, along with the conclusions drawn

from the work in previous chapters.

Chapter 2

Introduction to Computer Simulation

2.1 Introduction

Although computers can be used to calculate quantum mechanical information on atoms and molecules (energies, intermolecular interactions, etc) through *ab initio* calculations, most studies on bulk materials employ one of two techniques, known as molecular dynamics (MD) and Monte Carlo (MC). The Monte Carlo technique was introduced in the late forties,[33] and was used in the first simulation of a pseudo-liquid[34] (actually an idealised system of two dimensional hard discs). The first Monte Carlo simulation of a true Lennard-Jones fluid was carried out in 1957.[35] Since these rather simple beginnings, the Monte Carlo technique has become a very important tool in the computational study of the behaviour of complex and realistic chemical systems.

The first molecular dynamics simulation was performed by Alder and Wainwright on a set of hard spheres.[36,37] Later, a molecular dynamics simulation of liquid argon was reported by Rahman,[38] and since then, MD has become a key technique in the computational study of molecular systems.

Since their first uses, the two methods have become commonplace, and are now used in many diverse branches of chemistry and physics, such as the study of liquid crystalline behaviour,[39–41] the solid state,[42,43] and gases.[44]

The basic concepts behind the two methods of simulation are outlined in this chapter, along with some of the techniques employed to simulate larger polymeric

systems.

2.2 Computer Simulation

Simulation of chemical systems by computer usually requires analysis of the inter-particle interactions in the system. Many simulations today are *atomistic* (*all atom*), meaning that each atom in the simulated system corresponds to a single atom in the real system. For some computationally expensive calculations, however, the *united atom* approximation is used, where hydrogens are fused with heavier atoms into a single particle; a single "atom" in the simulated system actually represents more than one real atom. This dramatically reduces computational cost since in many organic systems (including PEO), the hydrogen atom is by far the most common. The term "atom" in simulation is often used to denote united atoms (say, a $-CH_2-$ group represented by a single particle) as well as traditional atomistic particles.

This simplification can be taken further with polymeric systems, using a technique known as *coarse-graining*. A typical example of a coarse-grained polymer simulation (section 2.3) could involve the structure of the simulated polymer being simplified to a chain of beads, or hard spheres.

Before any simulation can be carried out, a good representation of the interatomic interactions must be selected. Such a model is known as a *force field*. This section outlines the essential components in computer simulation techniques, including force fields, Monte Carlo and molecular dynamics simulation methods. Two common approximations made in the simulation of bulk systems, *periodic boundary conditions* and *non-bonded cutoffs* are also introduced.

2.2.1 Force Fields

A force field is an energy function that gives the potential of a particular set of interacting particles. In many simulations, the atoms are represented as point masses having various interactions with one another. There are a vast number of force fields available, each with its own strengths and weaknesses and particular applications. Since all simulation work in this thesis made use of the same functional form as the

Optimised Potentials for Liquid Simulation: All Atom (OPLS-AA) force field,[45] this energy function will be described as an example.

Five fundamental interaction types exist within OPLS-AA, which cover the most important of the interactions between atoms in the real world. These five interactions are bond-stretching, angle-bending, torsional-twisting, electrostatic and van der Waals interactions. The force field represents each of these interactions as an expression for that particular contribution to the overall system energy. This overall energy is given as the sum over all atoms and all energy components, as shown in equation 2.1,

$$E_{total} = E_{stretch} + E_{bend} + E_{torsion} + E_{elec} + E_{vdw}, \tag{2.1}$$

where

$E_{stretch}$ is the sum (over all diatomic bonds) of the bond-stretching energies,

E_{bend} is the sum (over all angles between adjacent pairs of bonds) of the angle-bending energies,

$E_{torsion}$ is the sum (over all four-atom bonded sequences) of the torsion energies,

E_{elec} is the sum (over all pairs of interacting atoms) of the electrostatic energies and

E_{vdw} is the sum (over all pairs of interacting atoms) of the van der Waals energies.

It should be noted that in many force fields, it is standard practice to neglect any electrostatic and repulsion-dispersion interactions between pairs of atoms separated by less than three bonds. The bond-stretching and angle-bending energy components are parameterised to take these extra interactions into account. Also, the 1,4-non-bonded interactions are often scaled, as the torsion potential already takes into account these interactions to some extent. The following subsections detail each of these components in turn.

2.2.1.1 Bond-Stretching

In OPLS-AA, like most simple force fields, the bond-stretching interaction is based upon the harmonic oscillator. The covalent bond between two atoms is modeled as an ideal spring, with an energy given by equation 2.2,

$$E_{stretch} = \sum_{bonds} k_s(r_{ij} - r_0)^2, \tag{2.2}$$

where

k_s is the force constant associated with the spring,

r_{ij} is the current distance between the two bonded atoms i and j, and

r_0 is the natural length of the spring when fully relaxed.

Although this ideal spring representation is very commonly used, and usually gives reasonable agreement with experimental results for most systems, the parabolic energy profile it yields does not match the asymmetric interatomic potential observed in experimental and theoretical studies. If the behaviour of the bonds in the system is of particular importance to the results, other more sophisticated bond-potentials, such as the Morse Potential should be used.

2.2.1.2 Angle-Bending

As with interatomic distance, there is a variation in energy when the angle between three sequentially bonded atoms is changed. The typical representation of this energy variation uses the harmonic potential, in an analogue to the bond-stretching potential. The harmonic angle-bending energy function is given in equation 2.3,

$$E_{bend} = \sum_{angles} k_b(\theta - \theta_0)^2, \tag{2.3}$$

where

k_b is the force constant associated with the spring,

θ is the current angle between the two bonds, and

θ_0 is the natural angle between the two bonds when fully relaxed.

2.2.1.3 Torsional (Twisting) Interactions

Torsional energy functions give the variation in energy as rotation occurs about a dihedral. The dihedral angle is defined as the angle between the plane defined by points A, B and C, and the plane defined by points B, C and D, where A, B, C and D are the positions of atoms bonded in a chain with this sequence. The energy

involved in the torsional interaction is shown in equation 2.4,

$$E_{torsion} = \sum_{dihedrals} \frac{V_1}{2}(1+cos(\phi))+\frac{V_2}{2}(1-cos(2\phi))+\frac{V_3}{2}(1+cos(3\phi))+\frac{V_4}{2}(1-cos(4\phi)), \tag{2.4}$$

where

the V_n values are constants, and

ϕ is the current dihedral angle.

2.2.1.4 Electrostatic Interactions

Electrostatics are incorporated into the force field for simulation of charged particles that could occur in ionic compounds, or molecular systems comprised of atoms with differing electronegativities. The Coulomb potential function is used to represent electrostatic interactions, shown in equation 2.5,

$$E_{elec} = \sum_{i=1}^{N} \sum_{j=i+1}^{N} \frac{q_i q_j}{4\pi\varepsilon_0 r_{ij}}, \tag{2.5}$$

where

q_i is the charge on atom i,

q_j is the charge on atom j,

e is the charge on the electron and

r_{ij} is the distance between atoms i and j.

2.2.1.5 Van der Waals Interactions

Like the stretching and bending potentials, there are many different forms used to represent the repulsion-dispersion interactions in force fields. OPLS-AA uses one of the most commonly used forms, the Lennard-Jones potential, shown in equation 2.6,

$$E_{vdw} = \sum_{i=1}^{N} \sum_{j=i+1}^{N} 4\varepsilon_{ij} \left(\frac{\sigma_{ij}^{12}}{r_{ij}^{12}} - \frac{\sigma_{ij}^{6}}{r_{ij}^{6}} \right), \tag{2.6}$$

where

ε_{ij} is the depth of the energy well in the interaction between atoms i and j,

σ_{ij} is the minimum distance between atoms i and j where the interaction potential is zero, and

r_{ij} is the distance between atoms i and j.

Another more accurate, but more computationally expensive form of this non-bonded potential is the Buckingham Potential which is used in situations where an accurate calculation of non-bonded interactions is essential.

2.2.1.6 Additional Force Field Components

The components detailed above can be put together to form a basic force field. Often these components are sufficient to obtain reasonably accurate simulation results, but sometimes greater detail is required in the model used to obtain the desired results. The introduction of additional components to the force field increases complexity and computational expense, but can often improve results in special situations.

Cross-terms[46] are sometimes introduced into a force field to model the interaction between different force field components. For example, in a triatomic molecule, such as water, when the H-O-H angle is decreased, the two O-H bonds will tend to lengthen to minimise unfavourable H-H close contacts. In the OPLS-AA force field representation, however, there is no non-bonded interaction between the two hydrogen atoms, so reducing the H-O-H angle will not affect the O-H bond lengths. To overcome this, cross-terms can be introduced, which model the "mixing" of the stretching and bending potentials, reproducing this effect in simulation.

Other contributions to the system energy can also be modeled specifically in the force field. For example, hydrogen-bonding energy functions have been incorporated into the MM3 force field.[46,47]

2.2.1.7 Other Force Fields

There are many force fields available today in the literature, each with its own strengths and weaknesses. The OPLS-AA force field is a general force field, suitable for the simulation of small organic molecules, or simple polymeric systems. Addi-

tional parameters have been incorporated into this force field for the simulation of heterocyclic systems.[48]

Smith and coworkers have concentrated on creating force fields specifically tailored to particular polymeric systems, such as PEO[49] and poly(propylene oxide).[50] These force fields are based upon high-level quantum chemical calculations. The CVFF[51] force field was designed for peptide and protein simulation, and the AMBER[52,53] force field is used in the study of proteins and nucleic acids. The ESFF[54] force field can be used to model transition metal complexes, in the study of inorganic chemistry.

2.2.2 Molecular Dynamics (MD)

The Molecular Dynamics (MD) method is used to calculate the trajectories of all particles in a simulated system, by evaluating the total force acting upon each atom in the system due to all other atoms, and then adjusting the acceleration, velocity and position of the particle according to Newton's laws of motion. This section outlines the basics of the MD method.

At the beginning of a simulation, all particles in the system are typically given velocities in a Boltzmann distribution, consistent with the selected temperature. At each time-step in the simulation, the forces acting on each atom are calculated by differentiating the energy terms in the force field; these forces are then used to assign accelerations to the atoms. In this way, the time-evolutions of acceleration, velocity and position are played out as the atoms all follow their own complex trajectory, as influenced by their neighbours.

A key idea behind MD is that time is broken down into a series of discrete time-steps. Without the use of these time-steps, the trajectories of the atoms in the system would have to be solved analytically; this is impossible for all but the most simple systems. Integration algorithms (so-called because they are used to integrate Newton's equations of motion) are used to propagate positions and velocities across time-steps in order to give the atomic trajectories. There are several different integration algorithms in use, but the most commonly used ones are the *Verlet*, *Verlet Leapfrog* and *Velocity Verlet*.

2.2.2.1 Verlet Algorithm

In the *Verlet* algorithm, the position and its derivatives with respect to time are treated as Taylor series expansions,

$$\mathbf{r}(t - \delta t) = \mathbf{r}(t) - \mathbf{r}'(t)\delta t + \frac{1}{2}\mathbf{r}''(t)\delta t^2 - ... \tag{2.7}$$

and

$$\mathbf{r}(t + \delta t) = \mathbf{r}(t) + \mathbf{r}'(t)\delta t + \frac{1}{2}\mathbf{r}''(t)\delta t^2 + ..., \tag{2.8}$$

where

$\mathbf{r}(t - \delta t)$ is the position at the previous time-step,

$\mathbf{r}(t)$ is the position at the current time-step,

$\mathbf{r}(t + \delta t)$ is the position at the next time-step and

$\mathbf{r}'(t)$, $\mathbf{r}''(t)$, ... are the time-derivatives of position (velocity, acceleration etc) at the current time-step.

The expressions for the positions $\mathbf{r}(t - \delta t)$ (equation 2.7) and $\mathbf{r}(t + \delta t)$ (equation 2.8) truncated at the third term, are combined to give an expression for the position at the next time-step, $\mathbf{r}(t + \delta t)$ in terms of $\mathbf{r}(t)$ and $\mathbf{r}''(t)$ (current position and acceleration):

$$\mathbf{r}(t + \delta t) = 2\mathbf{r}(t) - \mathbf{r}(t - \delta t) + \mathbf{r}''(t)\delta t^2$$

The *Verlet* algorithm neither generates, nor uses velocities at any time during the calculation as they are cancelled in the addition of the two Taylor expansions; if the velocities are required by the simulator (as they are for calculation of kinetic energies), they must be calculated manually, using

$$\mathbf{r}'(t) = \frac{\mathbf{r}(t + \delta t) - \mathbf{r}(t - \delta t)}{2\delta t}.$$

The lack of velocities, and also a lack of precision in adding the relatively small $\mathbf{r}''(t)\delta t^2$ to the larger $2\mathbf{r}(t) - \mathbf{r}(t - \delta t)$ often prompts simulators to use alternative integration algorithms.

2.2.2.2 Verlet Leapfrog Algorithm

The *Leapfrog* algorithm makes use of the atomic velocities in calculating the trajectories of the particles. Here, the positions are calculated using velocities which are half a time-step "out of phase" with the positions:

$$\mathbf{r}(t+\delta t) = \mathbf{r}(t) + \mathbf{r}'(t+\frac{1}{2}\delta t)\delta t$$

and

$$\mathbf{r}'(t+\frac{1}{2}\delta t) = \mathbf{r}'(t-\frac{1}{2}\delta t) + \mathbf{r}''(t)\delta t.$$

The *Leapfrog* algorithm's staggering of velocity and position results in problems when trying to calculate both potential (position-based) and kinetic (velocity-based) energies for the same point in time.

2.2.2.3 Velocity Verlet Algorithm

The *Velocity Verlet* algorithm allows the calculation of position and velocity at the same time, in a synchronised manner unlike that of the *Leapfrog* algorithm:

$$\mathbf{r}(t+\delta t) = \mathbf{r}(t) + \mathbf{r}'(t)\delta t + \frac{1}{2}\mathbf{r}''(t)\delta t^2$$

and

$$\mathbf{r}'(t+\delta t) = \mathbf{r}'(t) + \frac{1}{2}\left[\mathbf{r}''(t) + \mathbf{r}''(t+\delta t)\right].$$

After advancing the positions, the velocities are also advanced by calculating an intermediate velocity,

$$\mathbf{r}'(t+\frac{1}{2}\delta t) = \mathbf{r}'(t) + \frac{1}{2}\mathbf{r}''(t)\delta t.$$

2.2.3 Monte Carlo (MC)

Monte Carlo (MC) is used to sample the available configurations of a chemical system in the same way as MD, but whereas MD uses forces and accelerations to calculate

the positional time-evolution of the atoms, MC randomly generates configurations and either accepts or rejects them on the basis of their energy.

The key to the MC method involves making an attempted change (move) to a system, and comparing the new and old energies using formula 2.9,

$$X \leq \exp\left(\frac{-\Delta E}{k_B T}\right), \tag{2.9}$$

where

X is a random number between 0 and 1,

ΔE is the energy change on making the trial move,

k_B is the Boltzmann constant and

T is the system temperature.

If this condition is true (as it is always for an energy decrease), then the new configuration is accepted. The move is rejected (and the current configuration retained for the next move) if this condition is not met. In this way, a sequence of configurations known as a Markov Chain is generated, and is analogous to the trajectory obtained from MD. In the limit of infinite simulation time, the set of sampled configurations of a particular system obtained from MC and MD, as well as averages of properties such as energy, are identical.

For molecular systems, energies are calculated using a force field, just as in MD. MC moves may involve the changing of an internal parameter, such as the length of a bond or the value of a dihedral angle, or an external parameter, such as the position of the molecule or its orientation.

2.2.4 Further Considerations

The MC and MD techniques are very powerful in that much can be accomplished with small systems. Often, however, a simulation of bulk material is required. Obviously it is impractical and far too computationally expensive to simulate sufficient atoms to model, say, a beaker of water, not only because of the number of individual particles required, but also due to the sheer number of interactions between them. Some approximations are therefore used in these simulation techniques, to model

bulk materials with as little computational expense as possible while preserving the link to reality in the simulated system. The two most commonly used of these approximations are *cutoffs* and *periodic boundary conditions.* Both are applicable in MC and MD simulations.

2.2.4.1 Non-Bonded Cutoffs

In most simulations, the majority of computer time is taken up calculating interactions between non-bonded particles. The non-bonded interactions in particular are expensive because the interaction of every atom with every other atom in the system must be considered. Thus, computational cost of the non-bonded calculations increases with the square of the number of atoms. Many of these calculations will produce tiny forces or energies, due to the fact that many pairs of atoms are separated by large distances. Usually, it is safe to neglect any interactions between pairs of atoms separated by significant distances, as these interactions will be very small compared to shorter-range interactions. A maximum distance, known as the cutoff distance is usually selected such that interactions between pairs of atoms separated by more than this cutoff will be set to zero. This helps improve the efficiency of the simulation enormously, but care must be taken in selecting the cutoff distance to ensure that no important interactions are neglected.

The cutoff values used in the simulation work described in this thesis were selected according to computational cost. The large systems studied in chapter 5 demanded a lower cutoff distance than the relatively small water simulations described in chapter 3, for example. The simulations of aqueous PEO described in chapter 6 were assigned the same cutoff distance as the amphiphilic polymer simulations in the previous chapter, to allow direct comparisons to be drawn between the behaviour of tethered and free PEO chains in solution.

2.2.4.2 Periodic Boundary Conditions

Where cutoffs improve simulation efficiency by cutting out less significant interactions, periodic boundary conditions[55] are used to model bulk systems such as liquids. When using periodic boundary conditions, all atoms in the simulation are placed

into a "simulation box". This box lies on an infinite lattice, surrounded on all sides by images of itself and its contents, as illustrated in figure 2.1.

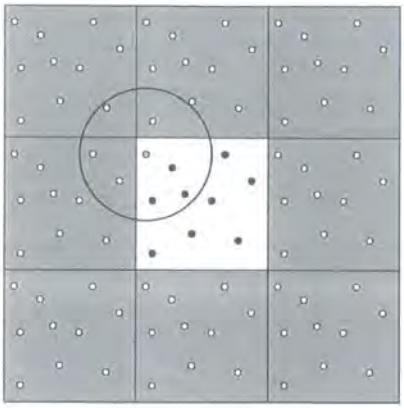

Figure 2.1: Periodic boundary conditions applied to a simple monatomic system in two dimensions. The circle's diameter is equal to the edge length of the boxes, and represents the maximum allowed cutoff for this system.

In the figure, the central, white, box is the actual simulation box, and the gray boxes are its periodic images. The circle around the gray atom in the simulation box represents the maximum allowed cutoff for this system, if the *minimum image convention* is to be observed. This convention limits the cutoff to prevent any atom, A, interacting with both atom B, and an image of B. The period of the system must therefore be at least as large as twice the cutoff to prevent this type of interaction. Of the nine other atoms in the simulation box, interactions are only permitted between seven of them and the gray atom in this case.

The periodicity of the system removes any edge effects experienced by atoms near the non-interacting walls of the simulation box. As images have the same interactions as "real" atoms, any atom on the edge of the box will still experience an environment consistent with bulk material. Although figure 2.1 shows a two dimensional system, periodic boundary conditions can also be applied in three dimensions.

2.3 Simulations of Polymers

The structural and dynamic behaviour of polymers is a very interesting area of study, and one which is relevant to industry and every-day life. The varied properties of

polymeric materials play an important role in many areas, such as manufacturing and packaging. It is vital, therefore, that a good understanding of these properties is obtained through experimental and theoretical studies. It is not surprising that a great deal of simulation work has been done on polymeric systems.

Tasaki has simulated PEO in solution, using water[56] and benzene[57] as the solvent, and analysed the conformational behaviour of the polymer chain. PEO has also been investigated in the melt[58] using both MD and neutron scattering techniques. The transport of electrolytes, particularly the lithium ion through solid PEO[59,60] has also been looked at using the MD technique.

Simulations of polymers are not limited to PEO, however. The interaction of water with bisphenol-A-polycarbonate and polyvinylalcohol has been investigated[61] in simulation. Diffusion of gas and water molecules through various copolymers involving polystyrene[62] and polybenzoxazine[63] has also been studied using simulation.

Single polymer molecules are often massive entities, and as a result, it is difficult to model them atomistically in a simulation, due to computational cost. Also, chain-like polymers in a condensed phase such as the melt are difficult to simulate atomistically as chain entanglement results in a very slow exploration of phase-space. These problems can be overcome with a general method known as *coarse-graining*. A coarse-grained model of a polymer typically has a single interaction site which corresponds to several atoms in the real polymer. The united-atom model in molecular simulation can be thought of as a coarse-grained model. However, in polymer simulation, the single interaction site often represents a larger number of atoms; often one or more monomers are approximated to a single site, but sometimes an entire molecule (or more) may be mapped to a single coarse-grained interaction site.

The coarse-graining technique is not limited to use in polymer systems alone; a similar approach to the united-atom approximation is often used in the simulation study of liquid-crystalline materials, where a single mesogen (non-spherical, often rod-like particle/molecule responsible for formation of liquid crystalline phases) is represented by a spherocylinder,[64] or Gay-Berne particle.[65] Coarse-graining can be used in the representation of liquid crystal molecules as well as colloidal particles.[66]

This section discusses some of the more important coarse-graining techniques as used in the simulation of polymeric systems.

2.3.1 Lattice Methods

Lattice methods present a discretised volume of space to the polymer molecule. Interaction sites within the polymer can only occupy certain discrete positions on a lattice.

2.3.1.1 Slithering Snake Model

In this model,[67] a polymer chain is broken down into a series of connected interaction sites. Each site must occupy a free lattice position, and the distance (bond length) between any two successive interaction sites must always be unity.

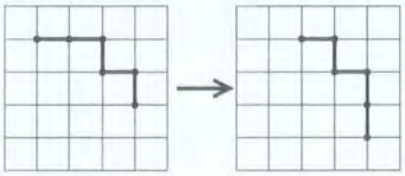

Figure 2.2: The slithering snake representation of a polymer molecule.

The polymer molecule is represented as a snake-like entity; the "head" end moves on one lattice position, dragging the rest of the chain along behind it (figure 2.2). Chain overlaps are not allowed in this model, meaning excluded volume effects are reproduced. Each lattice point may only hold one monomer at a time, so it is possible for the polymer molecule to adopt a configuration where no further moves can be made. The solution to this problem is to allow the swapping of the "head" and "tail" ends of the molecule, so reversing the direction of travel. This model has been used in many different studies, including the simulation of microphase separation in polymer melts.[68]

2.3.1.2 Bond-Fluctuation Model

The bond-fluctuation model[69] is another lattice model, but here the occupancy of lattice sites by monomers is somewhat different. In this model, a monomer occupies

the space bounded by four (in two dimensions) or eight (in three dimensions) lattice sites. The lattice sites immediately surrounding the monomer are considered to be occupied, and cannot be occupied by more than one monomer. As a result, the minimum distance between two monomers is two lattice spacings.

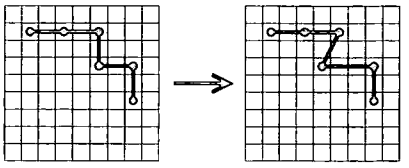

Figure 2.3: The bond-fluctuation representation of a polymer molecule.

Figure 2.3 shows an allowed move for this model. Unlike the slithering snake model, bond fluctuation allows variable bond lengths. In two dimensions, allowed bond lengths are $l = 2$, $\sqrt{5}$, $\sqrt{8}$, 3, $\sqrt{10}$ or $\sqrt{13}$ lattice spacings. So long as the initial configuration is self-avoiding, and all bond lengths are < 4 lattice spacings, then this model will (for two dimensions) remain self-avoiding, that is, no crossing of bonds will occur. In this model, any monomer may be moved by a distance of one lattice spacing in any of the four (or six for three dimensions) in-lattice directions. The move will be either rejected or accepted on the basis of the new configuration having allowed or disallowed bond lengths and angles, and its remaining in a self-avoiding configuration. Unlike the slithering-snake model, the bond-fluctuation model can also be used with branched systems.

This model and several variants have been used to investigate polymer diffusion,[70] relaxation of a confined polymer chain,[71] polymer brush behaviour[72] and the glass-transition.[73]

2.3.1.3 Repton Model

This model[74] is unusual, in that the normal excluded-volume constraints (i.e. only one monomer per lattice site) do not apply. Figure 2.4 shows a typical allowed move in this model.

An internal monomer may enter a lattice site already occupied by another monomer (or several other monomers), resulting in a lack of excluded-volume. A

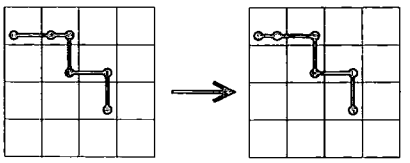

Figure 2.4: The Repton representation of a polymer molecule.

monomer may only leave a lattice site for an adjacent one if the lattice site being left still contains at least one monomer, bonded to the migrating monomer. Thus, internal monomers can only follow the contours of the polymer chain, and only bond lengths of 0 or 1 lattice spacing are allowed. Terminal monomers have more freedom, and may move to any adjacent lattice site, provided that they do not leave behind an unoccupied lattice site, which would necessitate a bond length longer than one lattice spacing.

A variant of the Repton method has been used very recently[75] to successfully simulate microphase separation in a binary mixture of polymers. Excluded-volume has been incorporated into this variant, as has the ability of internal monomers to make sideways moves by using a hexagonal lattice, rather than a square one. Interactions between nearest-neighbour lattice sites allows specific potentials to be applied to the polymer system under investigation, and to drive the phase separation.

2.3.2 Off-Lattice Methods

Off-lattice methods are more closely related to real systems than the lattice methods. Here, space is no longer discretised, and bond lengths and angles may be allowed much more freedom in value, depending on the model used. There are many off-lattice methods available for coarse-graining of polymeric systems, and this section details some of the more important ones.

2.3.2.1 Bead and Spring Model

In this model, the polymer chain is formed by a series of hard spheres, connected by springs. The spheres represent individual monomeric units, and are not allowed to overlap. The springs are often modeled using a harmonic potential, or a FENE po-

tential. The latter allows harmonic-like extension within a certain range of lengths, but with steeply increasing energy outside of that range. The chain resulting from this model can adopt any bond angle or length (depending on potential used) as long as the overlap of spheres is avoided. This model is illustrated in figure 2.5.

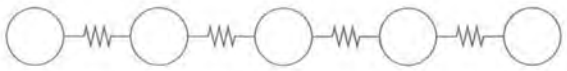

Figure 2.5: The bead and spring representation of a polymer molecule.

This model has been used to study the behaviour of a single polymer molecule in solution,[76] the adsorption of polymer chains at a surface[77] and the conformational relaxation of a deformed polymer chain.[78]

2.3.2.2 Freely-Jointed Chain

The freely-jointed chain model is very similar to the bead and spring model. The only real difference is that the bond lengths between spheres are not variable. It is often the case that the bond length chosen is equal to the diameter of the spheres, such that the spheres are all in contact (but not overlapping) with their neighbours. Figure 2.6 shows a typical polymer chain modeled using this method.

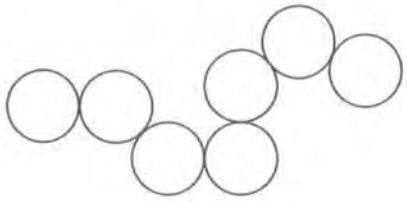

Figure 2.6: The freely-jointed chain representation of a polymer molecule.

2.3.2.3 Dissipative Particle Dynamics (DPD)

The DPD method[79,80] is usually reserved for simulation of colloidal suspensions. The behaviour of such a suspension would be impossible to study using atomistic simulations with current computers, since colloidal particles are "macroscopic" in scale, ranging up to 1 μm in size. Such "macroscopic" particles may contain millions of atoms, so it would be impractical to run an atomistic simulation on even one

such particle, neglecting its neighbours and the solvent. In addition, the Brownian motion involved in the dynamic behaviour of colloidal particles occurs on much longer timescales than those used in traditional MD simulations. Some form of coarse-graining technique is therefore required to allow many colloidal particles to interact with one another, and a solvent, on very long timescales; the DPD scheme finds much use in this particular field.

In DPD, a colloidal particle is modeled as a single spherical particle, and typical pair potentials between such particles are soft repulsive interactions. A *dissipative force* is added, to model the frictional effects experienced by the colloids as they pass through the solvent.

DPD is not limited to the study of colloids; the method can be applied to polymeric systems by linking together soft repulsive potentials by soft springs. DPD has successfully been used to model the microphase separation in a block copolymer.[81]

2.4 The Role of Simulation in the Current Study

Because the aims of this project include the study of the dynamics of a polymer brush, the MD method is the most appropriate technique available. A fully atomistic description of the polymeric system in question is also desirable, to minimise the number of approximations made in the generation of MD trajectories. The advantages of a fully atomistic MD simulation include non-discretised space, and therefore continuous potentials, bringing the quality of the model much closer to the level of the corresponding real systems.

Although the main simulations of the polymeric systems are to be carried out with MD, the MC technique is also briefly used to encourage the amphiphilic copolymer to adopt an appropriate conformation for easy setting up of the main simulations.

Chapter 3

Molecular Dynamics Simulations of Water

3.1 Introduction

As the most abundant liquid on Earth under ambient conditions, it is no surprise that water has been extensively studied using computer simulation. Water's nature as a simple triatomic molecule only adds to the attractiveness of this substance for study in simulation and much work has been carried out in this area.[82–117]

Simulation studies of water as both the pure compound and as a solvent have been undertaken previously. Many of these simulations have shown that the real-world behaviour of water is not easily reproduced computationally, despite the simple structure of the molecules concerned. Many different models of water have been used in simulations of varying computational cost and agreement with the true behaviour of water.[82,90–95,99,102–117] Some of the more important models of water are summarised in section 3.2.

Although many computational studies of water have already been carried out, there are several good reasons for simulating this simple molecule in the current work. First of all, as there are so many different models of water available, it is desirable to assess them for accuracy. Many of the water models were originally tested with only a small number of molecules when they were in development, so it is desirable to investigate the viability of the models in much larger systems.

Further advantages of studying water include obtaining timing data for the simulations, which can be used to help in the planning and scheduling of subsequent work. An equally important motivation is that fully equilibrated water systems in the bulk and with a water/vapour interface will be obtained for use in polymer solution simulations. A variety of non-bonded cutoff schemes can also be evaluated with such simulations of water.

The ultimate aim of this section is to evaluate the various potential truncation schemes and water models, to select the most appropriate method to be used in the simulations of amphiphilic polymer molecules at the air/water interface, and to produce such an equilibrated air/water interface.

3.2 Water Models

Since the water molecule apparently has only three interaction sites (one oxygen atom, and two hydrogen atoms), it would seem reasonable to assume that an accurate model of the water molecule for use in simulation would only require three interaction sites. There have been many such simple models of water, including the Simple Point Charge (SPC) model,[82] and the Transferable Intermolecular Potential Three Point (TIP3P) model.[92] These, like most water models, are specified as rigid to minimise computational cost and allow reasonably large time-steps in bulk simulation.

Although three-site water models do give reasonable agreement with experimental work, the results are not perfect.[92] For example, the old SPC model of water gives a calculated bulk density of 0.971 g cm^{-3} (experimental value = 0.997 g cm^{-3}). Although the TIP3P model (which was reparameterised to optimise the density and heat of vapourisation calculations for liquid water) gives an improved value of 0.982 g cm^{-3}, results are still far from perfect.

Much work has gone into improving and optimising these models for specific uses. For example, the SPC model has been improved by Berendsen, Grigera and Straatsma,[91] to give the Extended Simple Point Charge (SPC/E) model, which is better suited for use in a bulk liquid simulation than its predecessor.

It has been found that adding more interaction sites to the model can significantly improve the agreement between experiment and simulation for many properties of liquid water, including the density profile with respect to temperature. The Bernal-Fowler (BF)[90] model, proposed in 1933, was one of the earliest potential functions devised to emulate the behaviour of water molecules, and was designed with four interaction sites. This is particularly surprising, since the first computer simulations of water[100,101] did not occur until around 1969.

In the case of the TIP4P model,[92] the radial distribution function is improved, as is the density (0.999 g cm $^{-3}$). Even with these improvements, there is still a long way to go. For example, none of the more well known three- or four-site models are particularly good at predicting the curious density anomaly that occurs in water between $0 - 4^{o}$C.

There are many five-site models of water in the literature, including the BNS model[99] and the ST2 model.[114,115] Jorgensen introduced the five-site TIP5P model to reproduce the water density anomaly in simulation.[93] When comparing the TIPnP series of water models in simulation to experimental data, Jorgensen found that the temperature-density curve is closest to experimental data for the TIP5P model. However, the isobaric heat capacity predicted by the TIP5P model, 29.1 cal mol $^{-1}$ deg $^{-1}$ is significantly poorer than previous models (20.0 cal mol $^{-1}$ deg $^{-1}$ for TIP3P and 20.4 cal mol $^{-1}$ deg $^{-1}$ for TIP4P) and experiment (18.0 cal mol $^{-1}$ deg $^{-1}$).

There are water models with even more unusual numbers of interaction sites, such as the six-site MCHO[102] and NCC[103] models. The PE model,[106] involving only one interaction site, has also been proposed.

Other water models have various unique features; the TIPS[116,117] and the NSPCE[105] models have been designed with different forms for their non-bonded interaction potentials in attempts to improve the agreement between simulation and experiment. The former uses a variant of the Lennard-Jones 12-6 function, whereas the latter involves an exponential term in its non-bonded interactions.

As long as the charge distribution remains fixed in water models, they will never reach the extremely good agreement with experiment that is desired. In reality,

the water molecule is electrically polarisable; the charge distribution throughout the molecule is flexible, and can rearrange itself to minimise the potential of the system according to the environment. Attempts have been made to introduce polarisability by incorporating fluctuating charges,[94,95] and polarisable sites[96] (sites at which dipoles are induced by the electrostatic influence of neighbouring particles). Polarisability has been introduced into a number of water models, including SPCP,[113] PTIP4P,[107] SPC/FQ and TIP4P/FQ[112] (variants of the SPC and TIP4P models). Molecular flexibility has also been introduced into various models, such as RWK,[109] SPC/F,[110] SPC/FP[111] and NCCvib[104] (variant of the NCC model).

Studies of polarisable water models were prompted by the fact that traditional point-charge models of water (TIP3P, TIP4P, SPC, SPC/E etc.) have been parameterised for use in bulk liquid simulation. The dipole moments of these models (e.g. 2.27 D for SPC) are usually set significantly higher than the dipole moment of an isolated water molecule (1.85 D) in order to obtain the best simulation results for bulk water. This increased dipole moment helps to take into account the polarisation effects of bulk phases, but reduces the reliability of results for gas phase studies.

A review by Guillot[108] makes comparisons between these and many other water models that have been proposed over the years, and is an excellent source of information and references on the various water models available.

Ab initio MD simulations have also been performed using the Car-Parrinello method which calculates forces from quantum, rather than classical mechanics. Water was one of the first systems studied using this method.[118,119] Using these simulations, many structural properties of water such as the radial distribution function and vibrational spectra were successfully calculated. As computational power has increased, more detailed quantum MD simulations become possible. Such a study of water done in 1999[120] used a larger system and longer timescales to investigate properties such as molecular polarisation and dipole moments. Due to the computational cost of quantum methods, however, such simulations are not as common as their classical counterparts.

The simulation work detailed in this chapter involves three of the simpler and most commonly used water models, namely SPC/E, TIP4P and TIP5P, the newest

member of the TIPnP family. All simulations use classical MD techniques.

3.2.1 Extended Simple Point Charge (SPC/E)

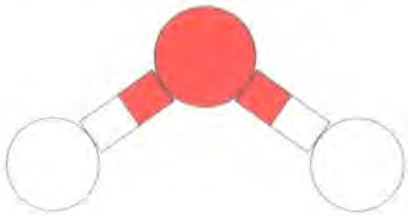

Figure 3.1: Structure of the SPC/E water model.

The SPC/E model[91] of water, shown in figure 3.1, is the simplest of the three chosen for evaluation. It consists of only three interaction sites, at the centres of the three component atoms. The atoms themselves are represented by point masses. Table 3.1 gives the details of this model. In comparison to the earlier SPC model, SPC/E gives better agreement with experiment for bulk phase properties, such as density and radial distribution functions.

All of the charges and repulsion-dispersion effects are centred on the atoms themselves. The oxygen is the only atom in the model that experiences non-electrostatic non-bonded interactions; the hydrogen atoms are completely inactive in terms of repulsion-dispersion effects in this model.

r_{OH}/Å	θ_{HOH}/^{o}
1.0	109.47

q_O / e$^-$	q_H / e$^-$	ε_O / kcal mol^{-1}	σ_O/Å
-0.8476	0.4238	0.1553	3.1656

Table 3.1: Parameters for the SPC/E water model.

3.2.2 Transferable Intermolecular Potential Four Point (TIP4P)

Like the SPC/E model above, TIP4P[92] (shown in figure 3.2) is composed of point masses, and has only one Lennard-Jones interaction site, the oxygen atom. However,

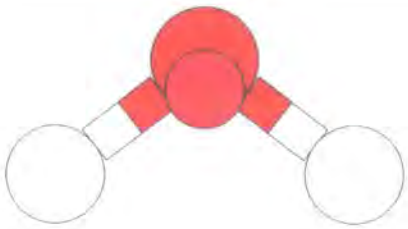

Figure 3.2: Structure of the TIP4P water model.

unlike the SPC/E model, TIP4P has four interaction sites in total. In addition to the three atoms, there is an additional site, *M*, which has no mass. Point *M*, which carries all of the negative charge present in the model, represents the shifting of the negative charge slightly away from the oxygen atom. *M* lies on the H-O-H angle bisector, displaced toward the hydrogen atoms. Table 3.2 shows the various parameters used in the TIP4P water model.

r_{OH}/Å	r_{OM}/Å	θ_{HOH}/°
0.9572	0.15	104.52

q_O / e$^-$	q_H / e$^-$	q_M / e$^-$	ε_O / kcal mol^{-1}	σ_O/Å
0.0	0.52	-1.04	0.1550	3.1536

Table 3.2: Parameters for the TIP4P water model.

3.2.3 Transferable Intermolecular Potential Five Point (TIP5P)

This model,[93] shown in figure 3.3, is the latest in the TIPnP series. It was proposed in 2000, and has proved to be useful in reproducing the unusual variation of density with temperature around the freezing point of water. Once again, this model is composed of points which carry masses, charges and Lennard-Jones parameters. The oxygen atom is still the only repulsion-dispersion active atom in the model, and now there are two massless points, L_1 and L_2, which carry the molecule's negative charge. L_1 and L_2 represent the lone electron pairs on the water's oxygen atom, and are positioned accordingly. Properties of the TIP5P model are shown in table 3.3.

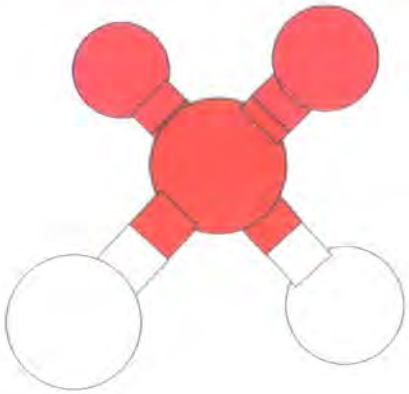

Figure 3.3: Structure of the TIP5P water model.

r_{OH}/Å	r_{OL}/Å	$\theta_{HOH}/^o$	$\theta_{LOL}/^o$
0.9572	0.70	104.52	109.47

q_O / e$^-$	q_H / e$^-$	q_L / e$^-$	ε_O / kcal mol^{-1}	σ_O/Å
0.0	0.241	-0.241	0.16	3.12

Table 3.3: Parameters for the TIP5P water model.

3.2.4 Simulations of Water

Although a lot of research groups devote their time to devising new and better water models, many workers use these models in simulations. There have been many studies carried out, simulating water in different situations. Examples of the diverse uses for water (and other liquid) simulations include the study of interfaces,[97] and the study of aqueous solutions.[98] This section summarises the work done by various researchers in the field of water simulation.

3.2.4.1 Simulation of Water Interfaces

Many simulations have been performed to study water interfaces. In some simulations the water liquid-vapour interface is studied. In other simulations, a liquid-liquid interface (where one of the liquids is water) has been looked at. Workers have looked at many different properties of water surfaces, including the molecular orientation of both water molecules[83] and surfactant molecules[84] at the surface.

Interfaces between aqueous and hydrophobic phases have also been simulated.[85,86] Many groups involved in looking at water interfaces, particularly the liquid-vapour interface, also produce density profiles, which gives an idea of how the system's density changes across the interface.[83,86] Yet another interesting aspect of interfaces is what happens when particles pass through them; Lynden-Bell and coworkers have used MD simulation techniques to study the effects of the passage of CO_2 and N_2 molecules through a water-air interface.[87,88]

The most common method of producing a liquid-vapour interface is to take a simulation box of equilibrated molecules, say water, and expand it in the z-direction. By doing this, the water remains at normal density in the middle of the simulation box in the form of a "block" or "slab", and two regions of vacuum are produced. This method actually results in two interfaces, but if they are a great enough distance apart, they will not interfere with one another. After this is done, the system is then equilibrated for a while under a constant-volume (e.g. NVT) ensemble; it is necessary to switch to constant-volume dynamics, because constant-pressure dynamics would result in the newly expanded box collapsing back down to its natural size for bulk water. After equilibration, the density near the interfaces will have reduced, giving a smooth transition region between liquid and vapour. Then the sampling stage of the simulation can be carried out, also under constant-volume conditions.

3.2.4.2 Simulation of Water Solutions and Mixtures

Simulations of water are not limited to the pure substance; solutions and mixtures have also been extensively studied. Auffinger and Beveridge performed MD simulations on an aqueous NaCl solution,[98] in order to investigate the effects of potential truncation on the radial distribution function as discussed in section 3.3. Simulation techniques have also been applied to the study of argon dissolved in water,[121] various alcohol-water mixtures[122] and solutions of NaCl in a mixed water-alcohol solvent.[123]

3.3 Cutoff Schemes

As well as simulating three water models, three cutoff schemes were used. The schemes that were chosen were those that are most commonly used in simulation. A brief outline of each scheme is given in the following sections. Although the Coulombic interactions are evaluated with each of these schemes, the repulsion-dispersion interactions may only be evaluated via standard atomistic truncation. Cutoffs can have a significant impact on the outcome of a simulation; it has previously been pointed out[124] that the user could well be inadvertently simulating two different systems if both the MC and MD method are used on one collective of atoms since the former truncates energy at the cutoff distance, whereas the latter also truncates forces. It is therefore essential to have a consistent definition of cutoffs throughout any simulations of a particular system whose outcomes are to be subject to any kind of meaningful comparison.

3.3.1 Coulombic Atom Based Cutoffs

The simplest cutoff scheme involves neglect of any interactions between centres separated by more than the cutoff radius (r_{cut}). At first sight, this may seem perfectly reasonable, however there are dangers inherent in this method. For example, the distribution of particles around one another, as measured with the radial distribution function, may show unexpected artifacts;[98] this problem occurs in the simulation of fluids with charged particles, including systems involving electronegative atoms or ions.

Figure 3.4 shows an example of this distortion in particle distribution. The oxygen atom on the central water molecule has a favourable coulombic interaction with the hydrogens of the other water molecule, however the unfavourable oxygen-oxygen repulsion is discounted as it occurs over slightly longer range than the cutoff allows. This results in an artificial lowering of the system energy, and also an unnatural accumulation of charged particles around each other, at the cutoff distance. Section 3.5 illustrates these problems, making reference to radial distribution functions obtained from simulation.

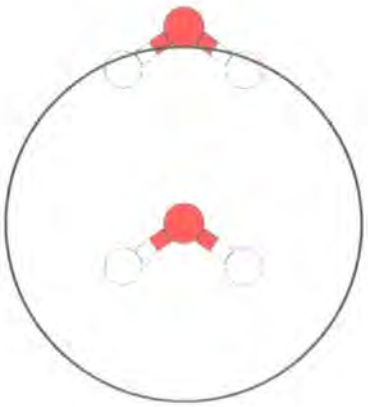

Figure 3.4: Illustration of a flaw in the atom based coulombic cutoff method. Artificial energy reductions can occur by charged particles ordering themselves around the cutoff distance, represented here as a circle around the central oxygen atom.

3.3.2 Coulombic Charge-Group Based Cutoffs

This method is similar to the atom based cutoffs mentioned above. The difference is that instead of basing the cutoffs on distances between pairs of atoms, the decision of whether or not to include an interaction in the energy calculation is based upon the distance between groups of atoms, or *charge-groups*. To obtain maximum benefit from the method, charge-groups should be set up such that they have a minimal (or better still, zero) overall charge. This will prevent the previously mentioned anomalous distribution of particles.

Various implementations and definitions exist for charge-group cutoffs. For example, in the DL_POLY[125] molecular dynamics program, all interactions are included between the two groups, say A and B, if the distance between any member of group A and any member of group B are within the cutoff distance. Otherwise, no interaction is calculated between the two groups. In the situation shown in figure 3.4, properly defined charge-groups would force the calculation of all interactions between the two water molecules, even though some interatomic distances in the system lie outside the cutoff distance.

Although this method improves upon atom based cutoffs by eliminating the accumulation of charge around r_{cut}, there are still disadvantages. It is possible, for example, to have two charge groups at fixed separation, where none of the atom pairs between the two groups are within r_{cut}. For rigid molecules, this would be acceptable

as no interactions between the two groups would be included. However, if the groups are not constrained in any other way, then simple bond stretching could bring pairs of atoms within r_{cut}. This would result in a whole range of interactions being included in the calculation sometimes, and completely neglected at other times.

Also, charge-groups would not be appropriate for use with simple ionic systems like NaCl. Charge-groups are intended to be composed of groups of atoms connected by covalent bonds (or at least fixed in close proximity to one another).

3.3.3 Ewald Sum

The Ewald Sum[126] is one of the best methods available for handling long range non-bonded interactions. Due to the nature of this method, only interactions between charges are handled. The remaining non-bonded interactions, i.e. the Lennard-Jones interactions, must still be truncated in a conventional fashion. The Ewald Sum is the most computationally expensive of the cutoff methods employed in this study.

The Ewald Sum method works by splitting the electrostatic energy sum into a short-ranged component (calculated in real space), and a long-ranged component (calculated in reciprocal space). In the DL_POLY[125] implementation of the Ewald Sum technique, convergence in these sums is controlled by the *convergence parameter*, α. The parameters k_1, k_2 and k_3 are used in the reciprocal space sum, and affect the accuracy of the calculation in the three spatial directions (x, y and z).

3.4 Computational Details and Theory

3.4.1 Bulk Water Simulations

The simulation details for all the simulations that have been run on bulk water are shown in table 3.4. Each run was performed using the DL_POLY[125] program with the NpT ensemble (T = 300 K and p = 1 atm). 50,000 steps of equilibration were performed to begin with, to allow the molecules to randomise. Temperature and pressure were controlled by the Hoover-Nosé thermostat and barostat, with

relaxation time constants of 4.0 ps and 1.0 ps respectively. The molecules were fixed in a rigid geometry, allowing a large time-step of 2 fs. All periodic boxes were cubic. In the simulations which used the Ewald Sum scheme, the parameters used were $\alpha = 0.34$ and $k_1 = k_2 = k_3 = 7$. In the remaining runs, the Coulombic cutoff was the same as the Lennard-Jones cutoff.

Water Model	Electrostatic Cutoff Type	No. of Mols.	Box Size	No. of Steps	Cutoff Radius	Machine Used	CPU Time
SPC/E	Atomistic	216	(18 Å)^3	450,000	8.5 Å	DEC	0.67
SPC/E	Charge Group	216	(18 Å)^3	450,000	8.9 Å	DEC	0.96
SPC/E	Ewald Sum	216	(18 Å)^3	450,000	8.9 Å	DEC	1.22
TIP4P	Atomistic	216	(18 Å)^3	450,000	8.5 Å	DEC	1.21
TIP4P	Charge Group	216	(18 Å)^3	450,000	8.9 Å	DEC	1.41
TIP4P	Ewald Sum	216	(18 Å)^3	450,000	8.9 Å	DEC	2.34
TIP5P	Atomistic	216	(18 Å)^3	450,000	8.5 Å	DEC	2.72
TIP5P	Charge Group	216	(18 Å)^3	450,000	8.9 Å	DEC	2.43
TIP5P	Ewald Sum	216	(18 Å)^3	450,000	8.9 Å	DEC	3.00
SPC/E	Atomistic	1728	(37 Å)^3	313,580	8.5 Å		11.5
SPC/E	Charge Group	1728	(37 Å)^3	200,000	8.5 Å	DEC	7.00
SPC/E	Ewald Sum	1728	(37 Å)^3	200,000	8.5 Å	SUN	10.8
TIP4P	Atomistic	1728	(37 Å)^3	200,000	8.5 Å	SUN	13.4 *
TIP4P	Charge Group	1728	(37 Å)^3	200,000	8.5 Å	SUN	10.5
TIP4P	Ewald Sum	1728	(37 Å)^3	200,000	8.5 Å	SUN	16.8 *
TIP5P	Atomistic	1728	(37 Å)^3	159,000	8.5 Å		*
TIP5P	Charge Group	1728	(37 Å)^3	200,000	8.5 Å	DEC	19.0
TIP5P	Ewald Sum	1728	(37 Å)^3	200,000	8.5 Å	SUN	24 *

Table 3.4: Details of the various simulations of water that have been performed, and the timings for each run. Values presented in the 'Box Size' column are approximate as runs were carried out in the NpT ensemble. Cutoff radius is for both electrostatic (except Ewald Sum simulations) and Lennard-Jones interactions. Simulations marked "DEC" were run on a Dec 433 a.u. Simulations marked "SUN" were run on a SUN Ultrasparc II @ 450 MHz. CPU times are in days.
* Some runs have estimated timing data as they broke down and had to be restarted. One run has no timing information.

Three characteristic quantities can be calculated from these molecular dynamics simulations: the heat of vapourisation (equations 3.1 and 3.2), the isothermal compressibility (equation 3.3) and the density. Equation 3.2 is used under the assumption that the system forms an ideal gas, and that the molecules are rigid (i.e.

$E_{intra}(g)$ and $E_{intra}(l)$ are equal).

$$\Delta_{vap}H = [E_{intra}(g) + pV(g)] - [E_{intra}(l) + E_{inter}(l) + pV(l)] \tag{3.1}$$

$$\Delta_{vap}H = RT - E_{inter} \tag{3.2}$$

$$\kappa = [< V^2 > - < V >^2]/[k_bT < V >] \tag{3.3}$$

3.4.2 Water/Vapour Interface Simulation

In addition to the simulations of bulk water, two trial simulations of water interfaces were attempted. In order to reduce to a minimum the time taken by the simulation, the simplest water models, SPC/E and TIP4P, were chosen, and the Coulombic charge-group cutoff scheme was employed to prevent the ordering problems that occur with atomistic cutoffs. To start off these simulations, the end configurations of previous SPC/E and TIP4P runs were taken. The SPC/E configuration was taken from the end of a 1728 molecule simulation. The TIP4P configuration was obtained by taking the end-point of a 216 molecule simulation, and expanding the system by replicating the original simulation box. The box contents were duplicated in the x- and y-directions once and twice in the z- direction, giving 2592 molecules. Such large numbers of molecules are essential to ensure that the system displays bulk water character between the interfaces. The z-dimensions of the boxes were expanded from around 37 Å and 56 Å respectively, to 100 Å. Before the expansion of the box was done, however, molecules that were split across the sides of the cell were "repaired" by "unwrapping" the periodic boundary conditions, to prevent broken molecules being left in the middle of the box upon expansion.

As before, these new configurations were equilibrated for 50,000 steps of 2 fs, at $T = 300$ K. 172,000 steps of sampling dynamics were performed for the SPC/E model, and 500,000 for TIP4P. The NVT ensemble was selected for this simulation, and the Hoover-Nosé thermostat was used.

3.5 Results and Discussion

3.5.1 Bulk Water Simulations

Oxygen-oxygen radial distribution functions, calculated from the larger simulations, are shown in figure 3.5. These radial distribution functions clearly show the flaws in the Coulombic-atomistic cutoff scheme.[98] In both the SPC/E and TIP4P models, there are anomalous peaks in the oxygen-oxygen radial distribution function. Also shown is the oxygen-hydrogen radial distribution function for SPC/E (dotted line), which contains a similar anomalous trough.

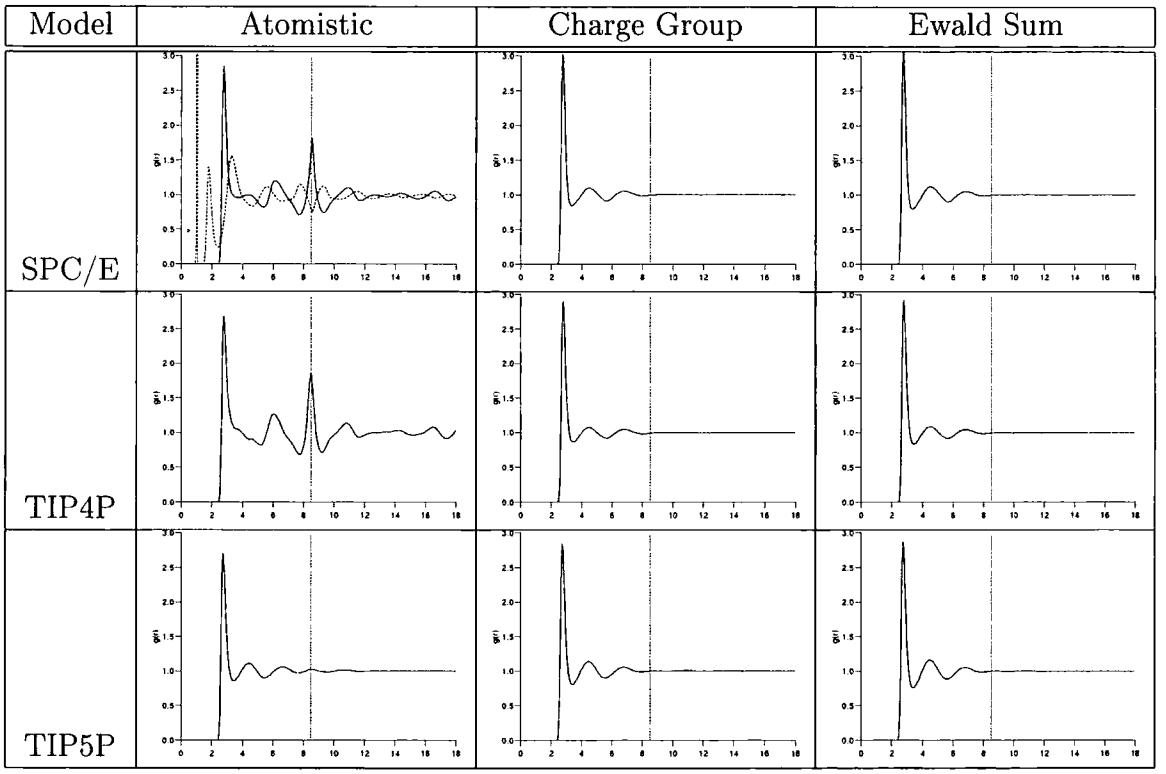

Figure 3.5: O-O radial distribution functions constructed from simulation data (1728 molecules) for the different water models and cutoff schemes. The dotted line shows the O-H radial distribution function. The vertical line marks the cutoff at 8.5 Å.

The reason for these anomalies is a simple one. In the case of the oxygen-oxygen radial distribution function, the peak represents a buildup of oxygen atoms just outside of the cutoff distance marked on the graphs. Since the Coulombic-atomistic method of calculating interactions only includes interactions within the cutoff dis-

tance, molecules can rearrange themselves to minimise the calculated energy of the system. Water molecules move to such a position that their oxygen atoms are outside of the cutoff distance of a central oxygen atom, but their hydrogen atoms are within this cutoff. This results in the unfavourable O-O interactions being excluded from the calculation (and also causes a buildup of oxygen atoms just outside of the cutoff). Similarly, favourable O-H interactions are included in the calculation. This causes a buildup of hydrogen atoms just inside the cutoff, and a depletion of hydrogen atoms just outside the cutoff, producing a trough in the radial distribution function. These anomalous artifacts in the radial distribution functions disappear when we move to charge group based cutoffs.

It is also interesting to note that there appears to be very little difference between the radial distribution functions produced using the TIP4P and TIP5P models, and also between the two best cutoff schemes (charge group based, and Ewald Sum). There only appears to be a slight heightening of the second peak in the O-O radial distribution function when going from TIP4P to TIP5P, which also appears in Jorgensen's original study[93] of a smaller system of 512 molecules. Jorgensen's results show better agreement between the radial distribution functions calculated in simulation and experimentally derived for real water for the TIP5P model than TIP4P.

Calculated values for the properties expressed in equations 3.1, 3.2 and 3.3 for the larger (1728 molecule) simulations, using all three cutoff schemes, are shown in table 3.5. These properties can also be calculated from the smaller (216 molecule) simulations (see table 3.6).

The experimental values[89] are shown in the table for comparison. Clearly a problem occurred in the simulation of TIP4P water under the Coulombic-atomistic cutoff scheme. The values of the heat of vapourisation and the isothermal compressibility both stand out as being very different to the others. Although these calculated values seem wrong, no problems can be found in the simulation files used to produce these results. The values Jorgensen[92] obtained were $\Delta_{vap}H = 10.66$ kcal mol^{-1} and $10^6\kappa = 35$ atm^{-1}. The fact that problems only occur with this model under a specific cutoff scheme seems to indicate that something went wrong only in

Simulation	$\Delta_{vap}H/kcal\,mol^{-1}$	$10^6\kappa/atm^{-1}$	$\rho/g\,cm^{-3}$
SPC/E CA	9.083	395	1.084
SPC/E CG	11.936	67.4	1.020
SPC/E ES	11.749	46.9	0.995
TIP4P CA	5.632	1.28	1.081
TIP4P CG	10.315	75.1	0.991
TIP4P ES	10.187	64.1	0.973
TIP5P CA	9.997	55.8	1.009
TIP5P CG	10.393	74.3	1.007
TIP5P ES	10.211	61.1	0.982
TIP4P MC	10.65	60	1.001
TIP5P MC	10.46	41	0.999
Experimental	10.51	45.8	0.997

Table 3.5: Properties of water calculated from the larger water simulations. Cutoff schemes used are shown with water model. CA is an atom based cutoff, CG is a charge-group based cutoff and ES is the Ewald Sum. MC denotes data taken from Jorgensen's Monte Carlo study.[93]

Simulation	$\Delta_{vap}H/kcal\,mol^{-1}$	$10^6\kappa/atm^{-1}$	$\rho/g\,cm^{-3}$
SPC/E CA	8.010	49.9	1.052
SPC/E CG	11.984	42.2	1.025
SPC/E ES	11.755	54.2	1.001
TIP4P CA	5.653	1.72	1.087
TIP4P CG	10.316	69.6	0.991
TIP4P ES	10.204	63.8	0.979
TIP5P CA	9.819	37.5	1.005
TIP5P CG	10.568	55.8	1.033
TIP5P ES	10.229	51.9	0.984
Experimental	10.51	45.8	0.997

Table 3.6: Properties of water calculated from the smaller water simulations. Cutoff schemes used are shown with water model. CA is an atom based cutoff, CG is a charge-group based cutoff and ES is the Ewald Sum.

these two simulations; however, the system studied by Jorgensen was smaller and was simulated using the Monte Carlo method rather than molecular dynamics.

All of the results for the density are close to experimental values, as are most of the isothermal compressibilities. Each of these water models seems to be good at reproducing experimental data. Jorgensen's study shows that these properties are better reproduced for the TIP5P model than TIP4P,[93] and this also appears to be the case here for the Ewald Sum simulations. The improvement in density for the charge-group study, however, is questionable. Jorgensen's reported improvement in isothermal compressibility is far more dramatic than the results seen here; the TIP5P values in the Ewald Sum simulations are particularly poor. The discrepancies between Jorgensen's results, and those seen here, could be due to the differences in simulation method; Jorgensen used the Monte Carlo method with 512 molecules, whereas the current study uses the molecular dynamics technique with 216 and 1728 molecules. In addition, it has been pointed out that the TIP5P water model may not perform as well as expected under a different cutoff scheme than that used in the original parameterisation of the model.[127]

3.5.2 Water Liquid/Vapour Interface Simulation

As the simulations proceed, two interfaces are formed, as shown by the density profiles in figures 3.6 (SPC/E) and 3.8 (TIP4P). Due to practical limits upon file sizes, recording of atomic positions was only possible once every 1,000 steps, so the density profiles have a ragged look through the bulk section, due to the low sampling rate. However, the average height of the density profile through this region is very close to the experimental density of water, indicating that both bulk and interfacial water types are present.

Two snapshots taken from the SPC/E simulation are also shown in figure 3.7. A slight increase in the spacing of the water molecules is evident at the surfaces of the slab in the mid-simulation snapshot, corresponding to a reduced density in the interfacial regions. Also, a single water molecule can be seen in the vapour, dissociated from the bulk material. This snapshot was taken at about 385 ps into the simulation, by which time the equilibration of the interfaces is complete.

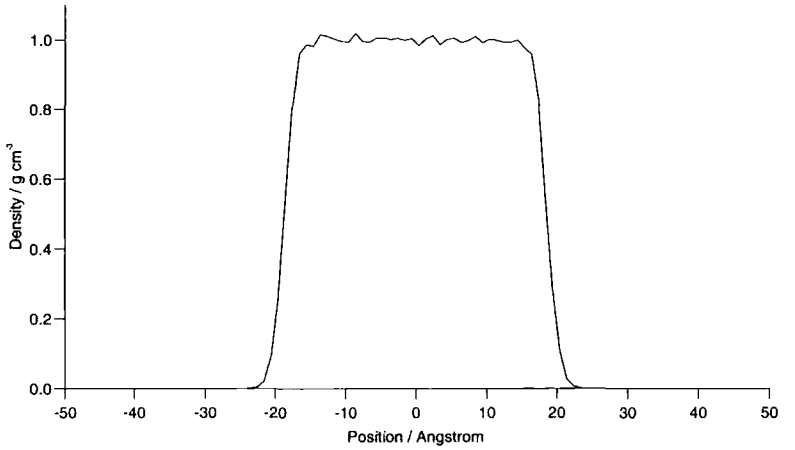

Figure 3.6: Density profile of a slab of SPC/E water which has formed two interfacial regions.

3.5.3 Study of Computational Cost

In order to assess the relative performance of the available hardware, very brief MD simulations of TIP4P water were performed, under the same conditions as the 216 molecule study using charge-group based cutoffs. The simulations were timed over 1,000 steps, using each of the available machines, including the powerful and newly introduced AMD systems which will be used in the main simulations of the amphiphilic polymer at an interface. The results are summarised in table 3.7.

Machine Used	CPU Time / s	Relative Speed
SUN	148.2	0.36
DEC	122.4	0.44
AMD	54.0	1.00

Table 3.7: Computational cost of a 1,000 step MD simulation of TIP4P water. "DEC" was a Dec 433 a.u. "SUN" was a SUN Ultrasparc II @ 450 MHz. "AMD" were run on an AMD Athlon @ 1500 MHz.

3.6 Conclusions

Various simulations of water have been carried out, and assessments made of computational cost (time) and cutoff scheme as well as the three water models used.

Figure 3.7: Two snapshots taken from the simulation of an SPC/E water interface. The upper image is the initial configuration, and the lower image is the configuration after 386 ps. Only oxygen sites are shown.

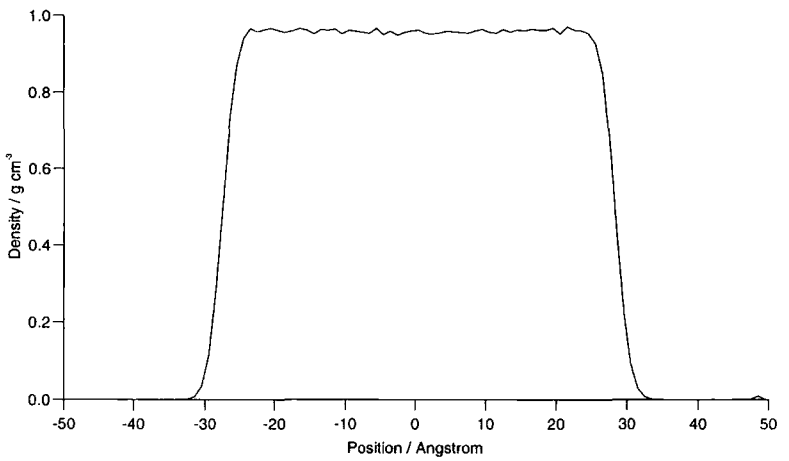

Figure 3.8: Density profile of a slab of TIP4P water which has formed two interfacial regions.

From these results, it has been decided that a TIP4P water model with a charge-group based cutoff scheme is the best compromise in terms of calculation quality vs. computational cost. In addition, a recent study[127] indicates that the TIP5P model is actually inferior to TIP4P in the reproduction of certain properties (including density) in simulations using different cutoff schemes to those employed in the original parameterisation. These findings are of sufficient concern to justify avoiding the TIP5P model in subsequent simulations involving water.

The TIP4P water model can successfully and accurately predict important water properties, particularly density. Since our simulations of an amphiphilic polymer at the air/water interface are going to be analysed structurally, it is logical to ensure that the system structure is as realistic as possible. Therefore the TIP4P model has been chosen over SPC/E and TIP5P. The latter model is only more suitable that TIP4P in the $0 - 4^{o}C$ temperature range, and has also been shown to suffer problems, so there is no justification for using this more expensive model. All structural artifacts have been eliminated from the radial distribution functions using the charge-group method, so again there is no real justification for using the significantly more expensive Ewald Sum technique. Finally, a large system of TIP4P water molecules has been encouraged to adopt an air/water interfacial configuration for use in further studies of an amphiphilic polymer at the water-air interface.

A brief analysis of computational cost has helped to plan out subsequent sim-

ulation work. The newly introduced AMD machines will allow significantly faster processing, which will be particularly beneficial when multi-processor parallel jobs are run. Such parallel computation with fast processors is essential in the large systems that are to be studied at the atomistic level (chapter 5).

Chapter 4

Developing a Force Field for Simulation of Poly(ethylene Oxide) Based upon ab Initio Calculations on 1,2-Dimethoxyethane

4.1 Introduction

1,2-Dimethoxyethane (DME) contains the two major dihedral interactions present in the polymer poly(ethylene oxide) (PEO) (C-O-C-C and O-C-C-O). Consequently, the conformational energies and populations of the former have been extensively studied experimentally[128–133] and theoretically[133–144] in the gas, liquid and aqueous phases to obtain better understanding of the conformational behaviour of the latter.

In 1993, Smith, Jaffe and Yoon performed *ab initio* electronic structure calculations on DME,[145] and used the results of these calculations to construct a force field[49] specifically for DME and PEO. This work, however, is now ten years old, and in the past decade, increasingly powerful computers have become more widely available. It was therefore decided to repeat the work, using higher levels of theory, and more computationally expensive but accurate basis sets. In addition to the advances in computational capability, there is a further motivation to repeat this work; although Smith used a reasonably good basis set and the MP2 level electron corre-

lation method for his final energy evaluations, the optimisations themselves were all carried out using the much less sophisticated HF method and a less extensive basis set. Although this practice is useful in saving computer time, it is does not give as good a set of results as performing the whole optimisation under the MP2 method, and the energies and geometries yielded can only be considered as estimates.

In the current work, the ten major conformations (*ttt*, *tgt*, *ttg*, *tgg*, *tgg'*, *ggg*, *ggg'*, *gg'g*, *gtg* and *gtg'*) and several major barriers (including *tct* and *ttc*) in DME, have been subject to *ab initio* geometry optimisation, and energy evaluation at the MP2 and B3LYP levels of theory, using a variety of basis sets. These optimised energies were then used to parameterise a force field for DME, which was refined by carrying out molecular dynamics calculations of DME in the liquid phase, in an attempt to obtain good agreement with experimental data.

This work is divided into a number of sections. Section 4.2 details some of the more important experimental and theoretical studies that have been done on DME. Section 4.3 contains details on the *ab initio* structure optimisation calculations that were performed on the DME molecule. Using results from these, section 4.4 focuses on the fitting of force field torsion parameters, to obtain a new force field that gives conformational energies in agreement with the *ab initio* study. Various attempts at fitting the force field parameters are detailed in this section in an attempt to get the best agreement possible between force field and *ab initio* energies, as well as force field and experimental bulk liquid phase conformational populations. A detailed study of DME's potential energy surface is then undertaken in section 4.5, in an attempt to determine the reasons for the conformational behaviour encountered in section 4.4. Finally, the work is summarised with conclusions in section 4.6.

4.2 1,2-Dimethoxyethane (DME) as a Model Molecule

Since DME is one of the shortest oligomers of PEO, it is not surprising that the former has been studied intensively by researchers wishing to understand the conformational and energetic behaviour of the latter. Despite DME's simple structure,

however, its conformational behaviour is quite complex. The five conformations that have been found experimentally to dominate DME's gas and liquid phases are shown in figure 4.1.

DME exhibits a strong *gauche effect*, where the *gauche* conformation of the central O-C-C-O dihedral is unusually highly-populated compared to the *trans* conformation. In fact many X-C-C-Y systems where X and Y are small electronegative groups exhibit greater stability in the *gauche* state than *trans*,[146] particularly 1,2-difluoroethane.[147,148] When X and Y are large polarisable groups, the *gauche* state is destabilised with respect to the *trans* state.[149]

4.2.1 Experimental Studies

A study of DME and related molecules by Ogawa *et al.*[128] aimed to determine which conformations were present in a number of different phases, including the vapour. This study confirmed the presence of the *ttt*, *tgt*, *ttg* and *tgg* conformations in gaseous DME.

In 1979, Astrup[129] used gas phase electron diffraction to estimate the conformational populations in DME, as well as various other structural information such as bond lengths and angles. This study indicated that the highly strained *gg'g* conformation was absent from the gas phase, which is not surprising given the highly energetic close contact between the two terminal methyl groups in this conformation. Astrup also noted that the *gg'* sequence in DME (*tgg'* and *ggg'* conformations) is more populated than the analogous conformations in *n*-hexane, which are of significantly higher energy. The importance of a 1,5-CH...O interaction in stabilising the *tgg'* conformation was also suggested.

Over a decade later, in 1992, Inomata and Abe studied DME's gas phase conformational populations using an RIS model[150] based upon NMR coupling constants.[132] Unfortunately, agreement between the electron diffraction study and the NMR study was particularly poor for the *tgt*, *tgg* and *tgg'* conformations. The remaining conformations, however, showed somewhat better agreement. The two studies do agree that the fraction of C-C bonds that are trans is around 20%, supporting the gauche effect. Agreement is somewhat poorer on the fractions of trans C-O bonds.

In the same year, a matrix-isolation infrared spectroscopic study of DME's gas phase was performed[133] at 18 K. This study confirmed the presence of the *ttt*, *tgt* and *tgg'* conformations in the vapour phase. It was also established that at higher temperatures (up to 45 K) the DME molecules begin to aggregate, and the *tgt* bands in the IR spectra become enhanced as the *ttt* bands decrease in intensity. This indicates that the *tgt* conformation is stabilised by intermolecular interactions. This work also confirmed the presence of a stabilising 1,5-CH...O interaction in the *tgg'* conformation, previously suggested by Astrup.

Further evidence supporting these ideas comes from another infrared spectroscopic study[130] performed in 1996, where the population of the *tgt* conformation is found to fall (while the *tgg'* population rises) when moving from the liquid to the gas phase. This study proposed an energy difference of 0.31 $\pm$ 0.04 kcal mol^{-1} between the *ttt* and *tgg'* conformations on the basis of these infrared spectroscopic studies. However, no energy difference was calculated for the *tgt* and *tgg'* conformations because the *tgt* signal was not easily distinguishable. This surprisingly small *ttt-tgg'* energy difference provides further evidence for a stabilising 1,5-CH...O interaction.

DME has also been experimentally investigated in the bulk liquid phase. The study of Ogawa *et al.*[128] confirmed the presence of the *ttt*, *tgt*, *ttg* and *tgg* conformations in bulk liquid DME. A Raman spectroscopic study[131] was performed in 2000 on liquid DME with a view to calculating the conformational populations in this compound. It was found that only five conformations (*ttt*, *tgt*, *ttg*, *tgg* and *tgg'*) are present in a detectable amount. This Raman spectroscopic study also included an investigation of the conformational behaviour of DME as the compound is diluted in aqueous solution; as concentration decreases, *ttt* and *tgg'* were found to decrease in population while *tgt* and *tgg* increased.

4.2.2 Theoretical Studies

DME has been studied even more intensively from a theoretical perspective. The study of Yoshida *et al.*[133] involved an *ab initio* quantum mechanical study on DME alongside the experimental, in which conformational energy differences were calculated. This study used only basic Hartree-Fock calculations, with no electron

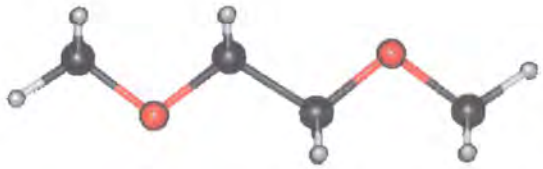

(a) ttt

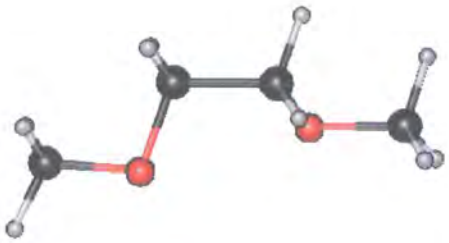

(b) tgt

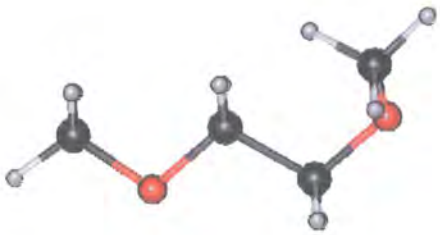

(c) ttg

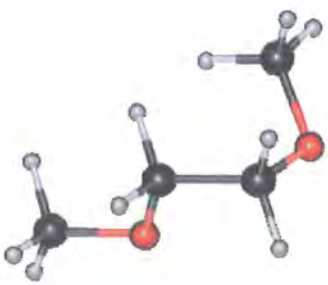

(d) tgg

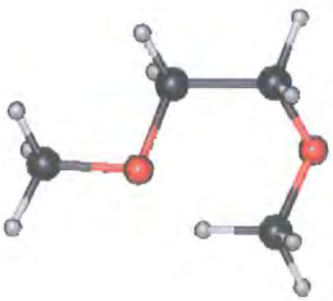

(e) tgg'

Figure 4.1: Low energy conformations of DME. The short 1,5-CH—O distance in the *tgg'* conformation indicates a possible internal hydrogen bond

correlation taken into account. As a result, the energies obtained are rather large.

Murcko and DiPaola used high-level *ab initio* calculations including electron correlation on selected conformations of DME and noted that the *ttt-tgt* energy difference decreases as electron correlation is included.

A study in 1995 used a combined quantum mechanical and molecular mechanical potential energy function to study the effects of solvation on the conformational equilibrium of DME.[143] In the same year, a variant of the molecular dynamics method was used to successfully reproduce the experimental observation that the crystalline phase of DME consists of the *tgt* conformation only.[141]

In 1996, Williams and Hall studied DME using molecular dynamics and force fields modified to agree with *ab initio* calculations.[144] In this work, the authors note that from past experimental and theoretical studies on DME, the *ttt* conformation is generally found to be the lowest in energy.

In terms of quantity, however, the theoretical side of DME studies is dominated by Smith and coworkers, who have done a great deal of work in the field. In 1993, Smith performed *ab initio* calculations[145] on the ten DME conformations listed in section 4.1, to investigate the relative energies of these conformations. With this data, Smith then developed a new force field[49] for the MD/MC simulation of DME and PEO. Smith's 1995 molecular dynamics study of DME showed that in the gas phase, the *tgg'* and *ttt* conformations are more populated, and *tgt* is less populated than in the liquid phase, in agreement with the following year's infrared spectroscopic study.[130]

In 1998, Smith performed further *ab initio* calculations, in order to develop force field parameters[135] for the interaction of water and DME/PEO. These new force field parameters were then used in simulations of aqueous DME.[134] These simulations show conformational behaviour in good agreement with the later Raman spectroscopic study[131] as the DME concentration is varied.

Unfortunately, Smith's force field fails to accurately reproduce the experimental liquid-phase conformational populations of Goutev *et al.*[131] In particular, the *tgt* conformation is overpopulated in simulation, and the *tgg'* conformation is significantly underpopulated. Also, Smith's force field is based upon *ab initio* calculations

that used one level of theory for the optimisations and a higher level of theory for energy evaluations. While this practice saves on computer time, it is not generally a safe thing to do because the optimised structure found at the lower level of theory could well be different to the corresponding optimised structure at the higher level of theory. Today, higher basis sets can be reached than ten years ago, due to the wider availability of more powerful processors.

Accordingly, it was decided to investigate the problem of DME and its conformational equilibrium with a view to improving on Smith's force field, allowing better quality simulations of PEO systems.

4.3 *Ab Initio* Structure Optimisations of DME

The Gaussian 98[151] software package was used to scan the potential energy surface of DME, as its two major dihedrals were separately rotated through 180 degrees (figure 4.2). Due to the symmetry of the system, the remaining 180 degrees of rotation had the same energy profile. The O-C-C-O *cis* barrier is somewhat higher than its C-O-C-C counterpart; this is due to both a strong electrostatic repulsion between the two electronegative oxygen atoms which are at minimum separation at this barrier, and two 1,4 H-H overlaps that occur in the former but not the latter.

The ten energy-minimum conformations of DME along with several rotational barriers were also optimised, using a number of different basis sets under two quantum methods, MP2 and B3LYP. Again because of the symmetry of the DME molecule, these ten conformations are fully representative of the twenty-seven true energy-minimum conformations.

The first attempt at obtaining new torsion parameters for the DME molecule involved running a least-squares fit based upon the differences in *ab initio* and force field energies for the DME dihedrals obtained from the potential energy surface scans. Subsequent attempts focus more upon matching the energies of the energy minima and barriers.

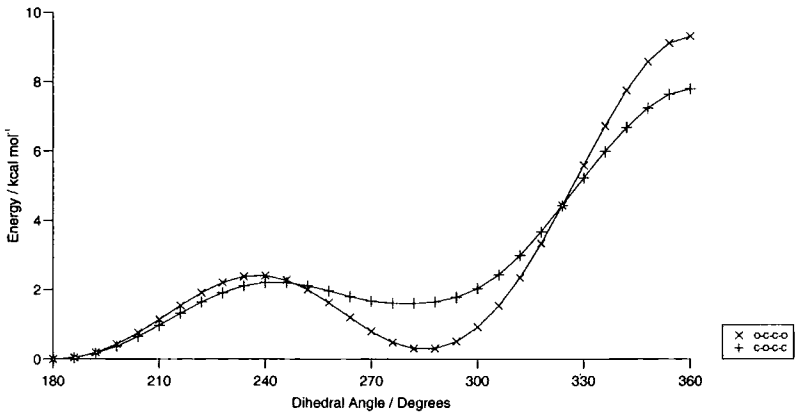

Figure 4.2: Relaxed potential energy surface (PES) scan for rotation about the two major dihedrals in DME (all other major dihedrals in *trans* state), obtained using *ab initio* methods, at the MP2/6-31++G'(d,p) level of theory. All energies are relative to the *ttt* conformation. Energies calculated at six degree intervals.

4.3.1 MP2 Optimisations

The MP2 method was used to optimise the DME molecule for a range of basis sets, as shown in table 4.1. In some cases, no minimum was found for the *gg'g* conformation, due to the unfavourable close contact between the two terminal methyl groups.

The first thing that is noticeable about these results is that all of the higher-order basis-sets give the *ttt* conformation as the global minimum. Unfortunately, there does not appear to be any significant degree of convergence in these results. In particular, the energy of the *tgt* conformation varies greatly, from 0.19-0.57 kcal mol $^{-1}$ within the 6-31 family of basis sets. In addition the *tgt* and *tgg'* conformations take different relative positions in order of energy with different basis sets. Results for the *ttg*, *tgg* and *gtg* conformations, and *tgt-tgg'* and *ttg-tgg'* barriers show some convergence within the 6-31G basis set family.

A set of full optimisations were performed using MP2/D95+(2df,p), the basis set and method used by Smith only in the energy calculation step after optimising with the SCF/D95** method, in order to assess the validity of this practice. It is immediately clear that, with the exception of *ttg*, all of Smith's relative energies are higher than the ones in this study. This is most likely because the optimised structures from the SCF calculation are not energy minima on the MP2/D95+(2df,p) potential energy surface used in Smith's energy evaluation. The small discrepancy in

MP2	Basis Set							
Conformation	STO-3G	3-21G	4-21G	6-31G(d)	6-31++G'(d,p)	6-311++G(d,p)	6-311++G(2d,2p)	D95+(2df,p)
ttt	0.00	1.55	1.54	0.00	0.00	0.00	0.00	0.00 (0.00)
tgt	0.34	3.17	3.09	0.57	0.28	0.19	0.31	0.09 (0.15)
ttg	1.21	2.58	2.57	1.47	1.60	1.51	1.47	1.45 (1.43)
tgg	1.56	4.12	4.06	1.88	1.88	1.72	1.70	1.33 (1.51)
tgg'	0.28	0.00	0.00	0.09	0.42	0.41	0.46	0.12 (0.23)
ggg	2.13	1.87	1.93	1.74	1.80	1.39	1.76	1.29 (1.64)
ggg'	1.54	0.99	1.02	1.60	2.21	2.08	2.02	1.65 (1.86)
gg'g	3.88	2.27	*	2.07	2.57	2.45	2.32	* (2.41)
gtg	2.36	3.68	3.65	3.01	3.33	3.23	3.00	3.04 (3.13)
gtg'	2.40	3.29	3.27	2.84	3.22	3.13	2.91	2.93 (3.08)
tct	4.32	11.89	11.73	9.17	9.30	9.20	8.78	8.74 (8.90)
ttc	7.05	8.22	8.30	7.75	7.78	7.73	6.97	7.25
tgt-tgg'					1.50	1.34	1.49	(1.36)
ttg-tgg'					2.92	2.90	2.84	(2.03)

Table 4.1: Optimised energies of various conformations and barriers in DME, using the MP2 method with various basis sets. All energies are in kcal mol^{-1}, and are relative to the lowest energy conformation in each case.
* No energy minimum found for this conformation. Values in parentheses are Smith's optimised energies.[49]

the *ttg* energy is probably due to rounding errors in the calculations and conversions from atomic units to kcal mol $^{-1}$.

Some of Smith's relative energies using HF/D95**//MP2/D95+(2df,p) are considerably higher than energies obtained in this study with MP2/D95+(2df,p)// MP2/D95+(2df,p) (the energy minima on the MP2/D95+(2df,p) potential energy surface). Such differences include the energies for the *tgt* and *tgg'* conformations, which are the conformations that suffer the greatest error already in force field based simulation. It is clear, therefore, that any *ab initio* optimisation should be performed at the same level of theory as the subsequent energy evaluation.

Basis Set	ttt	tgt	ttg	tgg	tgg'
6-31G(d,p)	0.00	0.55	1.38	1.74	0.02
6-31G(2d,p)	0.43	0.53	1.67	1.51	0.00
6-31+G(d,p)	0.00	0.46	1.47	1.91	0.14
6-311G(d,p)	0.00	0.52	1.44	1.70	0.02

Table 4.2: Optimised energies of the five conformations of DME found in the liquid phase, using the MP2 method, and the 6-31G family of basis sets. All energies are in kcal mol $^{-1}$, and are relative to the lowest energy conformation in each case.

An additional study was done, focusing particularly on the five key conformations present in the liquid phase of DME, the results of which can be seen in table 4.2. This study was done using the MP2 method and various improvements to the 6-31G(d,p) basis set, in line with a similar analysis of benzyl fluoride, by Tozer.[152]

In this case, we observe no significant energy differences when adding extra valence functions (6-311G(d,p)), and only small differences when adding diffuse functions (6-31+G(d,p)). By far the most significant effect is observed when additional polarisation functions are introduced for heavy atoms (6-31G(2d,p)). Using this basis set, the order of the conformations in energy changes, with *tgg'* now being the global minimum. These results confirm that even at the 6-31G family of basis sets, satisfactory convergence has not been obtained.

It may also be the case that the MP2 method is inadequate for this task. Although MP2 is an electron-correlation method, it generally only predicts about 80% of the dispersion energy in molecular systems. In particular, the MP2 method may be underestimating the van der Waals interactions between the oxygen and hydro-

gen atoms in the *tgg'* conformation, where these atoms are in close proximity to one another. This van der Waals interaction is likely to be small (but not necessarily insignificant) compared to the electrostatic (hydrogen-bonding) interaction between the oxygen and hydrogen atoms. This electrostatic interaction may also be underestimated within the MP2 method.

Due to current limitations in computational power, higher basis sets (e.g. cc-pVDZ, aug-cc-pVTZ, etc) and methods, coupled-cluster being the most accurate method available today, are not easily applicable to such a large system as DME. There are some studies that use focal-point extrapolations[153,154] to obtain estimates of conformational energies at levels of theory that are too expensive to run on current processors. Perhaps such a detailed study on DME will result in a set of conformational energies that are close to the true energies of the system.

4.3.2 B3LYP Optimisations

To assess the applicability of Density Functional Theory (DFT) to this system, and to give a basis for comparison with MP2 results, the B3LYP method was also used to optimise the DME molecule for a range of basis sets, as shown in table 4.3. The B3LYP method appears to have more difficulty in optimising the *gg'g* conformation than MP2.

The B3LYP method returns higher energies for the *tgg'* conformation than MP2, and the results are somewhat more consistent than those in table 4.1. In particular, within the 6-31G basis-set family, the *tgt* conformation has a much more consistent set of energies. In both the MP2 and B3LYP cases, the 6-31G(d) energy for *tgg'* is significantly lower than the remaining energies in this basis-set family. The *tct* and *ttc* barrier energies are slightly smaller with the B3LYP method than MP2.

B3LYP	Basis Set							
Conformation	STO-3G	3-21G	4-21G	6-31G(d)	6-31++G'(d,p)	6-311++G(d,p)	6-311++G(2d,2p)	D95+(2df,p)
ttt	0.66	1.73	1.73	0.00	0.00	0.00	0.00	0.00
tgt	0.90	3.16	3.09	0.52	0.48	0.46	0.33	0.26
ttg	1.45	2.70	2.70	1.41	1.70	1.63	1.57	1.59
tgg	1.76	4.06	4.02	1.89	2.17	2.11	1.89	1.79
tgg'	0.00	0.00	0.00	0.32	0.81	0.72	0.80	0.70
ggg	2.10	2.16	2.21	2.63	3.04	2.87	2.88	2.71
ggg'	0.93	0.99	1.01	1.86	2.74	2.59	2.58	2.48
gg'g	*	*	*	2.88	*	*	3.16	*
gtg	2.22	3.78	3.75	2.96	3.58	3.45	3.31	3.36
gtg'	2.12	3.38	3.36	2.78	3.35	3.22	3.13	3.18
tct	4.93	11.74	11.60	8.42	8.83	8.90	8.34	8.38
ttc	7.06	8.06	8.16	7.15	7.41	7.39	7.11	7.12

Table 4.3: Optimised energies of various conformations and barriers in DME, using the B3LYP method with various basis sets. All energies are in kcal mol $^{-1}$, and are relative to the lowest energy conformation in each case.
* No energy minimum found for this conformation.

4.4 Fitting Force Field Torsion Parameters to *Ab Initio* Data

The commonly used OPLS-AA force field,[45] which was designed with the simulation of small, organic molecules in mind, does not perform particularly well in the simulation of DME. Specifically, the conformational populations in bulk liquid DME are in poor agreement with experiment. A typical MD simulation of liquid DME with the OPLS-AA force field, such as that shown in table 4.4, underestimates the quantity of molecules in the *tgg'* conformation, and overestimates the population of the *tgt* conformation.

Conformation	MD Population	Raman Population
ttt	13.54%	12%
tgt	50.31%	42%
ttg	5.16%	4%
tgg	13.01%	9%
tgg'	14.60%	33%
ggg	1.39%	~ 0
ggg'	1.39%	~ 0
gg'g	0.13%	~ 0
gtg	0.25%	~ 0
gtg'	0.22%	~ 0

Table 4.4: Populations of DME's conformations from a molecular dynamics simulation using the OPLS-AA force field, and Raman Spectroscopic experiment.

The energies of the minimised conformations using the OPLS-AA force field also differ quite significantly from the energies obtained using high-level *ab initio* structure optimisations. These facts are sufficient motivation to fit the force field torsion parameters to such high-level *ab initio* calculations, in order to obtain a force field that better represents the DME molecule in the gas phase. In turn it is hoped that this good representation will transfer well to the bulk liquid phase, and

to poly(ethylene oxide) chains in aqueous solution.

4.4.1 Fitting Procedure

Using the results of the *ab initio* optimisations, a series of least-squares fits (detailed below) were performed on the OPLS-AA force field energy, by adjusting the torsion parameters. The original fitting procedure involved fitting to a rotational energy profile; for each *ab initio* data point that a dihedral angle and energy evaluation existed, the square of the difference between the minimised force field (with varying dihedral constrained and all other degrees of freedom fully relaxed) and *ab initio* energies was calculated. These squared differences were accumulated to give an overall parameter, χ^2, which characterised the quality of the force field with respect to the quantum calculations, and which itself was minimised through systematic adjustments to the torsion parameters. In this procedure, the force field and *ab initio* energies are both converted in such a way that each energy in both sets is relative to the minimum energy data point in that set, so that agreement is obtained in the relative energies of the conformations. The absolute energies are not important, as it is only energy differences that influence conformational distributions. The calculation of χ^2 is shown in equation 4.1,

$$\chi^2 = \sum (\Delta E_{i,a} - \Delta E_{i,f})^2, \tag{4.1}$$

where

$\Delta E_{i,a}$ = *ab initio* energy of conformation i relative to ground state (lowest energy conformation), and

$\Delta E_{i,f}$ = force field energy of conformation i relative to ground state.

This procedure has previously been used to parameterise a force field for molecules exhibiting liquid-crystalline properties.[155]

4.4.2 Testing Procedure

Once fitted torsion parameters have been obtained, it is necessary to test them in a bulk liquid MD simulation of DME, in order to assess how well the force field

reproduces experimentally determined conformational populations.

The testing procedure used was the same for all trial force fields, and made use of the DL_POLY molecular dynamics simulation code.[125] Periodic boundary conditions were employed, with a cubic box geometry. Simulations occurred under the NpT ensemble, and were performed at $p = 1$ atm, and $T = 300$ K to correspond to the results obtained in the Raman spectroscopic study. The starting configuration used was a randomised box of 343 DME molecules; this initial configuration was taken from the end point of a previous simulation using the unmodified OPLS-AA force field. Total simulation time came to 750,000 time-steps (1 fs time-step, with first 50,000 steps as equilibration) and a charge-group based cutoff of 7.5 Å was used. The DME molecules in these simulations were split into two charge groups, each comprising exactly half of the DME molecule. Atomic coordinates used to calculate conformational populations were dumped once every 500 time-steps. All degrees of freedom within the molecules were left unconstrained.

Conformational populations were sampled across five time-windows in the simulation trajectory data, to ensure that the system had reached equilibrium.

4.4.3 Fitting to *Ab Initio* Rotational Energy Profiles

Gaussian 98 was used to perform fully relaxed *ab initio* potential energy surface (PES) scans. These calculations were essentially *ab initio* dihedral driver calculations on the C-O-C-C and O-C-C-O dihedrals. The *ab initio* studies were initially carried out at the MP2/6-31++G'(d,p) level, and results were obtained for dihedral increments of six degrees.

Early fit attempts based upon the three-term cosine torsion potential of the OPLS-AA force field gave rise to quite high χ^2 values, and it was decided to adopt a four-term cosine torsion potential to achieve better fits.

The first four-term fit considered comprised of rotation about one of the terminal C-O-C-C dihedrals (*ttx* scan), followed by rotation about the central O-C-C-O dihedral (*txt* scan) in a separate fit (using previously fitted C-O-C-C parameters). In both rotations, the remaining two backbone dihedrals were left in the *trans* conformation. While the match between the force field and *ab initio* energies was excellent

($\chi^2 = 0.18$ kcal^2 mol^{-2} over 60 data points), and the two rotational energy profiles are virtually coincident (figures 4.3 and 4.4), some of the conformational energy minima are very different between the two methods (table 4.5). This is primarily because the force field parameters have been fitted using only data involving two *trans* dihedrals and one variable dihedral.

In order to obtain a more realistic match between the *ab initio* data and the force field, another fit was performed with additional data. This additional data took the form of yet another relaxed PES scan of the C-O-C-C dihedral, with the O-C-C-O dihedral this time in the gauche conformation (*tgx* scan).

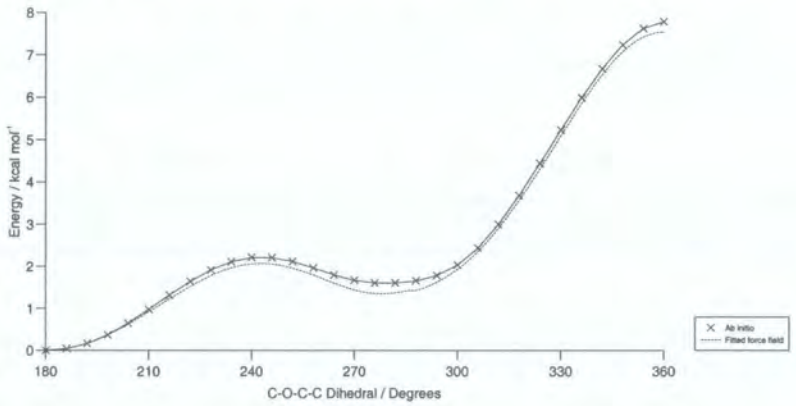

Figure 4.3: Comparison of the *ab initio* (solid line) and fitted force field (dashed line) energy profiles resulting from a relaxed rotation about the C-O-C-C dihedral. All energies are relative to the *ttt* conformation. *Ab initio* energies calculated at six degree intervals. Force field energies calculated at two degree intervals (points omitted for clarity).

Unfortunately, this fit was significantly poorer in quality ($\chi^2 = 8.40$ kcal^2 mol^{-2} over 120 data points), and although some of the conformations have moved closer to their *ab initio* energies, others have moved further away. In terms of conformational energies, this fit is no better overall than the previous one.

4.4.4 Fitting to Rigid Conformational Energy Minima

After the failure of the rotational profiles in the first two fits, a new approach was considered. In this set of fits, the actual *ab initio* energy minima are used, rather than data from relaxed PES scans. This time, the three main dihedrals are

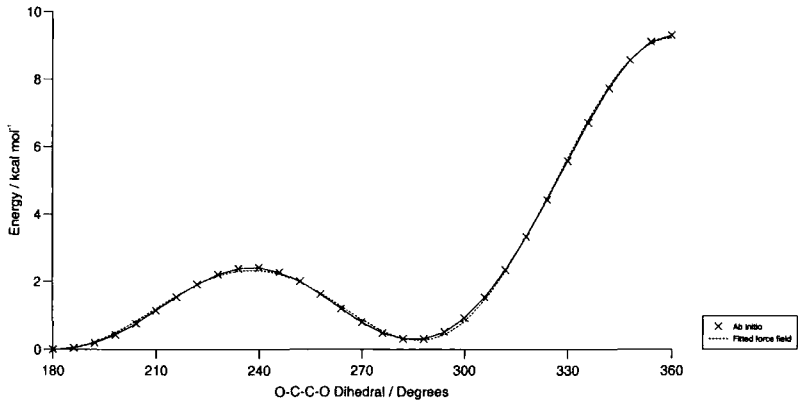

Figure 4.4: Comparison of the *ab initio* (solid line) and fitted force field (dashed line) energy profiles resulting from a relaxed rotation about the O-C-C-O dihedral. All energies are relative to the *ttt* conformation. *Ab initio* energies calculated at six degree intervals. Force field energies calculated at two degree intervals (points omitted for clarity).

Conformation	*Ab initio* energy	Fitted force field energy
ttt	0	0
tgt	0.27855	0.204934
ttg	1.60122	1.325809
tgg	1.88240	1.754200
tgg'	0.41547	-0.195567
gtg	3.33427	2.558786
gtg'	3.21825	2.406105
ggg	1.80422	2.634036
ggg'	2.20589	1.254686
gg'g	2.57643	1.644981

Table 4.5: Conformational energy minima from fitted force field. All energies are in kcal mol $^{-1}$, and are relative to the *ttt* conformer.

constrained to the *ab initio* geometries while the remaining degrees of freedom in the molecule are relaxed, and χ^2 is minimised. Unfortunately, despite obtaining low χ^2 values in these fits, it quickly became apparent that a particular energy-minimised *ab initio* geometry for a particular conformation is not necessarily (and in fact is highly unlikely to be) identical to the corresponding force field energy-minimised geometry. For example, table 4.6 shows the energies involved in the *tgt* conformation. The force field was fitted such that at the *ab initio* geometry, the two energies would match. Even though this fit clearly isn't a particularly good one, the result is made worse by the fact that the *ab initio* geometry is very different to the true energy-minimum geometry for the fitted force field. It turns out that the true force field energy-minimum in this case is even further from the *ab initio* energy value than the already poor fit.

tgt	C-O-C-C	O-C-C-O	C-C-O-C	Optimised Energy
Ab initio	-174.353	75.004	-174.583	0.27855
Force field (rigid)	-174.353	75.004	-174.583	0.16252
Force field (relaxed)	-174.066	66.414	-174.095	0.05169

Table 4.6: *Ab initio* and force field energies for the *tgt* conformation from a fit where the three dihedrals were kept rigid. All energies are relative to the *ttt* conformation and in kcal mol^{-1}. All dihedral angles are in degrees.

This limitation in the fitting procedure is clearly too significant to ignore, so yet another fitting procedure was devised.

4.4.5 Fitting to Relaxed Conformational Energy Minima

The fitting procedure was further modified, such that the major dihedrals are no longer constrained to the *ab initio* geometry. In this procedure, the χ^2 value is calculated as the sum of the squares of the differences between the *ab initio* energies and the *fully relaxed* force field minimum energies. Although this allows the geometries of the force field energy-minima to deviate further from their *ab initio* counterparts, the actual energy values for each conformation should be in much better agreement. Indeed this is found to be the case, as illustrated in one of the better fits that have been performed to date, in table 4.7.

Conformation	*Ab initio* energy	Fitted force field energy
ttt	0	0
tgt	0.27855	0.278821
ttg	1.60122	1.601281
tgg	1.88240	1.882729
tgg'	0.41547	0.412086
gtg	3.33427	3.196450
gtg'	3.21825	2.905921
ggg	1.80422	2.898923
ggg'	2.20589	1.948661
gg'g	2.57643	2.527307

Table 4.7: Comparison of *ab initio* and force field energies for the best fit obtained to date. All energies are in kcal mol^{-1}, and are relative to the *ttt* conformation. The torsion parameters used were as follows:
C-O-C-C: 0.8066, -0.3482, 0.7380, -0.0296
O-C-C-O: 1.2228, -2.0187, 2.3394, 0.2804

The fit shown in table 4.7 was performed using the five conformations (*ttt*, *tgt*, *ttg*, *tgg* and *tgg'*) which coexist in the liquid phase of DME, as measured using Raman spectroscopy. In addition, two major inter-conformational barriers (*tct* and *ttc*) were also included in the fit. In order to use barrier conformations in a fit, the fitting procedure was once again slightly modified, to allow selective constraints, ensuring that the barriers remain at the *ab initio* geometries while the minima are fully optimised. The quality of the fit for the energy-minimum conformations used in the fitting process is very good ($\chi^2 = 1.16 \times 10^{-5}$ kcal^2 mol^{-2}), and even the remaining conformations have reasonably good agreement with *ab initio* energy values. Only the *ggg* conformation has a poor match for energy in the fitted force field, but since the population of the *ggg* conformation in bulk liquid DME is negligible, this can be overlooked.

Despite the extremely good fit, when these torsion parameters are tested in a molecular dynamics simulation of liquid DME using the DL_POLY[125] program, the resulting conformational populations do not match the measurements taken using Raman spectroscopy, as table 4.8 shows. Conformational populations are calculated across five different time-windows to verify that the system is at equilibrium, and not changing significantly throughout the simulation.

	Molecular Dynamics Step Number						
Conformation	50,000-190,000	190,000-330,000	330,000-470,000	470,000-610,000	610,000-750,000	50,000-750,000	Raman
ttt	11.89%	11.82%	11.05%	7.77%	8.99%	10.30%	12%
tgt	52.38%	53.17%	54.47%	56.51%	54.91%	54.29%	42%
ttg	3.99%	4.62%	4.14%	3.28%	3.22%	3.85%	4%
tgg	9.93%	9.61%	9.48%	9.91%	10.23%	9.83%	9%
tgg'	18.78%	17.84%	18.32%	19.61%	19.84%	18.88%	33%
ggg	0.58%	0.56%	0.46%	0.48%	0.47%	0.51%	~ 0
ggg'	2.01%	1.83%	1.68%	2.01%	1.93%	1.89%	~ 0
gg'g	0.13%	0.09%	0.11%	0.12%	0.09%	0.11%	~ 0
gtg	0.16%	0.23%	0.13%	0.15%	0.17%	0.17%	~ 0
gtg'	0.16%	0.22%	0.16%	0.17%	0.15%	0.17%	~ 0

Table 4.8: Populations of DME's conformations from a molecular dynamics simulation using the torsional parameters from table 4.7. All other force field parameters used are from the OPLS-AA force field.

The force field clearly does well in representing the higher energy conformations; they are of low population in the molecular dynamics simulation, in agreement with experimental data. Also, three of the lower energy conformations (*ttt*, *ttg* and *tgg*) are very close in population to experimental observations. Unfortunately the two remaining conformations (*tgt* and *tgg'*) are significantly different from their experimental values, and all subsequent work has been focused on trying to reduce the population of the *tgt* conformation, while increasing the population of *tgg'*.

4.4.5.1 Fitting to Different Basis Sets

Fits were attempted to all of the available *ab initio* energies given by the 6-31G family of basis sets using the MP2 method (shown in table 4.1). Unfortunately, no significant differences were noted in MD liquid phase populations between these various fits.

4.4.5.2 Weighting χ^2

Several fits were performed using all ten *ab initio* optimised energies and two major barriers, in which the χ^2 function was altered. In the first attempt, each contribution to χ^2 was given a Boltzmann weight, shown in equation 4.2,

$$\chi^2 = \sum e^{\left(\frac{-\Delta E_{i,a}}{k_B T}\right)} \left(\Delta E_{i,a} - \Delta E_{i,f}\right)^2, \tag{4.2}$$

where

$\Delta E_{i,a}$ = *ab initio* energy of conformation i relative to ground state (lowest energy conformation), and

$\Delta E_{i,f}$ = force field energy of conformation i relative to ground state.

In the second attempt, χ^2 was the sum of the squares of the percentage errors in the force field energies based upon the *ab initio* energies, as shown in equation 4.3,

$$\chi^2 = \sum \left(\frac{100\left(\Delta E_{i,f} - \Delta E_{i,a}\right)}{\Delta E_{i,a}}\right)^2, \tag{4.3}$$

In both of these cases, the χ^2 function is weighted such that the lower energy conformations have a larger contribution to χ^2 than higher energy conformations. The original intent was to ensure that the force field represented the lower energy (and in the liquid phase, dominant in population) conformations better, at the expense of accuracy in the higher energy ones. However, there turned out to be no advantage to this approach as the liquid phase populations from a molecular dynamics test of the fitted parameters showed no significant improvement on previous fits.

4.4.5.3 Modifying C-O-C-H Torsion Parameters

Since the *tgg'* conformation has a surprisingly low energy courtesy of its internal hydrogen bond, the possibility was considered that the formation of this hydrogen bond may be in some way hindered in the force field representation of the DME molecule. A comparison was made between the OPLS-AA force field and *ab initio* energy profiles for rotation about the hydrogen-bonding C-O-C-H dihedral in *tgg'* (figure 4.5), and it was found that the force field gave slightly higher barriers than the *ab initio* representation. However, when fits were attempted with a reduced barrier

height for this dihedral, very little change was noticed in the molecular dynamics conformational populations of bulk liquid DME.

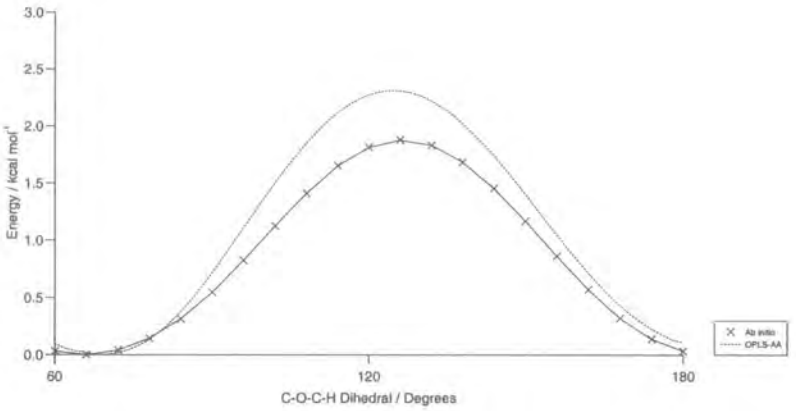

Figure 4.5: *Ab initio* and force field energy profiles for the rotation of the terminal methyl group of DME in the *tgg'* conformation. The *ab initio* energy is calculated at intervals of six degrees, hence the rough appearance of the curve. All energies are relative to the local energy-minimum for this rotation. Force field energies calculated at two degree intervals (points omitted for clarity).

4.4.5.4 Including Extra Inter-Conformational Barriers

In order to better represent the *tgg'* conformation, it was decided to try to fit the force field to two extra *ab initio* data points (the *tgt-tgg'* and *ttg-tgg'* barriers). It was felt that if the force field representation of these barriers was of too low an energy, then the *tgg'* population could more easily "leak out" into neighbouring conformations' (*tgt* and *ttg*). Conversely, if the barriers were too high, then this could cause access to the *tgg'* conformation to be restricted.

Figure 4.6 compares the height of the *ttg-tgg'* barrier, using the original unmodified OPLS-AA force field, an attempted fit which included this barrier and the *ab initio* data calculated for the same barrier. The fitted barrier is in much better agreement with the *ab initio* data than the original OPLS-AA force field. In addition, the *tct* barrier is grossly underestimated in OPLS-AA with respect to *ab initio* calculations which give 9.30 kcal mol^{-1} relative to *ttt*. This has also been rectified in the fit. The *ttt-ttg* energy difference is in good agreement between the two force fields at 1.58 kcal mol^{-1} for OPLS-AA, 1.56 kcal mol^{-1} for the fitted force field, and 1.60 kcal mol^{-1} using MP2/6-31G'++(d,p).

Figure 4.7 shows the other barrier (*tgt-tgg'*). In this case, the fitted force field representation is not as good since the fitted barrier is as far below the *ab initio* data as the original OPLS-AA barrier is above it.

Despite the radical changes to the *ttg-tgg'*, *tgt-tgg'* and *tct* barrier energies in this fit, there is no significant improvement in the molecular dynamics population for the *tgg'* conformation which is at 14.55% for OPLS-AA, and 18.43% for the fitted force field. These populations are still a long way short of the reported 33% from liquid phase Raman spectroscopy.

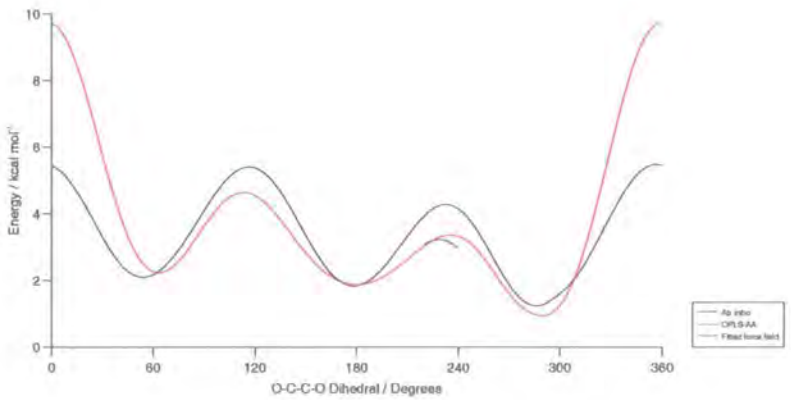

Figure 4.6: Dihedral driver calculation for rotation about the O-C-C-O dihedral, showing various conformations and barriers. Minima from left to right: *tgg*, *ttg* and *tgg'*. Ab initio data shown for the *ttg-tgg'* barrier. All energies relative to *ttt* energy in each case. All energies calculated at two degree intervals (points omitted for clarity).

4.4.5.5 Using Experimentally Determined Populations as a Basis For Energies

Using the experimentally determined populations of the five low-energy conformations of DME, a new set of relative energies was derived. Energies were determined from the Boltzmann probability, using equation 4.4,

$$p_i = \frac{N_i}{N} = \frac{e^{\left(\frac{-\Delta E_i}{k_B T}\right)}}{Q} \tag{4.4}$$

where

$p_i = \frac{N_i}{N}$ = Boltzmann probability of conformation i (fractional population of con-

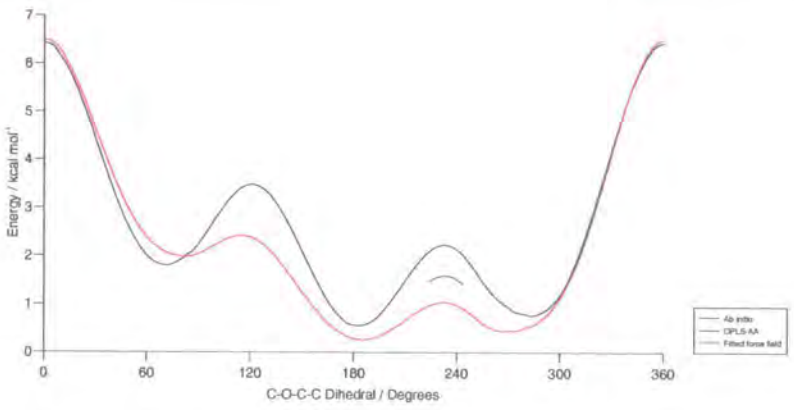

Figure 4.7: Dihedral driver calculation for rotation about the C-O-C-C dihedral, showing various conformations and barriers. Minima from left to right: *tgg*, *tgt* and *tgg'*. Ab initio data shown for the *tgt-tgg'* barrier. All energies relative to *ttt* energy in each case. All energies calculated at two degree intervals (points omitted for clarity).

formation i),

ΔE_i = Energy of conformation i relative to ground state (lowest energy conformation), and

Q = Partition function.

An approximate value of Q is easily obtained since we know the population of each of the conformations, and we can assume that the *tgt* conformation is the lowest energy conformation because of its high experimental population in the liquid phase, and also because this conformation is the only one present in solid, crystalline DME. Making the further assumption that the tg^+t and tg^-t conformations are equally populated, we can calculate Q using

$$Q = \frac{100}{(N_{tgt}/2)},$$

and giving $Q = 4.7619$ (with $N_{tgt} = 21\%$).

Since we now know Q and each p_i value (from the experimental study), extracting the energy of each conformation from equation 4.4 is trivial. In calculation of these energies, however, the multiplicity of each conformation must be taken into account.

Although this technique strictly applies only in the gas phase, it was still considered instructive to investigate exactly *how* the conformational populations of DME

in molecular dynamics simulations vary with fitted energies. Table 4.9 shows the calculated energies of the conformations, along with the populations from molecular dynamics simulation.

Conformation	Multiplicity	Raman Population	Relative Raman Energy / kcal mol^{-1}	Force Field Energy	Force Field Population
ttt	1	12%	0.33	0.22	17.34%
tgt	2	42%	0.00	0.00	50.20%
ttg	4	4%	1.81	1.84	6.28%
tgg	4	9%	1.33	1.32	12.87%
tgg'	4	33%	0.56	0.54	10.50%
ggg	2	0%	∞	2.06	0.96%
ggg'	4	0%	∞	1.93	1.20%
gg'g	2	0%	∞	1.98	0.12%
gtg	2	0%	∞	3.48	0.25%
gtg'	2	0%	∞	3.17	0.29%

Table 4.9: Results from the molecular dynamics simulation of liquid DME, using force field parameters fitted to energies calculated from the experimental populations.

Once again, the conformational populations obtained from simulation are very different to those from experiment. In this case, the *tgg'* population has actually reduced to about 11%.

4.4.5.6 Charge-Scaling Fits

Upon analysis of a complete component-by-component energy-breakdown of the *tgt* and *tgg'* energies, it was discovered that the single-most significant contributor to the overall force field energy of these two conformations is the 1,4 oxygen-oxygen

electrostatic repulsion. The possibility was considered that this large, unfavourable energy term was affecting the relative populations of these two conformations, and so several fits were performed with lower magnitude charges on atoms in the system.

In addition, it is widely believed that the 1,5 O-H interaction in DME is a hydrogen-bond. It was therefore also decided to scale the charges up as well as down, to find out how the balance between the O-O and O-H coulombic energies would affect the overall molecular dynamics populations. Many of the attempted

Charges scaled	ttt	tgt	ttg	tgg	tgg'
Unchanged OPLS-AA	10.30%	54.29%	3.85%	9.83%	18.88%
0% OPLS-AA	Split Minimum				
25% OPLS-AA	Split Minimum				
50% OPLS-AA	Split Minimum				
75% OPLS-AA (1)	Split Minimum				
75% OPLS-AA (2)	Vapourises				
85% OPLS-AA	15.43%	54.10%	4.92%	7.07%	16.66%
90% OPLS-AA	13.90%	53.81%	4.83%	8.15%	16.97%
110% OPLS-AA	12.51%	52.74%	4.28%	10.71%	16.82%
115% OPLS-AA	Split Minimum				
Oxygens, -10%	12.70%	54.63%	4.42%	8.32%	17.55%
Oxygens, +10%	Split Minimum				
Smith Hydrogen Charges	Split Minimum				

Table 4.10: Charge-scaling fits. Fits labeled *Oxygens* involved the scaling of charges on oxygens only (the excess charge was compensated for by sharing a neutralising "excess charge" equally among the four carbon atoms). Remaining fits had all charges scaled. The *Smith Hydrogen Charges* fit was performed using the higher hydrogen charges from Smith's DME force field. Again, the compensating charge was shared equally among the carbon atoms.

fits (shown in table 4.10) actually failed, giving more than one degenerate *ttt* conformation (labeled *Split Minimum*), usually with either the C-O-C-C or O-C-C-O dihedrals at around 160 degrees, rather than 180 degrees (figure 4.8). The reason for this is an unusually large, positive V4 value in the torsion potential, giving rise to a peak in energy at a dihedral of zero degrees (*trans*). Attempts that failed in this way included 0%, 25%, 50%, 75% and 115% overall charges, and a 10% increase on oxygen charges, as well as an attempt using Smith's higher hydrogen charge. A second, more successful fit using 75% overall charge resulted in a system that

vapourised in simulation at a constant pressure of 1 atm because of a reduction in intermolecular interactions. The remaining fits that did give viable force fields still show no significant improvement in the *tgg'* population.

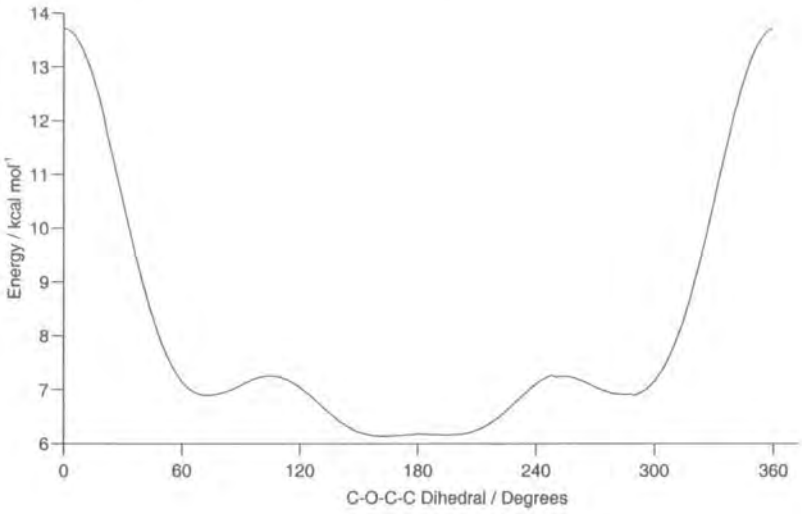

Figure 4.8: Dihedral driver results using a force field that produces a doubly degenerate *trans* conformation in the C-O-C-C dihedral, because of a small energy barrier centred at 180 degrees. This could result in a four-fold degenerate *ttt* conformation in DME as there are two such dihedrals present. Energies calculated at two degree intervals (points omitted for clarity).

4.4.5.7 Torsion-Elimination Fits

Attempts were made to incorporate the entire torsional energy contribution about the major dihedrals into the two sets of fitted torsional parameters by elimination of all other torsion potentials acting about the C-C and O-C atom pairs. The reasoning behind this was that in fitting C-O-C-C and O-C-C-O torsion functions, other related torsions such as H-C-O-C and H-C-C-H were unaffected, and still contributed energy in accordance with the original OPLS-AA force field. It was hoped that the entire torsional potential for the two major dihedrals could be incorporated into only two parameter sets. The results of these attempts are summarised in table 4.11.

In the case of the elimination of both HCCH and HCCO torsion terms, the *tgg'* population sees a slight improvement, coming to 19.6%. However, this figure is still unsatisfactory. Once again, some of the fits (elimination of HCOC, HCCO and all torsions) resulted in non-viable force fields with degenerate *ttt* conformations.

	ttt	tgt	ttg	tgg	tgg'
HCOC eliminated	Split Minimum				
HCCH eliminated	15.71%	48.77%	6.33%	9.22%	16.87%
HCCO eliminated	Split Minimum				
HCCH & HCCO eliminated	8.89%	49.13%	3.87%	12.94%	19.63%
All torsions eliminated	Split Minimum				

Table 4.11: Torsion-elimination fits.

4.4.5.8 Increasing the Energy of the *tgt* Conformation

In an attempt to reduce the population of the *tgt* conformation in the molecular dynamics simulation of DME, the energy of this conformation was increased by 1 kcal mol^{-1} ($\approx$ 36%) relative to the *ttt* conformation. A very good fit was obtained with this altered energy, and a molecular dynamics simulation was performed.

Conformation	Force Field	Raman
ttt	13.79	12%
tgt	57.52	42%
ttg	3.63	4%
tgg	8.07	9%
tgg'	15.27	33%
ggg	0.39	~ 0
ggg'	1.01	~ 0
gg'g	0.10	~ 0
gtg	0.11	~ 0
gtg'	0.11	~ 0

Table 4.12: Conformational populations for DME from a molecular dynamics simulation using the torsional parameters obtained from a fit using an increased *tgt* energy. All other force field parameters used are from the OPLS-AA force field.

Despite increasing the energy of the *tgt* conformation in the fit, the population of this conformation has slightly increased at the expense of the already low *tgg'* population.

4.4.5.9 Exchanging the Energies of the *tgt* and *tgg'* Conformations

After the failure of increasing the *tgt* energy, the energies of this and the *tgg'* conformation were swapped in an attempt to bring the molecular dynamics populations into line with experiment. Table 4.13 shows the population of each conformation obtained in a molecular dynamics simulation using this force field.

	Molecular Dynamics Step Number						
Conformation	50,000-190,000	190,000-330,000	330,000-470,000	470,000-610,000	610,000-750,000	50,000-750,000	Raman
ttt	13.82%	12.72%	13.30%	12.79%	12.72%	13.07%	12%
tgt	53.37%	55.14%	54.37%	55.51%	54.33%	54.54%	42%
ttg	4.17%	4.08%	4.04%	4.02%	3.68%	4.00%	4%
tgg	8.51%	8.12%	8.50%	8.27%	8.49%	8.38%	9%
tgg'	17.95%	17.88%	17.74%	17.54%	18.48%	17.92%	33%
ggg	0.37%	0.38%	0.29%	0.32%	0.48%	0.37%	~ 0
ggg'	1.37%	1.35%	1.33%	1.16%	1.44%	1.33%	~ 0
gg'g	0.12%	0.08%	0.11%	0.08%	0.09%	0.10%	~ 0
gtg	0.15%	0.11%	0.12%	0.16%	0.16%	0.14%	~ 0
gtg'	0.17%	0.15%	0.21%	0.15%	0.12%	0.16%	~ 0

Table 4.13: Populations of DME's conformations from a molecular dynamics simulation using the torsional parameters from table . All other force field parameters used are from the OPLS-AA force field.

Once again, the *tgg'* population is severely underpopulated, but excellent agreement is obtained for the *ttg* and *tgg* conformations.

4.4.5.10 Decreasing the Energy of the *tgg'* Conformation

As a complementary test to the previous ones, attempts were made to increase the population of the *tgg'* conformation in the liquid phase by decreasing the energy (thereby increasing the conformation's accessibility). This was attempted by setting the *tgg'* energy lower than the *ttt* energy, in the hope that the deepened potential well around the *tgg'* conformation would grant more accessibility.

Table 4.14 shows the results of this test. This force field shows very good agree-

Conformation	Rel. Energy / kcal mol^{-1}	Force Field Population	Raman
ttt	0.459	13.55%	12%
tgt	0.657	46.55%	42%
ttg	1.969	2.93%	4%
tgg	2.330	4.27%	9%
tgg'	0.000	30.82%	33%
ggg	3.195	0.40%	~ 0
ggg'	1.498	1.05%	~ 0
gg'g	*	0.00%	~ 0
gtg	3.296	0.22%	~ 0
gtg'	3.094	0.21%	~ 0
Trans C-O-C-C		79.11%	77%
Gauche C-O-C-C		20.89%	23%
Trans O-C-C-O		16.91%	16%
Gauche O-C-C-O		83.09%	84%

Table 4.14: Conformational energies and populations from MD simulations of DME using the best force field so far.
* This conformation does not minimise

ment with experimental populations, particularly for the troublesome *tgg'* conformation. The populations of the *ttg* and *tgg* conformations are a little low, but certainly closer to the Raman populations than *tgg'* was in previous attempts.

Table 4.15 shows results from gas phase Monte Carlo calculations using standard OPLS-AA and the best force field obtained through fitting, compared to the two experimental studies. It is immediately obvious that the *tgg'* conformation is much more accessible in this fitted force field, as the MC population has increased to 39% (from 16% in OPLS-AA).

As pointed out by Inomata and Abe,[132] the agreement between their NMR study and Astrup's diffraction[129] analysis is good for the t/g ratio in the O-C-C-O dihedral, if not for the individual conformations themselves. The agreement in the C-O-C-C dihedral is moderate. As far as the overall t/g population ratios go, the best agreement is seen between the NMR study and the MC calculation using the best force field, but again, there is little agreement between the more highly populated individual conformations.

From these results, an oxygen *gauche effect* is obvious; although the C-O-C-C t/g populations remain roughly constant when going from the gas to the liquid phase,

Conformation	Diffraction	NMR	OPLS-AA	Best Force Field
TTT	13%	12%	38.81%	25.92%
TGT	23%	46%	31.64%	30.03%
TTG	3%	9%	7.71%	2.88%
TGG (tgg + tgg')	53%	27%	20.13%	40.13%
GGG (ggg + ggg' + gg'g)	3%	4%	1.28%	0.91%
GTG (gtg + gtg')	5%	2%	0.43%	0.13%
Trans C-O-C-C	64%	76%	84.37%	77.46%
Gauche C-O-C-C	36%	24%	15.63%	22.54%
Trans O-C-C-O	21%	23%	46.95%	28.93%
Gauche O-C-C-O	79%	77%	53.05%	71.07%

Table 4.15: Gas phase populations from electron diffraction,[129] gas phase NMR,[132] MC with standard OPLS-AA force field, and MC with force field fitted to lowered *tgg'* energy.

the O-C-C-O t/g ratio decreases significantly, from 23/73 to 16/84. The *gauche effect* is also assisted by the low energy of the O-C-C-O *gauche* state ($\Delta E_{tgt-ttt} \approx$ 0.3 kcal mol^{-1}) compared to the C-O-C-C *gauche* state ($\Delta E_{ttg-ttt} \approx 1.6$ kcal mol^{-1}), seen in figure 4.2.

Optimisations of hexane (table 4.16) at the MP2/6-31G++'(d,p) level show that the *ttg* and *tgt* conformations are very close in energy, at 0.6 kcal mol^{-1}, confirming that the oxygens present in DME are having a significant effect. Hexane's *tgg'* conformation is unusually high in energy (2.9 kcal mol^{-1}) compared its *tgg* energy (0.9 kcal mol^{-1}). This is due to a close contact between two hydrogen atoms (one on the 1-methyl group and the other in the 5-methylene group), a situation that does not occur in DME due to the absence of the 5-methylene group. The third dihedral (g^-) in hexane has a larger angle than the corresponding DME dihedral because of this extra strain.

4.5 Detailed Study of Potential Energy Surface

Despite varying a number of different factors in the fits (most significantly the relative energies of the *tgt* and *tgg'* conformations) the relative populations were not significantly affected, except in the very last fit. In order to better visualise the potential energy surface, a Ramachandran map was plotted using the original OPLS-AA

	DME				Hexane			
	Energy	Dih 1	Dih 2	Dih 3	Energy	Dih 1	Dih 2	Dih 3
ttt	0.00	179.4	179.6	179.7	0.00	179.9	-179.8	180.0
tgt	0.28	-174.4	75.0	-174.6	0.58	175.3	63.6	175.4
ttg	1.60	-178.9	177.6	81.0	0.60	179.6	175.4	63.6
tgg	1.88	-178.9	60.4	63.4	0.91	174.9	59.0	58.5
tgg'	0.42	-178.5	74.0	-84.1	2.87	175.0	60.8	-94.1
ggg	1.80	58.9	44.3	59.0	1.25	59.1	56.4	59.1
ggg'	2.21	76.8	70.9	-80.8	3.29	62.4	62.8	-92.6
gg'g	2.57	103.3	-63.7	102.6	5.28	90.8	-61.9	90.9
gtg	3.33	84.9	179.1	84.9	1.18	63.5	171.4	63.5
gtg'	3.22	80.3	-179.7	-79.9	1.37	64.8	179.9	-65.1
tct	9.30	180.0	0.0	180.0	5.77	179.9	0.0	179.8
ttc	7.78	-179.9	-179.7	0.0	5.84	179.9	-179.8	0.0

Table 4.16: Comparison of optimised structures of the ten conformations of DME and hexane at the MP2/6-31G++'(d,p) level of theory. Dih 1, Dih 2 and Dih 3 are the angles of the three major dihedrals along the molecular backbone. Energies are in kcal mol $^{-1}$ and dihedral angles are in degrees.

force field (figure 4.9), by varying the O-C-C-O and C-C-O-C dihedrals together, while maintaining the remaining C-O-C-C dihedral in the *trans* state. This map would then encompass all five key, low-energy conformations, and the surrounding PES environment.

There are three features immediately noticeable about the *tgg'* sectors on this PES map. First, and most significantly, the *tgg'* potential well is noticeably narrower than the *tgt* well, as noted by Smith.[49] This narrow potential well explains why the population of the *tgg'* conformation did not increase significantly, even when the potential well was made slightly deeper (i.e. when the energy of the minimum was reduced). The depth of the potential has less effect on the accessibility of those states than the width. Only a drastic energy reduction for *tgg'* results in an increased amount of accessible phase space for this conformation.

Second, the large *tgc* energy barrier that lies between the *tgg'* and *tgg* conformations appears to polarise the entire *tgg'* sector towards the *tgt* region. Most notably, the *tgt-tgg'* barrier is pushed well into the *tgt* regime. As a result, a particular conformation that may lie on the *tgg'* side of this barrier, and therefore be *tgg'* in spirit, could actually be counted as *tgt*, because is has a C-C-O-C dihedral angle less

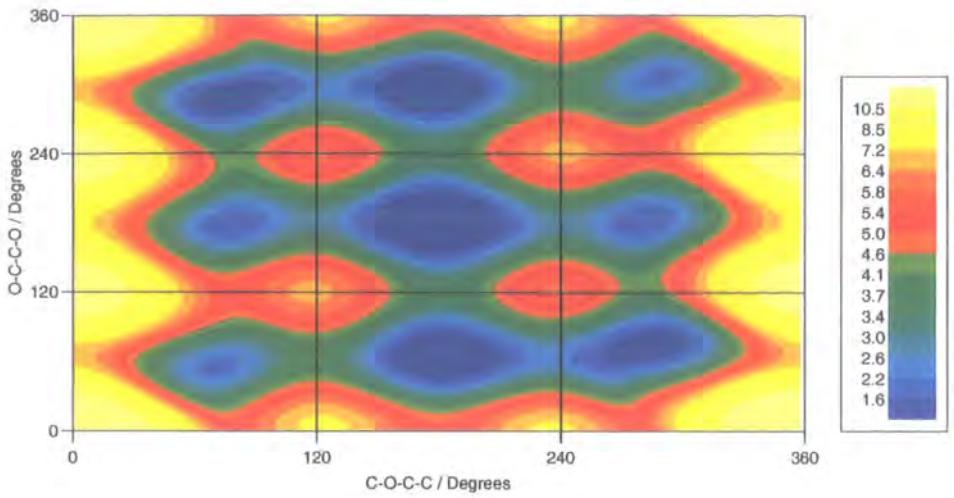

Figure 4.9: Ramachandran map based upon the O-C-C-O and C-C-O-C dihedrals in DME, using the OPLS-AA force field. The remaining C-O-C-C dihedral is trans. All energies are relative to *ttt* and are in kcal mol $^{-1}$. All five low energy conformations are shown: *tgg'* (top left and bottom right), *tgt* (top centre and bottom centre), *tgg* (top right and bottom left), *ttg* (centre left and centre right) and *ttt* (centre).

than 240^o.

Finally, there are two low energy barriers (*tgg'*-*tgt* and *tgg'*-*ttg*) which the DME molecules could easily overcome, resulting in a depletion of the *tgg'* population, although it has already been determined that the heights of these barriers have very little effect on the conformational populations.

In an attempt to understand the impact of the second effect, a population analysis was performed on a previous MD trajectory obtained with the original OPLS-AA force field, with modified boundaries for conformational definitions. Rather than assigning g^-, t and g^+ to dihedral angles $0 - 120^o$, $120 - 240^o$ and $240 - 360^o$ respectively, a visual inspection of figure 4.9 yielded modified boundaries; g^-, t and g^+ are assigned for the C-O-C-C dihedral in the ranges $0 - 125^o$, $125 - 235^o$ and $235 - 360^o$ respectively, and $0 - 130^o$, $130 - 230^o$ and $230 - 360^o$ respectively for the O-C-C-O dihedral. These new ranges coincide with the *tgt*-*tgg'* and *tgt*-*ttg* energy barrier maxima, and ensure that all molecules that lie on the *tgg'* side of this barrier are counted as such.

As the results in table 4.17 show, this modification has very little effect. The *ttt* population has reduced because its sector in phase space has been reduced in

Conformation	MD Population	Raman Population
ttt	13.38%	12%
tgt	49.92%	42%
ttg	5.20%	4%
tgg	13.10%	9%
tgg'	14.89%	33%
ggg	1.41%	~ 0
ggg'	1.44%	~ 0
gg'g	0.17%	~ 0
gtg	0.26%	~ 0
gtg'	0.23%	~ 0

Table 4.17: Populations of DME's conformations from a molecular dynamics simulation using the OPLS-AA force field, and modified conformational definitions.

volume. A population increase is seen in the *ttg* conformation despite reduction in the volume of phase space associated with this conformation, because the reduction in the O-C-C-O range removes higher energy geometries while the smaller increase in the C-O-C-C range introduces new lower-energy phase space. The *tgt* population has reduced slightly, while the *tgg'* population has increased.

A Ramachandran Map was also plotted for Smith's force field, but because it appears very similar the the OPLS-AA one, it is not shown here.

In order to investigate the best force field found so far, however, a Ramachandran map was plotted for this force field, in figure 4.10. With this force field, the *tgg'* energy well has widened significantly, and the *tgt-tgg'* barrier is now biased towards the *tgg'* conformation, increasing the accessibility of this conformation as expected. There is now, however, a more significant biasing of the *tgg'-ttg* barrier towards the *ttg* sector, but this does not seem to cause any problems in simulation. Energy wells for the *ttg* and *tgg* conformations have not been significantly affected, so their populations in simulation remain in reasonably good agreement with experiment.

This force field also has a large, positive V_4 term in the O-C-C-O torsion potential,

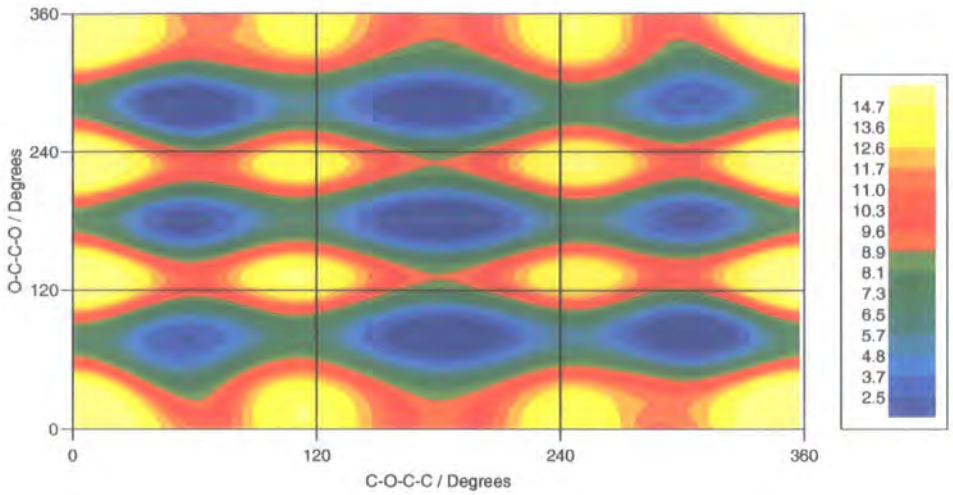

Figure 4.10: Ramachandran map based upon the O-C-C-O and C-C-O-C dihedrals in DME, using the best force field parameters found in reproducing the *tgg'* population. The remaining C-O-C-C dihedral is trans. All energies are relative to *ttt* and are in kcal mol^{-1}. Sector/conformational assignments are as in figure 4.9.
The torsion parameters used were as follows:
C-O-C-C: -1.5627, 2.2732, 3.0641, -1.2669
O-C-C-O: 0.7445, -2.9173, 2.7935, 4.4899

which does not result in the split minimum problem encountered earlier. It is likely that this strong torsion potential is a major contributor to the widening of the *tgg'* potential well.

4.5.1 Reverse-Engineering the OPLS-AA Force Field

It is expected that the population of the *tgg'* conformation in MD and MC methods will increase if the force field used presents a significantly wider *tgg'* potential well. An attempt was made to widen this potential well, through detailed analysis of the interaction-by-interaction breakdown of the force field energy for the *tgg'* conformation.

On minimisation of the *tgg'* conformation, it was found that the 4,5-C-O bond and 4,5,6-C-O-C angle had the largest contributions to the stretching and bending energies respectively, being the most highly strained. These are therefore two interactions (among others) that are responsible for the narrow nature of the surrounding potential well.

The force constants associated with these two interactions were halved, and the

fitting procedure repeated to obtain another trial force field. Unfortunately on testing with MD, the *tgg'* population is unaffected and the *ttt* population has increased at the expense of the *tgt* and *tgg* conformations. It was discovered afterward that this was probably due to these two interactions also being significant contributors to the *ttt* force field energy as well. The *tgg'* energy well may have been widened, but the *ttt* well was also opened up, nullifying the improvement and disrupting the balance between the various conformations.

	ttt	tgt	ttg	tgg	tgg'
C-C	0.0018	0.0052	0.0138	0.0264	0.0239
C-H	0.0031	0.0024	0.0016	0.0013	0.0021
C-O	0.0844	0.0864	0.1151	0.1166	0.1338
C-C-H	0.032	0.038	0.059	0.063	0.108
H-C-H	0.016	0.020	0.039	0.052	0.056
C-C-O	0.004	0.000	0.082	0.196	0.217
O-C-H	0.152	0.152	0.241	0.230	0.332
C-O-C	0.336	0.378	0.560	0.657	0.663
O-C-C-H	0.000	0.018	0.008	0.042	0.205
H-C-C-H	0.002	0.010	0.002	0.018	0.083
C-O-C-H	0.000	0.020	0.315	0.132	0.281
O-C-C-O	0.000	-0.395	0.000	-0.439	-0.344
C-C-O-C	0.000	0.006	0.312	0.262	0.286

Table 4.18: Interaction-by-interaction breakdown of the bonded force field energies associated with each of the five low-energy conformations in the OPLS-AA force field. All energies are in kcal mol $^{-1}$.

Perhaps a better way to go about this would be to locate a force field component in the *tgg'* optimisation that is of significant energy, and that also contributes very little energy to the other conformations. Such reverse-engineering could very well yield a force field with a much improved liquid-phase representation of DME. Table 4.18 shows the bonded contributions to the force field energy for each of the five lowest energy conformations. It is generally the case that the *tgg'* conformation has one of the highest, if not *the* highest energy for each contribution. This observation is in agreement with the idea of a narrow potential well. Out of all of these components, however, only the O-C-C-H and H-C-C-H torsions appear to have a significantly higher energy in *tgg'* than any other conformation. When these

parameters are altered, as in table 4.11, a slight improvement is seen in the *tgg'* population. Perhaps reduction of other parameters in this way may widen the *tgg'* potential well somewhat, without compromising agreement between fitted force field and *ab initio* energies.

4.6 Conclusions

It is clear that current force fields such as that of Smith, and the widely used OPLS-AA are not suitable for simulation of liquid- and gas-phase DME where good conformational agreement with experiment is required. The narrow potential well of the *tgg'* conformation is responsible for the low population of this conformation predicted using computational methods. A more detailed study of the various interactions at play in these force fields, and some intensive reverse-engineering work, could produce a force field that better predicts the behaviour of the DME molecule without resorting to a force field with unusually high V_4 terms in the fitted torsion potential.

In addition, currently accessible *ab initio* calculations do not give a reliable enough set of conformational energies for this molecule, even up to the MP2 method with the 6-31G family of basis sets. With more computer time and memory, higher methods (MP3, MP4, Coupled Cluster) and better basis sets (cc-pVDZ, aug-cc-pVTZ, etc) it is possible that convergence will be found, and the conformational energies of this molecule can be predicted with reasonable confidence and accuracy.

Unfortunately, this phase of the study took much longer than expected, due to repeated failures in attempts to improve the fit quality and conformational populations in the liquid phase. As a result, a force field had to be selected for the amphiphilic polymer simulations before this section of the work was complete. The fitted force field chosen (Amphiphile force field) is the one that gave the best agreement with experiment in conformational populations prior to the study on widening the *tgg'* energy well (Engineered force field). This chosen force field gives very similar populations to the one detailed in table 4.8. The torsion parameters and MD liquid phase populations for this force field are compared with those of the OPLS-AA and

Engineered force fields in table 4.19.

	V_1	V_2	V_3	V_4
C-O-C-C (O)	0.6500	-0.2500	0.6700	0.0000
O-C-C-O (O)	-0.5500	0.0000	0.0000	0.0000
C-O-C-C (A)	1.6678	-0.5653	-0.0033	-0.2931
O-C-C-O (A)	2.8198	-2.5606	0.8216	-0.9203
C-O-C-C (E)	-1.5627	2.2732	3.0641	-1.2669
O-C-C-O (E)	0.7445	-2.9173	2.7935	4.4899

Conformation	Population (O)	Population (A)	Population (E)
ttt	13.54%	15.35%	13.55%
tgt	50.31%	51.01%	46.55%
ttg	5.16%	5.19%	2.93%
tgg	13.01%	7.54%	4.27%
tgg'	14.60%	18.43%	30.82%
ggg	1.39%	0.36%	0.40%
ggg'	1.39%	1.32%	1.05%
gg'g	0.13%	0.34%	0.00%
gtg	0.25%	0.22%	0.22%
gtg'	0.22%	0.24%	0.21%

Table 4.19: Torsion parameters and conformational populations from MD simulations of bulk liquid DME for the O(PLS-AA), A(mphiphile) and E(ngineered) force fields.

All other parameters in the Amphiphile and Engineered force fields are from the OPLS-AA force field. No further modifications have been made.

Chapter 5

Amphiphilic Polymer Simulations

5.1 Introduction

Molecular simulation is becoming a useful tool in the study of amphiphilic materials in solution or at interfaces. For example, the associations between molecules of *t*-butyl alcohol and urea have been looked at using MD[156] at the atomistic level. The free energy of adsorption as well as conformational and orientational properties of *p*-*n*-pentylphenol at the water-air interface have also been studied using simulation methods.[157] Phase transitions have been observed in a system of amphiphilic chains at the water-air interface (at various surface concentrations) in a computational study.[158] Monolayers of amphiphilic material can also be analysed using coarse-grained simulation techniques.[159] Coarse-graining has also be applied to amphiphiles at the water-oil interface.[160]

Coarse-grained simulations have proven popular in the study of the behaviour of polymer chains. One particular study of polymer chains tethered to a water interface (performed with external potentials representing both the water and other neighbouring chains)[161] has been employed previously to study the "pancake" to "brush" transition that occurs as surface concentration increases. However, it is often very useful to have a simulation technique which can accurately reproduce experimental observations. Such simulations can be adjusted easily to simulate a whole range of related systems. This is particularly beneficial where there is a great deal of synthesis and characterisation required in preparing the corresponding real-

world experiment. Also, simulation methods are more freely available than, say, a coherent neutron source, required to gather neutron reflectometry data. In order to test the capabilities of computational methods in reproducing such experimentally observed effects, a particular system that has previously been studied in depth experimentally[31,32] has been selected for analysis in simulation. This system has previously been subject to greatly simplified and idealised simulation techniques,[161] which gave encouraging, although moderate agreement with experiment. It was concluded in these earlier simulations that the main reason for the lack of excellent agreement with experiment was due to deficiencies in the model employed there, where a single molecule was placed in a potential well with hard walls representing surrounding molecules. The aim of this work is to determine whether more detailed, fully atomistic simulations, with all molecules explicitly represented can reproduce the experimental data more successfully.

This chapter is concerned with atomistic MD simulations of an amphiphilic polymer at a water-air interface, at a range of surface concentrations. These simulations will be used to generate neutron reflectivity profiles which can be compared to experimental results. Some structural analysis (radii of gyration and conformational properties) will also be carried out.

Before results are discussed, however, a brief introduction to the optical matrix method is given. This method is used to calculate a neutron reflectivity profile for a simulated system, from the densities and scattering lengths of the three components (water, polynorbornene and PEO).

5.2 Optical Matrix Method

The optical matrix method can be used to generate neutron reflectivity profiles for the experimental setup shown in figure 5.1. By breaking a system down into a series of slabs along the z-axis, and making the approximation that the composition (and therefore scattering length density) is constant throughout each slab (but varying between them as composition changes), it is possible to simulate a neutron reflectivity profile. This approximation becomes more realistic as the thickness of the

slabs approaches zero, however there should be no significant problems if the slab thickness is sufficiently small that the scattering length density does not vary too drastically between consecutive slabs.

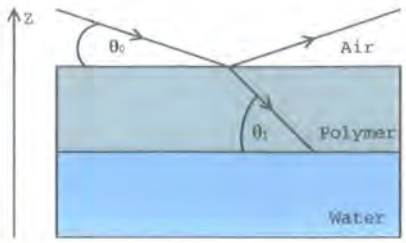

Figure 5.1: Neutron reflection in a simple, three-layer model.

In a simple three-slab system (say, air, polymer layer and water, shown in figure 5.1), the reflectivity, R, due to the central slab (amphiphile) can be written as

$$R = \left| \frac{r_{01} + r_{12} \exp(2i\beta_1)}{1 + r_{01} r_{12} \exp(2i\beta_1)} \right|^2, \tag{5.1}$$

where r_{ij} is a Fresnel coefficient, and β_1 is the phase shift of the neutron beam in the polymer layer.

The Fresnel coefficients characterise the optical properties of an interface between two consecutive slabs (i and j=i+1), in terms of their refractive indices as shown in equation 5.2,

$$r_{ij} = \frac{n_i \sin\theta_i - n_j \sin\theta_j}{n_i \sin\theta_i + n_j \sin\theta_j}, \tag{5.2}$$

where n_i is the refractive index of layer i, and θ_i is the angle of incidence of the neutron beam at the *i/(i+1)* boundary (air-polymer or polymer-water), after refraction at any previous interfaces.

The phase shift of the neutron beam is also readily calculated from equation 5.3

$$\beta_i = \left(\frac{2\pi d}{\lambda} \right) \sin\theta_i, \tag{5.3}$$

where d is the thickness of the polymer layer, and λ is the wavelength of the incident beam.

This calculation is quite simple for one polymer layer but, when extended to

include additional slabs, the equations become very complex. It has previously been shown[162] that the composition and properties of each layer, i, can be written as a characteristic matrix, M_i, as shown in equation 5.4

$$M_i = \begin{bmatrix} \cos\beta_j & -\frac{i}{\kappa}\sin\beta_j \\ -i\kappa\sin\beta_i & \cos\beta_j \end{bmatrix}, \tag{5.4}$$

where $\kappa = n_i \sin\theta_i$.

These characteristic matrices are easily multiplied together to give an overall matrix characterising the reflective properties of the entire array of slabs. This resultant matrix is shown in equation 5.5,

$$M_1 M_2 ... M_n = M = \begin{bmatrix} M_{11} & M_{12} \\ M_{21} & M_{22} \end{bmatrix}, \tag{5.5}$$

where M_{ij} are the values of the individual elements in the matrix.

The overall reflectivity of the system can then be written in terms of the elements of this matrix, in a fashion analogous to equation 5.1. Equation 5.6 shows the reflectivity in terms of these matrix elements,

$$R = \left| \frac{(M_{11} + M_{12}\kappa_s)\kappa_a - (M_{21} + M_{22})\kappa_s}{(M_{11} + M_{12}\kappa_s)\kappa_a + (M_{21} + M_{22})\kappa_s} \right|, \tag{5.6}$$

where a and s refer to the upper phase (air) and lower phase (bulk water) respectively.

The optical matrix method can be adapted to account for the natural roughness of the various interfaces involved,[163,164] to represent the system more realistically.

Since number density (and therefore scattering length density) is readily calculated from computer simulation, and due to the fact that simulations can be easily broken down into slab sequences, the optical matrix method is ideal for generating reflectivity profiles from simulation trajectories to compare to experiment.

5.3 Method

Molecular dynamics simulations were performed on an amphiphilic polynorbornene-*g*-poly(ethylene oxide) graft copolymer at an air-water interface. These simulations involved considerable difficulty in the setup procedure. The construction of these more complex systems are outlined in the following sections. All MD simulations were carried out using the DL_POLY[125] molecular simulation package.

Neutron reflectometry results are obtained from the density profiles calculated from the simulation trajectories. In order to do this, the optical matrix method was used (section 5.2).

5.3.1 Setting Up a Water-Air Interface

It quickly became apparent upon measurement of the lengths of the fully extended PEO sidechains in the graft copolymer that the previously established slab of water (chapter 3) was too narrow; the chains in their fully extended conformation passed right through the slab and extend out of the lower interface, back into an air environment. The best remedy was to increase the thickness of the water layer. In order to do this, the final configuration of the smaller (216 molecules) charge-group simulation of TIP4P water was taken, and enlarged through replication (multiplication factors 2, 2 and 3 in the x, y and z directions respectively). The z-length of the box was increased to 100 Å to allow the formation of water interfaces, and the x and y box lengths were increased slightly from about 37.79 Å to exactly 38 Å for convenience. This new system contained 2592 TIP4P water molecules, and was subject to further molecular dynamics simulation for three reasons: to allow the water-air interfaces to form, to remove the 0.21 Å thick region of vacuum that had been formed as a result of rounding up the x and y lengths of the simulation box and to remove the correlation of atomic positions introduced upon replicating the original system. 500,000 steps of simulation were performed (first 50,000 were equilibration), using a 2 fs time-step. A 7 Å cutoff was used along with charge-group based handling of the electrostatic interactions. The NVT ensemble was employed (using a Hoover thermostat) to ensure that the box-size remained as initially set up.

Once this equilibration was completed, the final configuration of the simulation was again expanded. This time, the x and y lengths of the box were doubled (again through replication of molecules), and the z length was further increased to allow sufficient distance between the two interfaces to prevent their interaction. The final system of TIP4P water was comprised of a slab of 10,368 molecules, centred in the z-direction in an orthorhombic box of 76 Å by 76 Å by 200 Å.

Establishing a good starting configuration for the water component was quite trivial. The challenge was to set up the polymer molecules and place them at this interface; this proved to be a more complex task.

5.3.2 Initial Attempts at Placing the Amphiphilic Polymer Molecules at the Water-Air Interface

A number of approaches were tried in setting up a reasonable starting configuration for the main simulations. These are outlined in the order they were attempted in the following subsections. These early attempts used a significantly narrower water slab. The revised water slab described in section 5.3.1 was only used for the final set of simulations detailed in section 5.3.3, when the depth of a typical brush structure for this system was known.

5.3.2.1 Placing a Fully Extended Polymer Molecule at the Interface

A single, extended polymer molecule was placed at the interface and simulated. Figure 5.2 shows the starting configuration used; the polymer molecule is placed just above the water interface.

By the end of the simulation (figure 5.3), the polymer molecule had aligned itself well with the interface, and one of the PEO chains had begun to find its way into the bulk water. Unfortunately, only one polymer molecule can be introduced in this fashion; as figure 5.2 (top view) shows, the single polymer molecule is already in a very extended conformation and prevents any packing of further molecules into the simulation box. In order to introduce more than one molecule into the water system, a different approach is required.

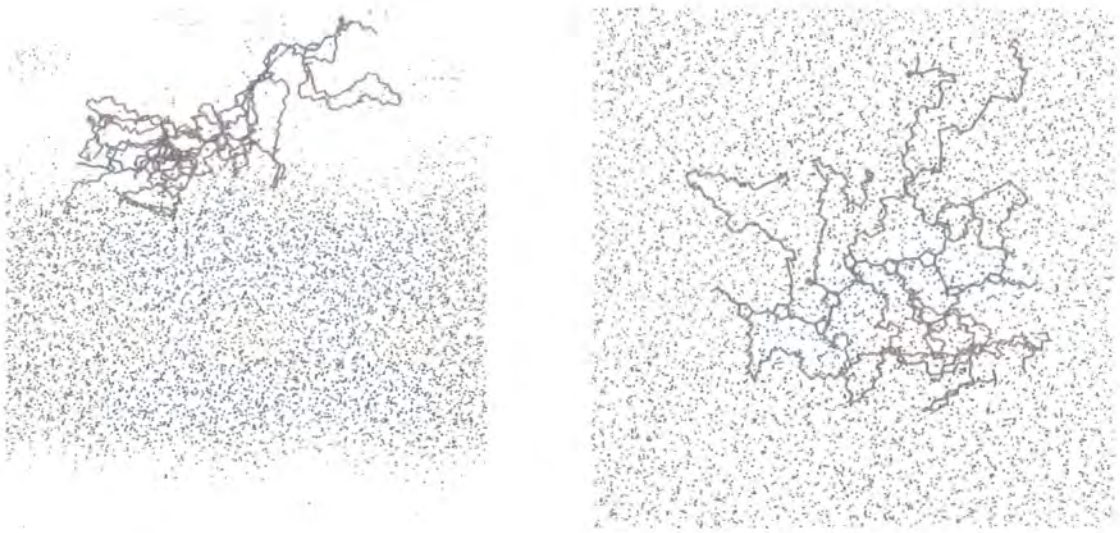

Figure 5.2: Side-view and top-view of a single amphiphilic polymer molecule at the air water interface. This snapshot was taken from the beginning of the MD simulation. The hydrophobic backbone is shown in blue, the hydrophilic sidechains are shown in red and the water molecules are shown in black.

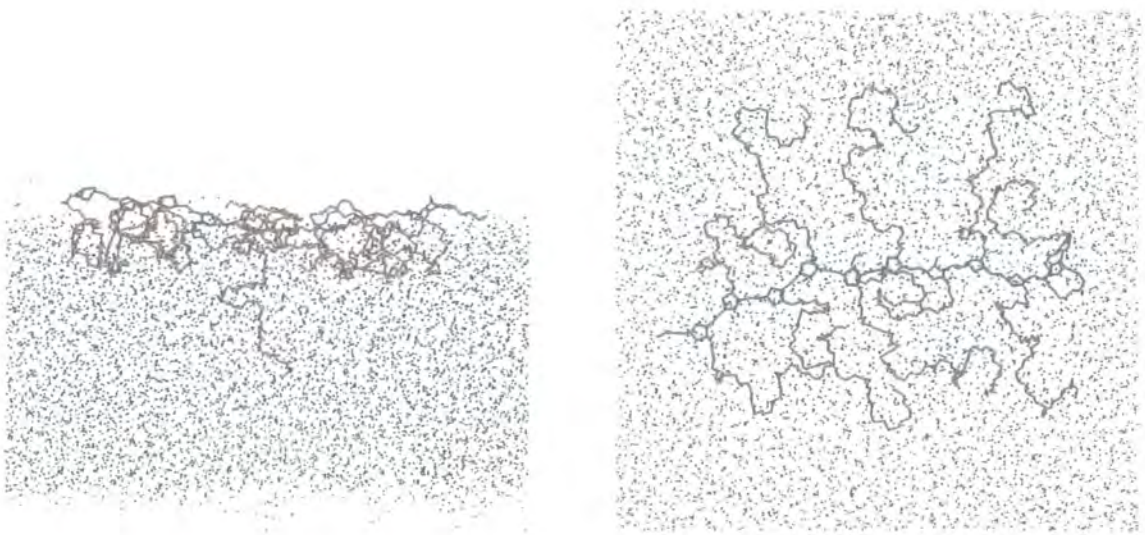

Figure 5.3: Side-view and top-view of a single amphiphilic polymer molecule at the air water interface. This snapshot was taken from the end of the MD simulation, after 3 ns. Colours as in figure 5.2.

5.3.2.2 Placing a Compressed "Blob" of Polymer Molecules at the Interface

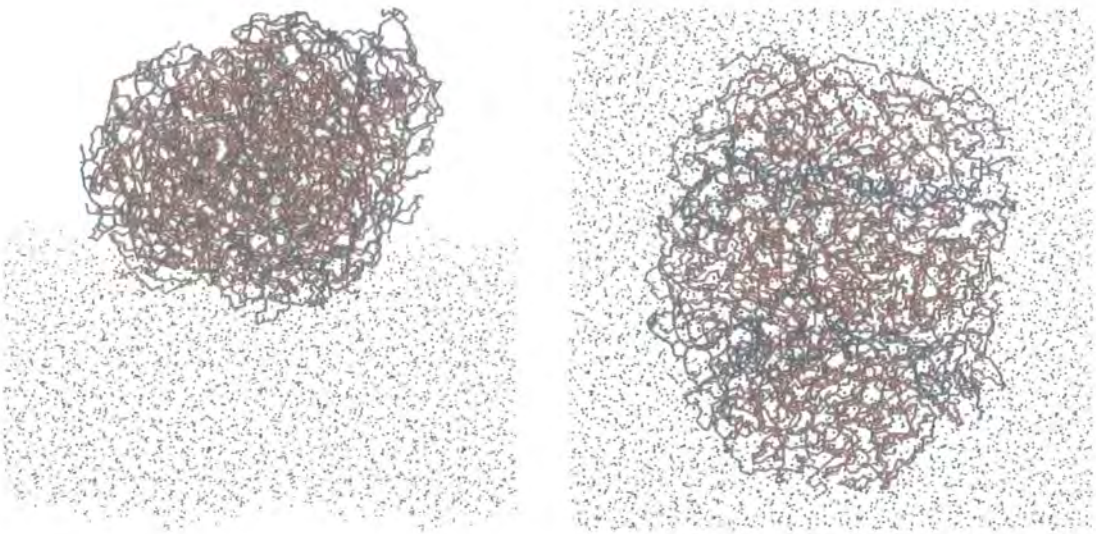

Figure 5.4: Side-view and top-view of eight amphiphilic polymer molecules aggregated at the air water interface. This snapshot was taken from the beginning of the MD simulation. Colours as in figure 5.2. The top view indicates that microphase separation may have taken place, as a lamellar structure has formed.

In an attempt to introduce more than one polymer molecule to the water interface, a new approach was considered; if the polymer molecules could be compressed, or aggregated, then it may be easier to introduce more molecules simultaneously. The first attempt at setting up the required system involved running a brief MD simulation (500,000 steps of 2 fs, 7 Å charge-group based cutoff) of eight amphiphilic polymer molecules, in close proximity to one another, in the gas phase. The aim was to encourage the molecules to aggregate and curl up to form a single entity that could easily be placed at the water-air interface. This simulation produced an ellipsoidal aggregate of polymer molecules which was then placed in close proximity to the water interface (figure 5.4). It is notable that there appears to be some microphase separation apparent in the top-view snapshot; a lamellar structure appears to have formed, separating regions of backbone from regions of sidechain.

It was hoped that with further simulation of this system, the PEO sidechains would eventually find their way down into the bulk water, aided by the steric crowding within the ellipsoid. Unfortunately, this proved unsuccessful, and despite spread-

ing at the interface, after a considerable amount of time spent in simulation only one or two (of eighty) PEO chains had begun to enter the bulk water (figure 5.5). In addition, the polymer backbone remained severely buckled and at many points, quite a distance from the interface. To carry on this simulation would have proved too computationally expensive, so other attempts were made to provide easier paths towards equilibration.

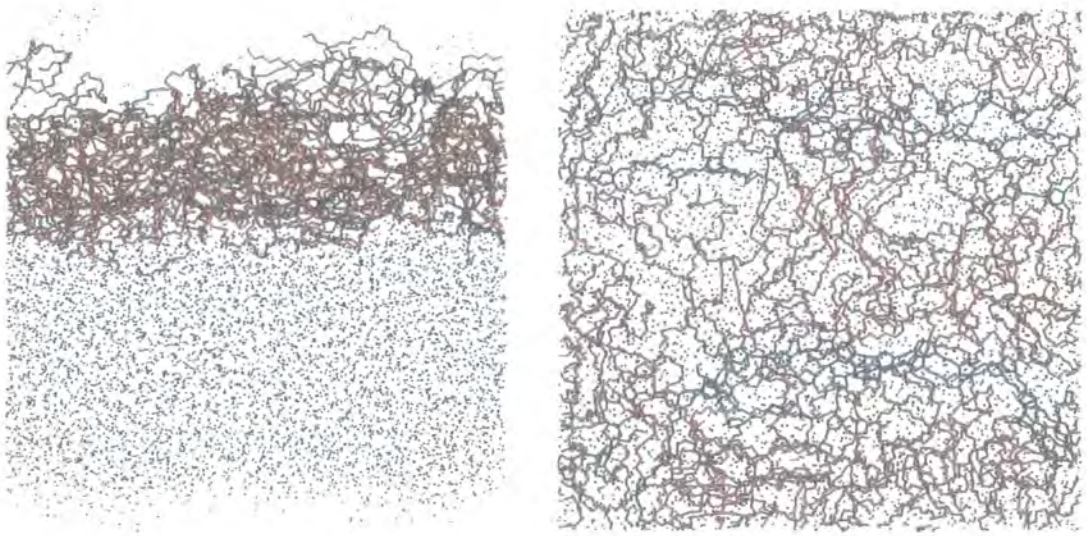

Figure 5.5: Side-view and top-view of eight amphiphilic polymer molecules at the air water interface. This snapshot was taken during the MD simulation, after spreading had occurred. The snapshot was taken at 260 ps, and colours as in figure 5.2.

5.3.2.3 Reducing Polymer-Polymer Interactions

A second approach to including more molecules at the interface was attempted. Here the magnitudes of all polymer-polymer interactions were significantly reduced. This approach was inspired by recent parallel-tempering work[165] in which potential softening was employed to speed up the equilibration process. The polymer-water and water-water interactions were unchanged. To accomplish this, all ε values for polymer-polymer interactions were reduced to 10 % of their OPLS-AA normal values. The idea behind this was to reduce the polymer-polymer attractions, effectively improving the quality (good/bad) of water as a solvent for this polymer. The end point of the previous attempt was used as the starting configuration for this simulation.

It is found to be the case that water indeed becomes a better solvent in this simulation; the polymer molecules absorb the water like a sponge, and swell accordingly (figure 5.6). Unfortunately the hydrophobic backbone is distributed randomly throughout the polymer/water layer and a significant period of equilibration would be required to allow the polymer molecules to rearrange themselves such that the hydrophobic backbones all leave the water layer.

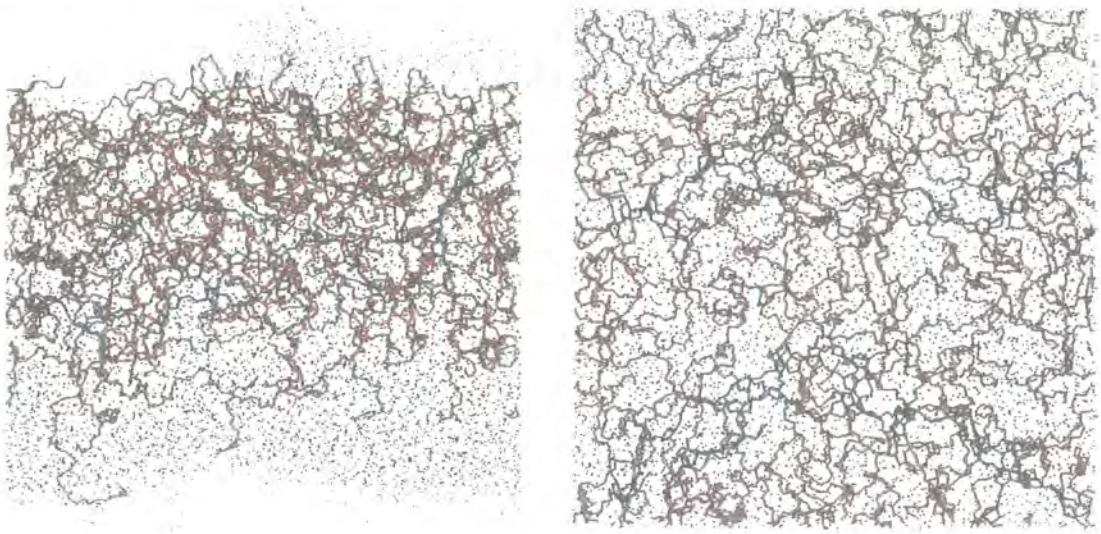

Figure 5.6: Side-view and top-view of eight amphiphilic polymer molecules at the air water interface. This snapshot was taken from the end of the MD simulation with softened polymer-polymer interactions, after 1 ns. Colours as in figure 5.2.

5.3.2.4 Restricting Motion of Water and Polymer Molecules

In response to the problems faced in the previous attempt, various restrictions were imposed upon the atomic positions in the system. First, all water molecules were frozen in the z-direction, to prevent their moving into the polymer blob and being absorbed. Also, the termini of the backbones were frozen in all three directions at the water interface to prevent them entering the bulk water. Finally, the temperature of the whole system was raised to 500 K to encourage faster reorganisation. Due to the use of the NVT ensemble and the positional freezing in the z-direction, there were no concerns regarding the boiling of the water layer, and such high temperatures could be simulated safely, without destroying the established density profile in the interfacial region. However, a bug in the then-current version of the DL_POLY

program caused a mis-handling of frozen atoms in systems involving more than one molecular type, and the various tethers used to hold the backbone in place failed to constrain their assigned atoms.

A confining potential, using tethers once again, was considered but rejected because of this bug. The plan would have been to place one polymer molecule into the simulation box complete with a set of tethers to confine it to a single quadrant of the box. Once the position of this molecule was firmly established, a second molecule would be introduced and tethered to another quadrant. It was hoped that molecules could be added in a stepwise fashion to obtain a good starting configuration, but sadly this idea had to be abandoned.

By this point, it had become clear that the idea of putting a collection of polymer molecules at the interface and allowing them to force one another's chains into the water was beyond the simulation time available. Instead, it was decided to carry out an initial equilibration of a polymer molecule in a confined geometry in the absence of water. These equilibrated molecules could then be placed at the water interface at various surface concentrations.

5.3.3 Final Attempt at Placing the Amphiphilic Polymer Molecules at the Water-Air Interface

Previous attempts to set up the polymer molecules at the interface in the pancake regime and allow them to restructure if appropriate into the brush conformation were unsuccessful. Attempts were therefore made to set up the system from the other extreme of the polymer's conformational behaviour. The polymer molecules were forced to adopt a brush conformation in this setup, and then allowed to relax if appropriate back to the pancake conformation during the simulation proper.

In order to force the polymer to adopt a brush-like structure, the fully stretched out, pancake form of a single polymer molecule was used as a starting point. In a technique similar to that used in a previous study of a related system,[161] the polymer molecule was surrounded by artificial walls represented by a repulsive potential. Unlike the previous study, however, where a region of space with a circular cross-section was used, here a region with spherocylindrical cross-section was adopted

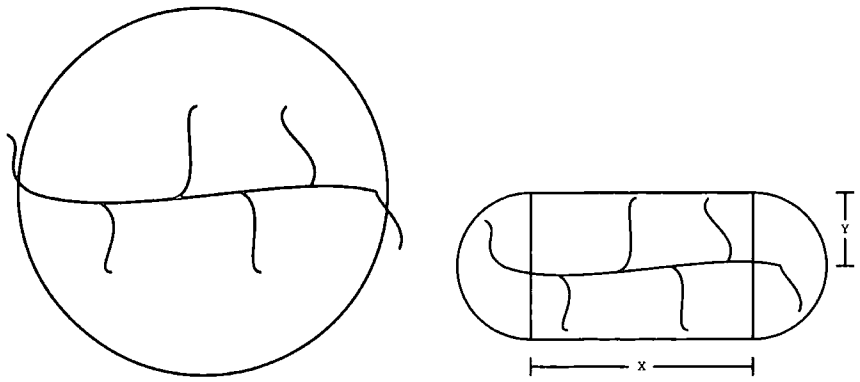

(a) circular cross-section

(b) spherocylindric cross-section

Figure 5.7: Two possible shapes of potential walls to emulate the effects of surrounding molecules.

(figure 5.7). The circular region has a severe disadvantage in that chains near the termini of the backbone have less free space in which to move than chains near the centre of the backbone, where the circular cross-section is at its widest. With a spherocylindrical cross-section, all chains along the backbone have a more equal share of the available space. Also, because the molecular shape more closely resembles a spherocylindrical cross-section than a circle, this new shaped box better represents the packing effects the polymer molecule experiences due to neighbouring molecules.

Several external potentials were imposed upon the polymer to get it to adopt a brush-like structure. A reduction in potential of 8.8 kJ mol^{-1} (corresponding to the heat of solution of an ethylene oxide repeat unit in water)[166] was granted to the system for each oxygen atom that fell below the idealised water interface, at $z = 0$. Hard wall potentials were employed to prevent PEO chains extending outside the spherocylindrical cross-section, and to prevent the hydrophobic backbone moving below the water interface. This whole system underwent a MC simulation to gradually compress the flat molecule into a brush structure. This was done by iteratively reducing both dimensions (x, the length of the rectangular region and y, the radius of the circular end caps and half the width of the rectangle) of the spherocylindrical cross-section and restarting the simulation from the previous end point. This process

was repeated until the polymer molecule was sufficiently compressed in the x- and y-directions to allow reasonable packing density into the water interface box for MD simulation. An initial target density was four such polymer molecules at the TIP4P water interface; this demanded that each polymer take up no more than 19 Å in one of the 76 Å interface dimensions ($2y \leq 19$ Å, and $2y + x \leq 76$ Å). Four systems were initially set up in the range of one to four polymer molecules at the water interface. It was later decided to try to further expand the range of surface concentrations simulated, so two additional setups were attempted, one with six molecules and one with eight. This task was not as straightforward as the previous systems, however, since with maximum compression using the spherocylindrical restriction technique, the minimum size that could reasonably be reached from a single molecule was not much less than the already obtained 19 Å.

A newly completed version of the Monte Carlo software capable of handling multiple molecules was employed, and the polymer molecule that had been compressed into the brush conformation was replicated five times (for six molecule simulation) and seven times (for eight molecule simulation) in separate MC simulations. The spherocylindrical confining potential was removed as the effects of other molecules were now included explicitly. The system was simulated under the NpT ensemble (complete with periodic boundary conditions), starting from a low density to allow the molecules free rotation. Rotation was restricted to being about the z-axis only, to ensure that the PEO sidechains continue to lie below $z = 0$. As the external pressure gradually caused a reduction in the box size, the polymer molecules were forced closer together. The molecules retained their brush-like structure due to systematic applications of molecular rigidity and external potentials (only those for submerged oxygen atoms since other molecules were at this point represented explicitly), intended to allow the molecules to relax as fully as possible and relieve some of the strain introduced due to their closer proximity. By significantly increasing the pressure on the system across a series of simulations, the molecular groupings were eventually brought to the 76 Å by 76 Å size, allowing direct transplantation into the MD simulation box. Figure 5.8 shows the final configuration of the polymer molecules after compressing to an appropriate density.

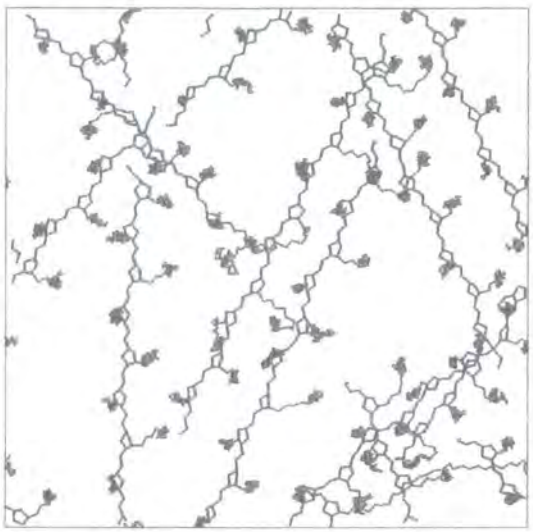

Figure 5.8: Top-view of eight amphiphilic polymer molecules as compressed using the Monte Carlo method. This snapshot shows the effect of periodic boundary conditions on the system. Colours as in figure 5.2, with simulation box in black.

Upon placing the polymer molecules at the TIP4P water interface, any water molecules overlapping with (or in close proximity to) any atoms in the newly introduced polymers were removed to prevent a high-energy starting configuration. Systems with more polymer molecules will inevitably have more polymer-water overlaps, and thus fewer water molecules after correction, as shown in table 5.1.

No. of Polymer Molecules at Surface	No. of Water Molecules	Surface Concentration / $mg\,m^{-2}$
1	10,157	0.3529
2	10,006	0.7057
3	9,899	1.0586
4	9,682	1.4114
6	9,194	2.1171
8	8,825	2.8229

Table 5.1: Various details on the six surface concentrations simulated.

Note on Comparison of Surface Concentrations from Experimental Studies

In the experimental studies of this system,[30] a variety of surface concentrations were studied with neutron reflectometry, using a larger polymer molecule with the

same structure. In the current study, ten norbornene repeat units, each with fifteen PEO units are used, however in the experimental study, a larger molecule with fifty norbornene units was used. It is therefore necessary to do a conversion calculation to establish how the surface concentrations used in the current work relate to those used in the experimental study.

With 2906 carbon, 1300 oxygen and 5612 hydrogen atoms, the experimentally studied polymer has a molecular mass of 61369.19 g mol^{-1}. Therefore, in 1 mg of the polymer, there are 9.81×10^{15} molecules. As the simulated molecule is one fifth the length (ten vs. fifty norbornene units) of the experimental molecule, we can say that 1 mg of the experimental polymer is equivalent to 4.91×10^{16} of the simulated molecules. This allows the set up of a conversion table to convert between experimental surface concentration and the number of molecules in the simulation box (table 5.2).

Experimental Surface Concentration / mg m^{-2}	No. of Molecules in Simulation Box
0.3	0.85
0.4	1.13
0.5	1.42
0.7	1.98
1.0	2.83
1.5	4.25
2.0	5.67
2.5	7.09
3.0	8.50
3.5	9.92
4.0	11.34

Table 5.2: Equivalence of experimental surface concentration and simulation box population.

With these surface concentrations, we can make direct comparisons between simulation and experiment for these systems. Higher experimental surface concentrations are currently unattainable in simulation, however, as the simulation box is already overcrowded with just eight molecules.

5.3.4 Simulations of Several Polymer Molecules and Analysis of Simulation Trajectories

MD Simulations of these systems made use of a fitted force field obtained previously (chapter 4). In each case, 1,500,000 steps of 2 fs were performed, using a 7 Å charge-group based cutoff at 300 K using the NVT ensemble. Due to the size of the system, atomic coordinates could only be dumped once every 10,000 steps. All bond lengths were constrained to their equilibrium lengths (taken from the OPLS-AA force field) using the SHAKE algorithm.

There are a number of different data sets that can be extracted from these simulations. The most interesting ones are listed here.

5.3.4.1 Neutron Reflectivity

The most important data that can be extracted from the simulations of the amphiphilic polymers is the density profile, which is easily converted to a simulated neutron reflectometry profile. The experimental systems have had the background reflectivity subtracted, so in all plots of reflectivity (simulated and experimental), a constant background of 5.00 x 10^{-6} will be added to the reflectivity values in this study. This will allow more objective comparisons to be made between the various systems. There were three separate contrasts studied experimentally: deuterated PEO on NRW, protonated (hydrogenous) PEO on D_2O and deuterated PEO on D_2O. In all cases, the polynorbornene backbone was fully hydrogenous. The same simulation trajectory can be used to generate a neutron reflectivity profile for each of these contrasts, if the assumption is made that molecular organisation is independent of isotopic substitution. This assumption is totally reasonable in this case, and was previously made in the experimental study to justify the comparisons drawn between the various contrasts.

5.3.4.2 Radii of Gyration

Using the method outlined in chapter 1, it is possible to calculate the average radius of gyration for the PEO grafts. However, with slight modification, the calculation of

the radius of gyration can be more useful. Rather than simply calculating a single value for R_g, it is possible to generate one-dimensional *partial radii of gyration* ($R_{g,x}$, $R_{g,y}$ and $R_{g,z}$) for the system. These partial radii of gyration are defined in equation 5.7,

$$R_{g,d} = \sqrt{\frac{\sum_{i=1}^{n} m_i s_{i,d}^2}{\sum_{i=1}^{n} m_i}}, \tag{5.7}$$

where

m_i is the mass of atomic site i and

$s_{i,d}$ is the distance between atomic site i and the polymer's centre of mass in dimension d (x, y or z).

These values can then be used to give a more quantitative picture of the structure by comparing the $R_{g,x}$ and $R_{g,y}$ values with $R_{g,z}$. The partial radius of gyration in the z-direction will be expected to be smaller than its x and y counterparts for a pancake structure, and larger for a brush.

5.3.4.3 Dihedral Angle Distributions

It is possible to break down the PEO side chains into sequences of O-C-C-O and C-O-C-C dihedrals. The population distributions in these dihedrals can then be compared to other experimental and simulated studies. In addition, the chains can be broken down into overlapping DME-like C-O-C-C-O-C sequences which can also be analysed and compared to the conformational distribution of DME itself.

5.4 Results

5.4.1 Neutron Reflectometry and General Observations

5.4.1.1 One Molecule at the Interface

The simulation involving one amphiphilic polymer molecule at the water-air interface was set up (figure 5.9) such that the polymer molecule lies close to the box-diagonal in order to minimise the chance of any interaction with its own periodic images. This setup becomes more difficult as the box population increases in the larger

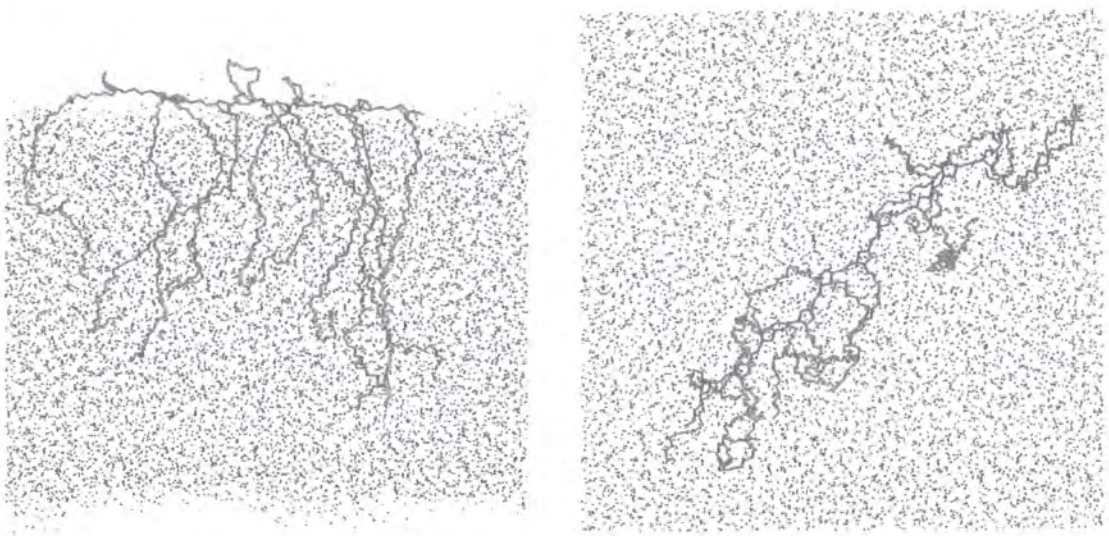

Figure 5.9: Side-view and top-view of one amphiphilic polymer molecule at the air water interface. This snapshot was taken from the beginning of the MD simulation. Colours as in figure 5.2.

simulations, and diagonal geometries involve each molecule potentially crossing more than one periodic boundary.

It is immediately clear that during the course of the simulation, the polymer molecule has rearranged itself from a brush-like structure into a more appropriate pancake structure. Indeed the pancake is the expected structure for such a low surface concentration as this. The PEO chains have spread out laterally and moved almost completely out of the bulk water by the end of the simulation. On analysis of the MD trajectory, it can be seen that the chains begin to retract towards the interface almost immediately, and after 1.08 ns, a pancake structure has already been formed, with just one or two PEO chains occasionally extending significantly into the bulk water. By 2.12 ns, the last of these errant chains has been captured and incorporated into the pancake, which persists until the end of the simulation (3 ns) (figure 5.10).

Using the simulation trajectory dump file, it is possible to produce a density profile which shows how the densities of the three main components (water, backbone and sidechains) vary across the simulation box. The profile in figure 5.11 shows the change in density along the z-axis, perpendicular to the water surfaces.

This density profile is easily converted to a number density profile (figure 5.12),

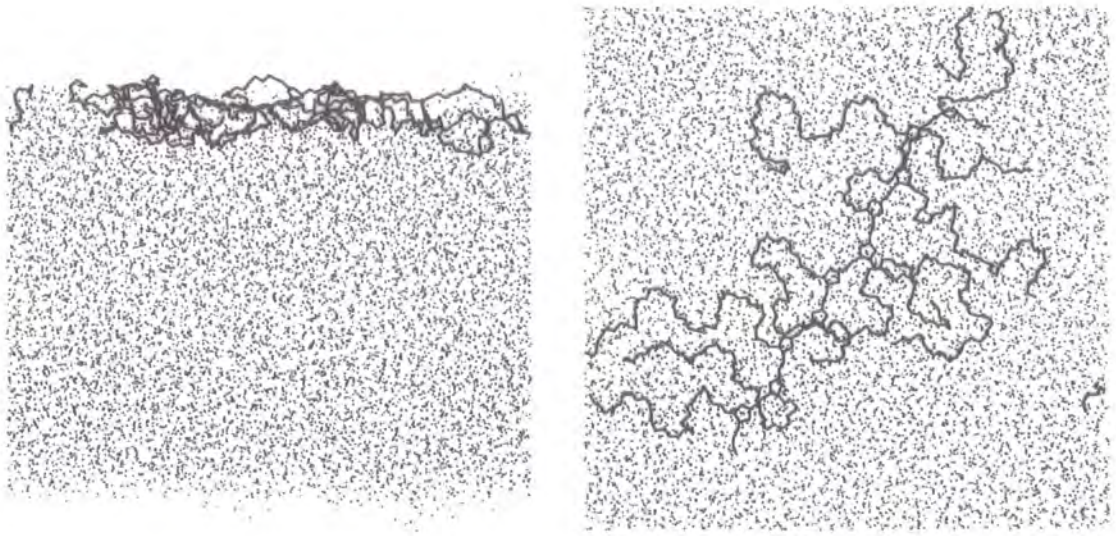

Figure 5.10: Side-view and top-view of one amphiphilic polymer molecule at the air water interface. This snapshot was taken from the end of the MD simulation. Colours as in figure 5.2.

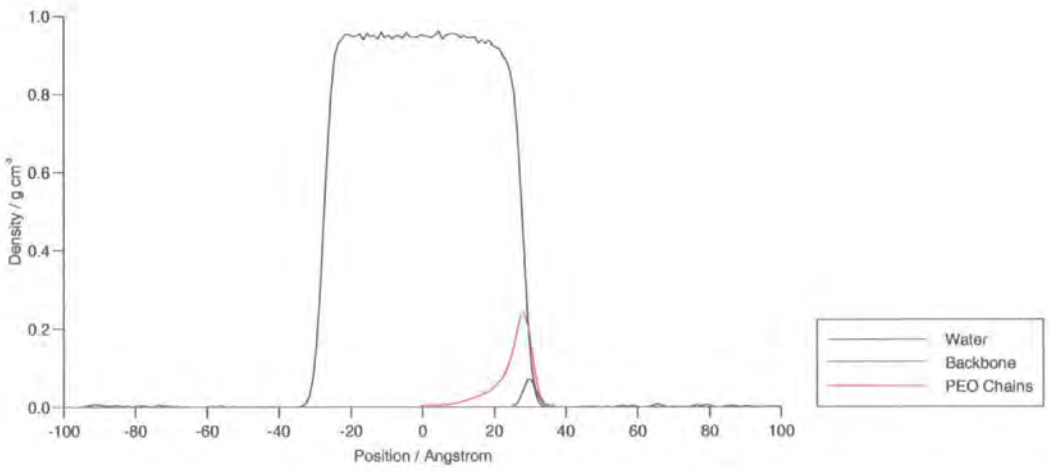

Figure 5.11: Density profile from the simulation of one amphiphilic polymer molecule at the water-air interface. Averaged over the full 3 ns of simulation time.

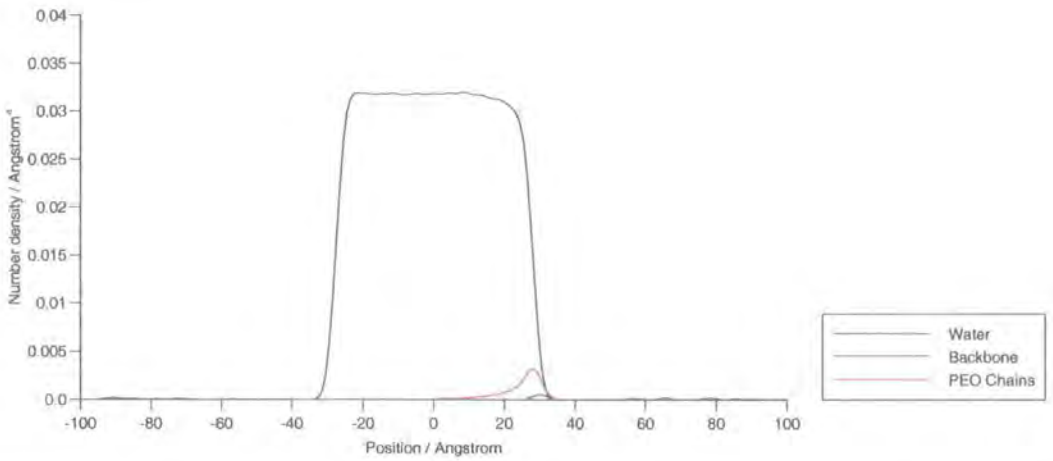

Figure 5.12: Number-density profile from the simulation of one amphiphilic polymer molecule at the water-air interface. Averaged over the full 3 ns of simulation time.

which shows the number of water molecules, norbornene units and EO units per unit volume. This in turn is converted to a scattering length density profile for use in calculating a neutron reflectometry profile. Figure 5.13 shows the scattering length density as a function of position in a direction perpendicular to the water surface. The image appears reversed when compared to the density profiles due to a difference in direction conventions adhered to by the various programs used to generate these data.

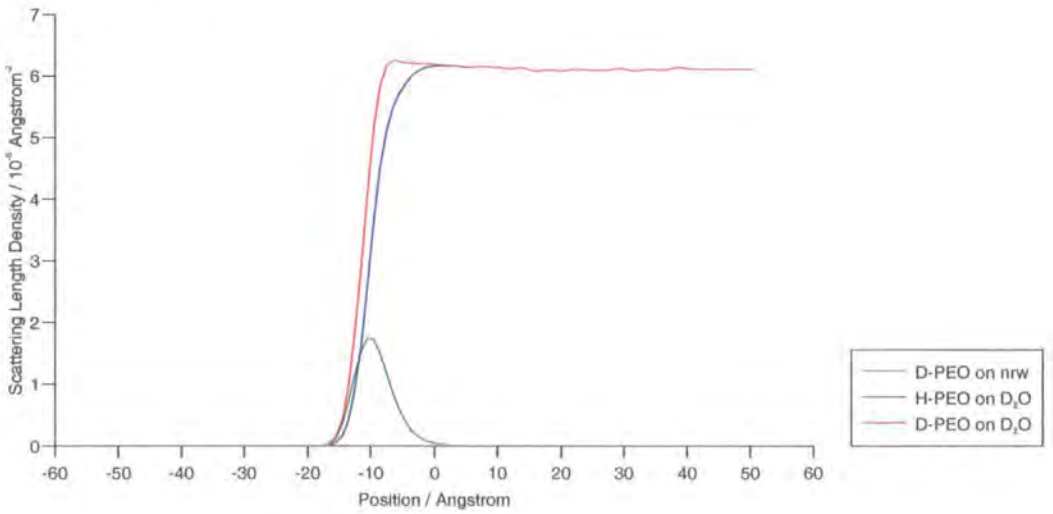

Figure 5.13: Scattering length density profiles calculated using the simulation of a single polymer molecule at the water surface. Air is at low z and bulk water is at high z. D indicates deuterated PEO, while H represents hydrogenous PEO.

The density of the water in the bulk region (between the interfaces) is of slightly lower density than typical bulk water. As scattering length density (SLD) is a function of density, the SLD calculated for the "bulk" water region in this system was slightly lower than that of real bulk water. As a result, a discontinuity was apparent in the SLD profile at around 40 Å where the simulated bulk water region ends and the subphase region is assumed to begin. To counter this, the value for scattering length density of D_2O used for each neutron reflectivity profile generated has had to be slightly adjusted to fall into line with the simulation density of water. In this case, a scattering length density of 6.10 x 10^{-6} Å $^{-2}$ has been adopted for pure water (subphase), rather than the usual value of 6.35 x 10^{-6} Å $^{-2}$. This correction is necessary because it is the discontinuity in SLD between adjacent layers that gives rise to neutron reflection.

Examination of the density profiles in figures 5.11 and 5.12 shows that the chains extend a long way into the bulk water. This is due to the fact that this density profile is made up of data from simulation steps before the PEO chains had completely retracted into the pancake structure. In all following sections, the neutron reflectometry data is constructed from density profiles which only include atomic positions from the final 1 ns of simulation. Figure 5.14 shows such a density profile for a single molecule at the water surface.

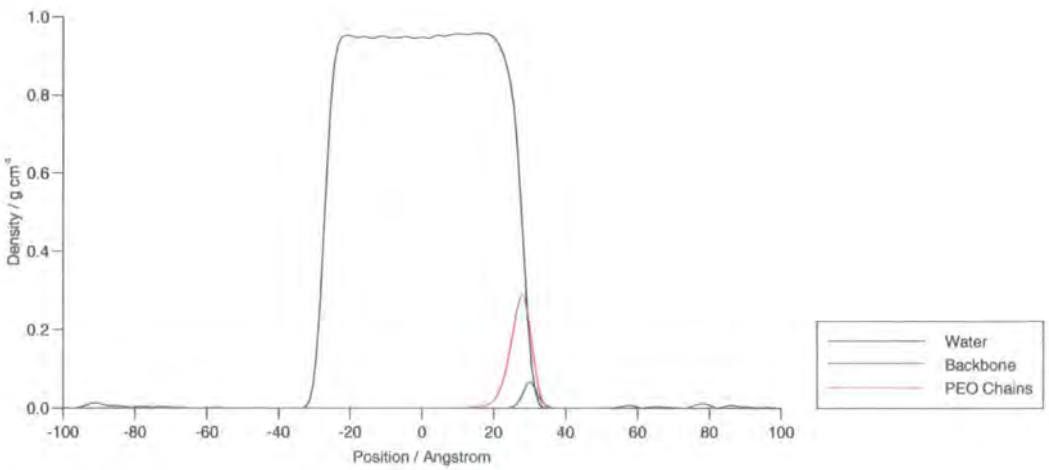

Figure 5.14: Density profile of the three components from the simulation of one amphiphilic molecule at the water interface.

Using the scattering length density profile, it is possible to generate a neutron

reflectivity plot to compare simulation and experiment. From tables 5.1 and 5.2, it is clear that the simulation of one molecule at the interface lies roughly midway between two of the experimentally studied surface concentrations. It is therefore logical to plot the reflectivity profiles of these three systems together for comparison (figure 5.15).

5.4.1.2 Two Molecules at the Interface

Figure 5.16 shows the starting configuration for this simulation. As was the case in the one molecule simulation, here the polymers also form a pancake layer at the interface. Here, however, there still appear to be chains exhibiting some brush character, extending into the bulk water to a small extent. There is no entanglement of chains; the two polymer molecules are clearly still separate entities at the end of the simulation (figure 5.17).

5.4.1.3 Three Molecules at the Interface

To introduce some orientational disorder into the system, the three molecule simulation was set up with the polymer backbones forming a rough equilateral triangle, shown in figure 5.20. Once again, a pancake structure is formed by the molecules, but with several chains still extending into the bulk water.

5.4.1.4 Four Molecules at the Interface

A number of different configurations were attempted for the four molecule simulation, including (with respect to the polymer backbone) squares and cross shapes. It was found that none of these configurations would fit into the box, however, without unfavourably close contacts and complete overlaps between atoms on different molecules. The configuration eventually settled on was the simple one shown in figure 5.24, with all four polymer backbones roughly in the same direction with approximately equal spacing.

Again, the polymer chains have spread out laterally, and the initial brush has collapsed to a structure rather like a flattened brush (figure 5.25).

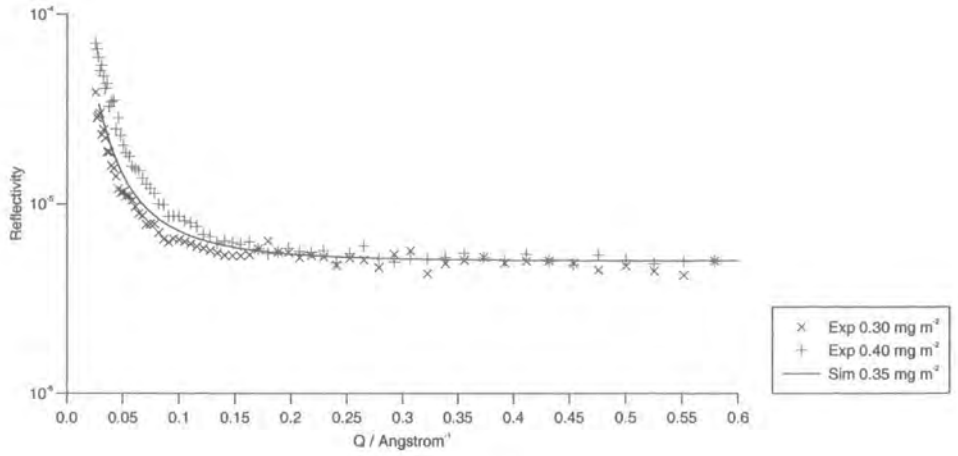

(a) deuterated on NRW

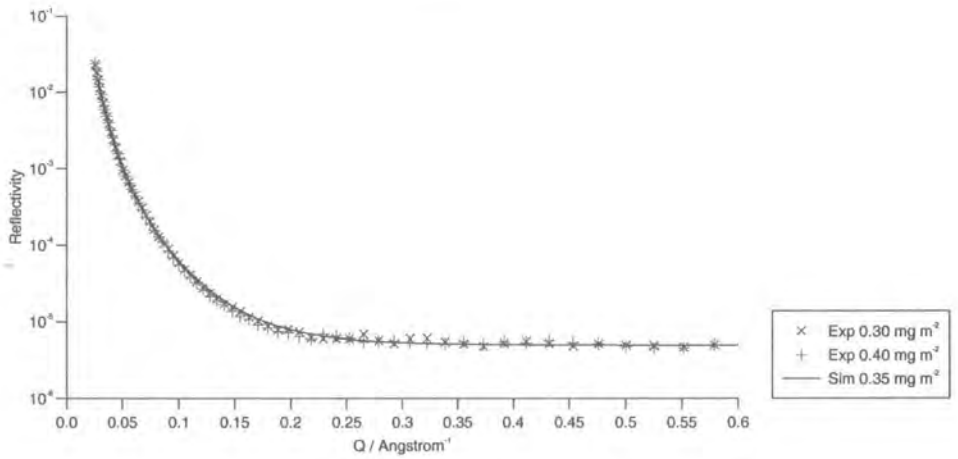

(b) protonated on D2O

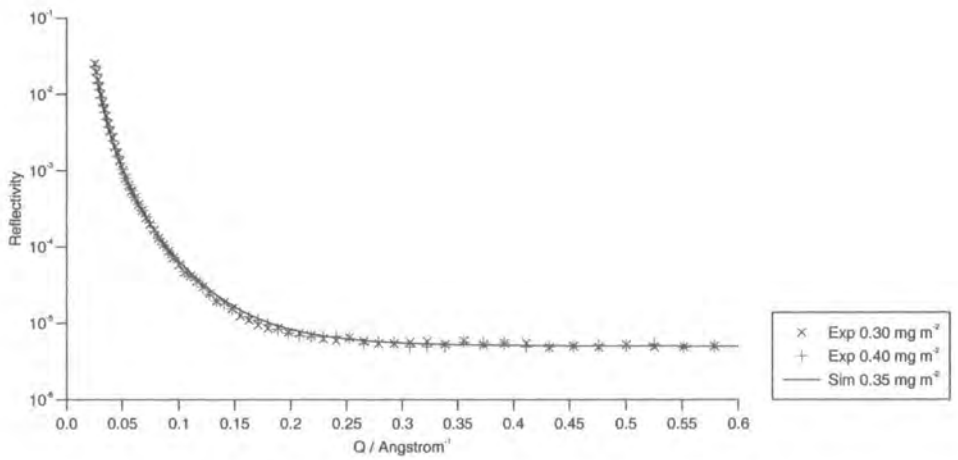

(c) deuterated on D2O

Figure 5.15: Neutron reflectivity profiles for the simulation of one molecule at the water interface.

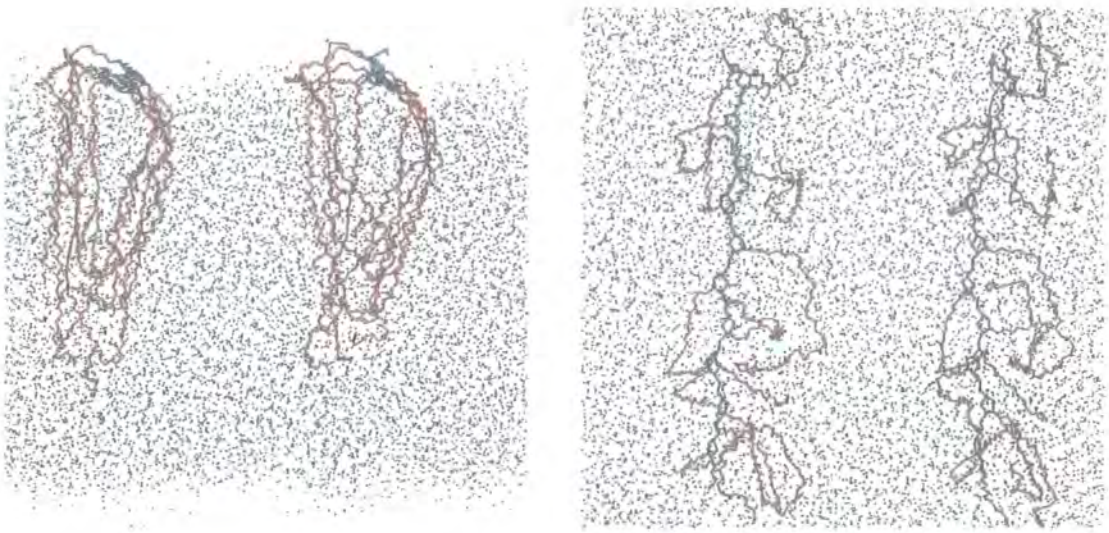

Figure 5.16: Side-view and top-view of two amphiphilic polymer molecules at the air water interface. This snapshot was taken from the beginning of the MD simulation. Colours as in figure 5.2.

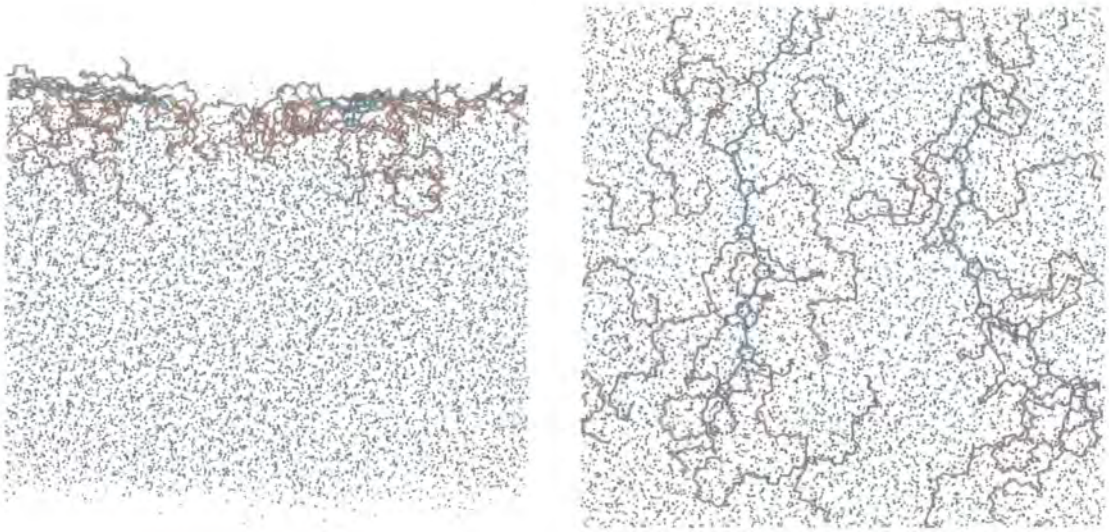

Figure 5.17: Side-view and top-view of two amphiphilic polymer molecules at the air water interface. This snapshot was taken from the end of the MD simulation. Colours as in figure 5.2.

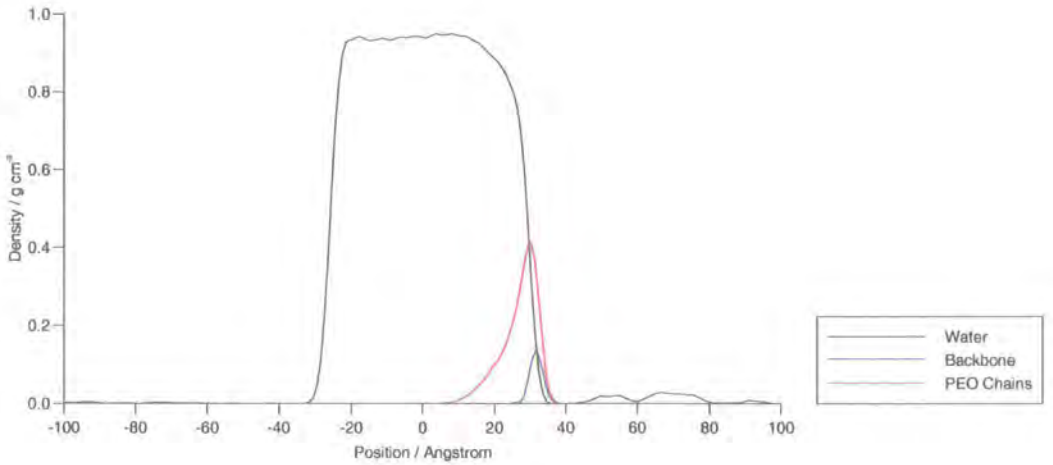

Figure 5.18: Density profile of the three components from the simulation of two amphiphilic molecule at the water interface.

5.4.1.5 Six Molecules at the Interface

As noted in section 5.3.3, the six- and eight-molecule simulations required more severe compression at the Monte Carlo stage, to compress the additional molecules into the already crowded simulation box. The effects of this compression can be seen clearly in figure 5.28, where the chains are close to a perfect brush structure; the side view shows almost fully extended chains, and the top view shows that most chains are very close to lying in the z-direction.

The overcrowding of the simulation box is not without consequence; figure 5.29 shows severe buckling of at least one polymer backbone, which has been forced down into the bulk liquid during the final simulation.

5.4.1.6 Eight Molecules at the Interface

This system is even more strained than the six molecule system. Figure 5.32 shows a very crowded simulation box at the beginning of the simulation. This time, the distortions occurring during the main simulation are even more severe; not only have many of the polymer backbones buckled, but they have also been drawn beneath the water surface. Figure 5.33 shows that the interface has also been damaged, and is no longer near-planar.

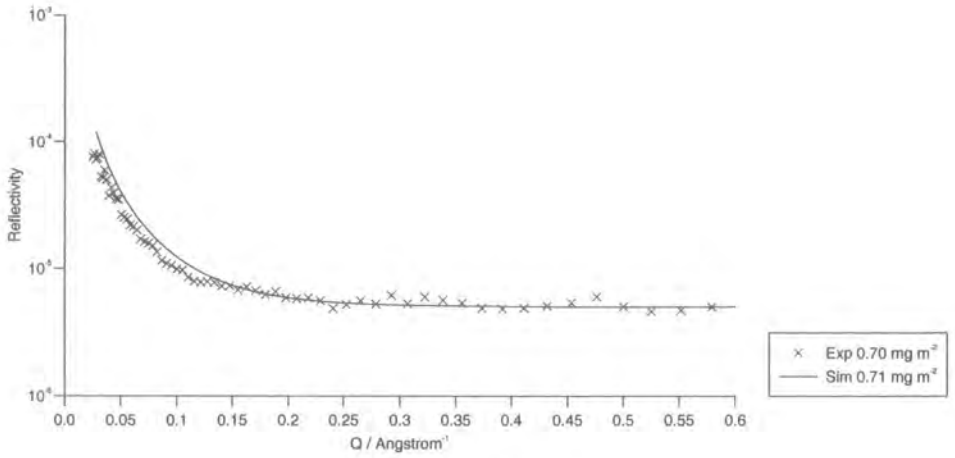

(a) deuterated on NRW

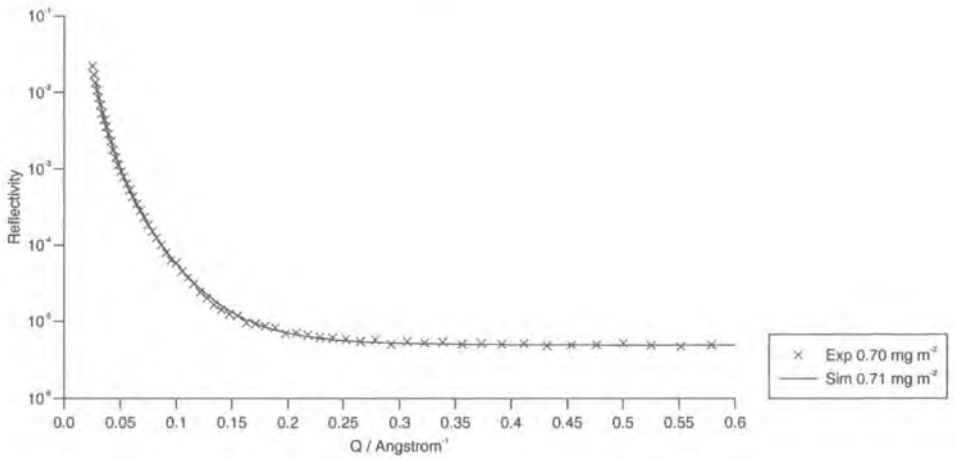

(b) protonated on D2O

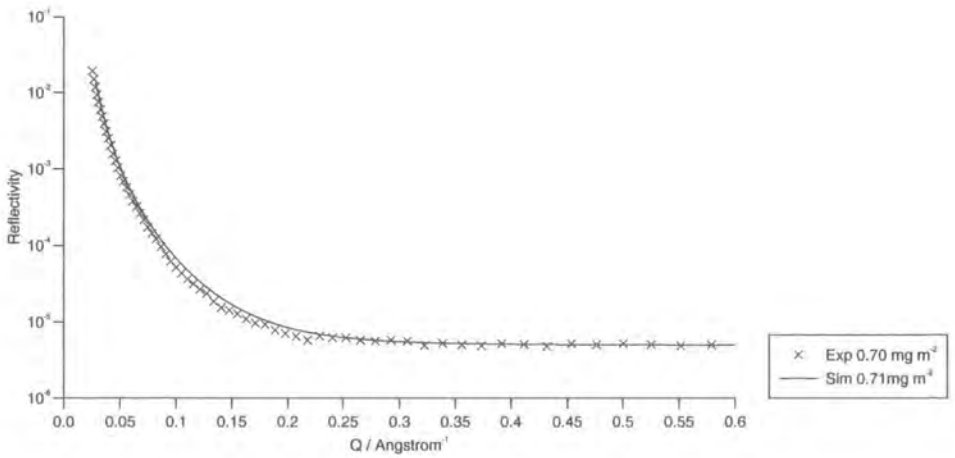

(c) deuterated on D2O

Figure 5.19: Neutron reflectivity profiles for the simulation of two molecules at the water interface.

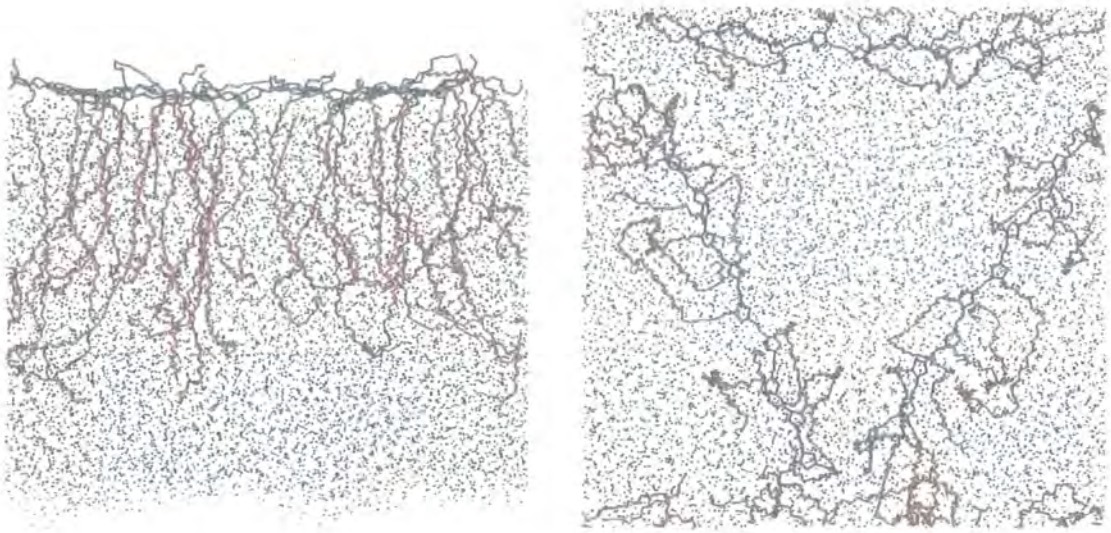

Figure 5.20: Side-view and top-view of three amphiphilic polymer molecules at the air water interface. This snapshot was taken from the beginning of the MD simulation. Colours as in figure 5.2.

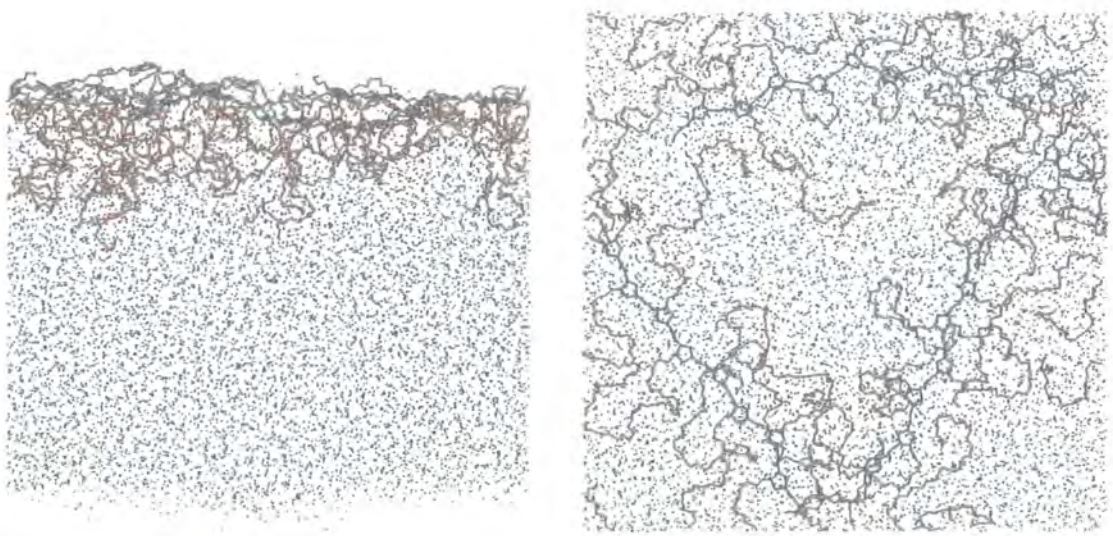

Figure 5.21: Side-view and top-view of three amphiphilic polymer molecules at the air water interface. This snapshot was taken from the end of the MD simulation. Colours as in figure 5.2.

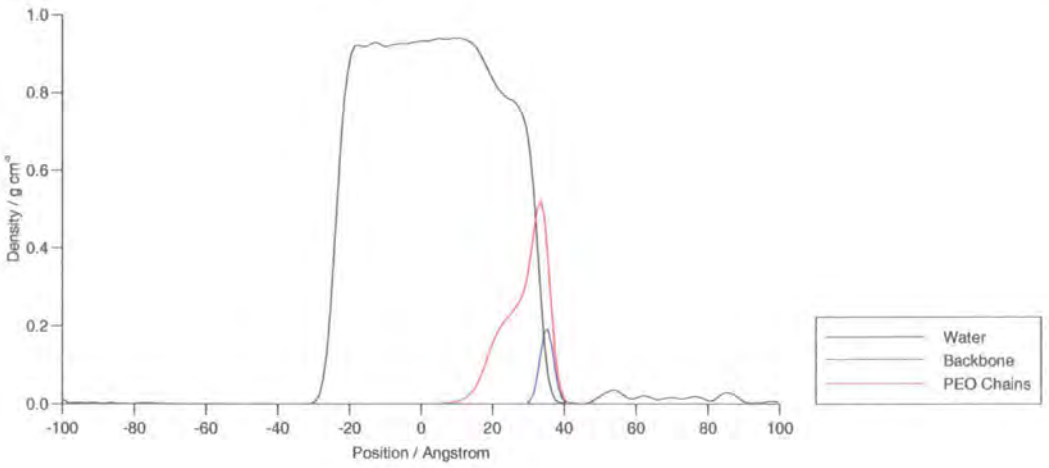

Figure 5.22: Density profile of the three components from the simulation of three amphiphilic molecule at the water interface.

5.4.2 Radii of Gyration

By applying equation 5.7 to the trajectory data for the PEO side chains alone, the full and partial radii of gyration have been calculated as averages across all chains in the system. Figure 5.36 shows the variation in these quantities with time throughout the six simulations. Table 5.3 gives values for R_g and $R_{g,z}$ for both PEO and backbone, averaged over all chains in the system, and also over the final 1 ns of simulation time.

	PEO Grafts		Backbone	
Simulation	R_g	$R_{g,z}$	R_g	$R_{g,z}$
1 molecule	7.98	2.29	18.50	1.47
2 molecules	8.09	3.63	18.25	1.50
3 molecules	7.44	4.12	18.41	1.37
4 molecules	7.95	5.15	18.46	1.74
6 molecules	8.80	7.31	17.53	3.12
8 molecules	9.16	7.86	17.83	2.87

Table 5.3: Full and partial (z-direction) radii of gyration (Å) for the two polymer components. All values are averaged over all molecules, and across the final 1 ns of simulation.

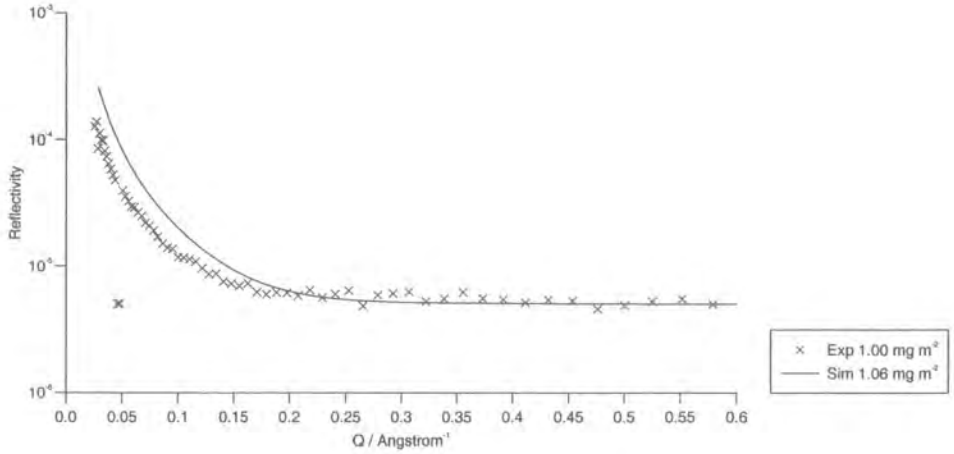

(a) deuterated on NRW

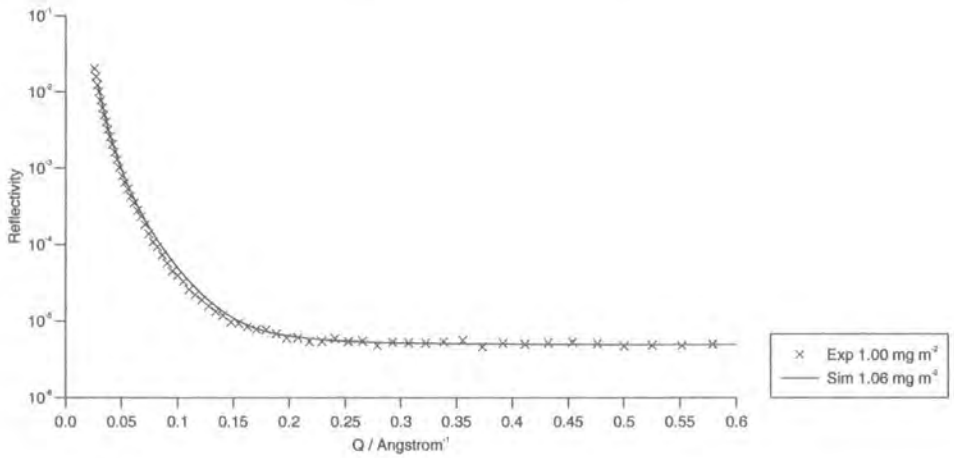

(b) protonated on D2O

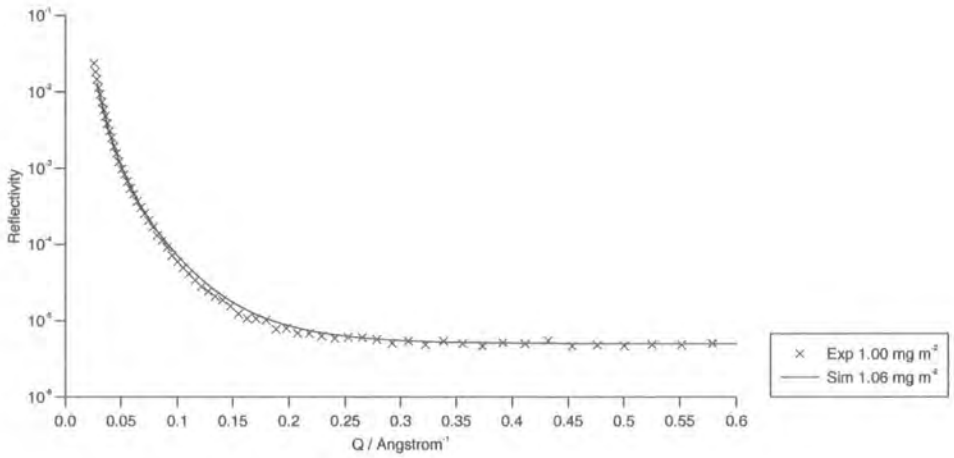

(c) deuterated on D2O

Figure 5.23: Neutron reflectivity profiles for the simulation of three molecules at the water interface.

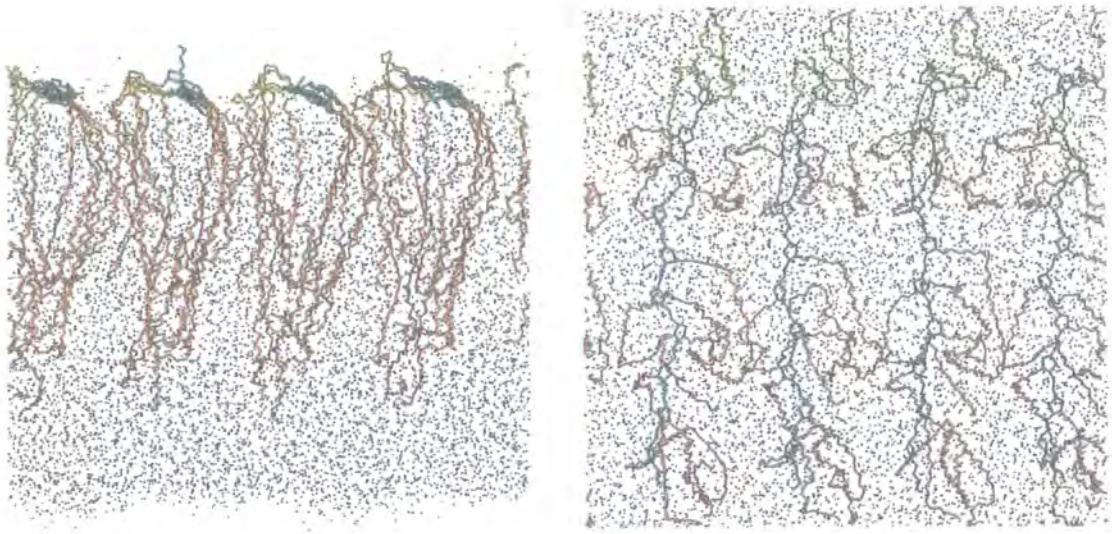

Figure 5.24: Side-view and top-view of four amphiphilic polymer molecules at the air water interface. This snapshot was taken from the beginning of the MD simulation. Colours as in figure 5.2.

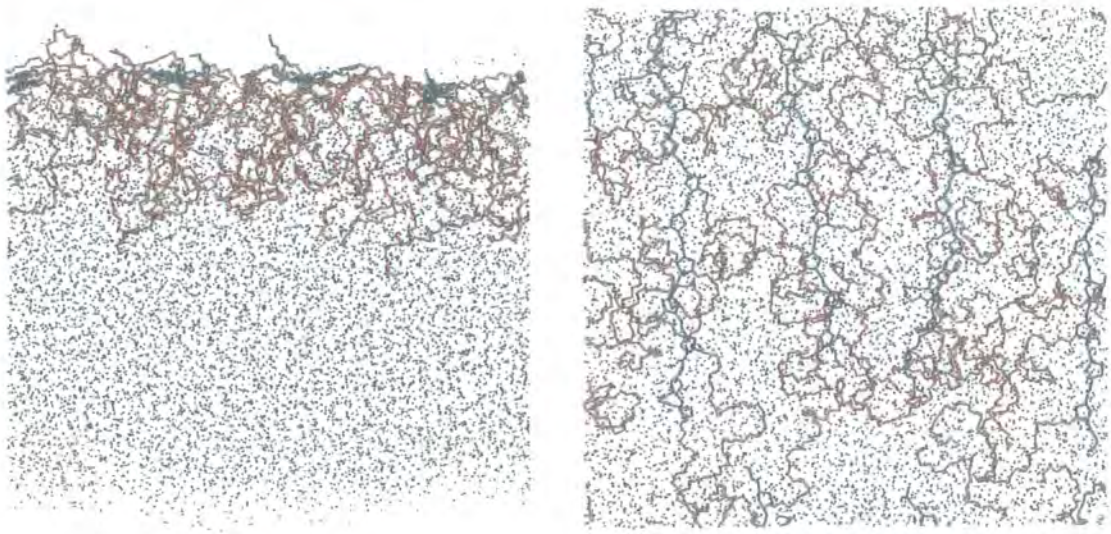

Figure 5.25: Side-view and top-view of four amphiphilic polymer molecules at the air water interface. This snapshot was taken from the end of the MD simulation. Colours as in figure 5.2.

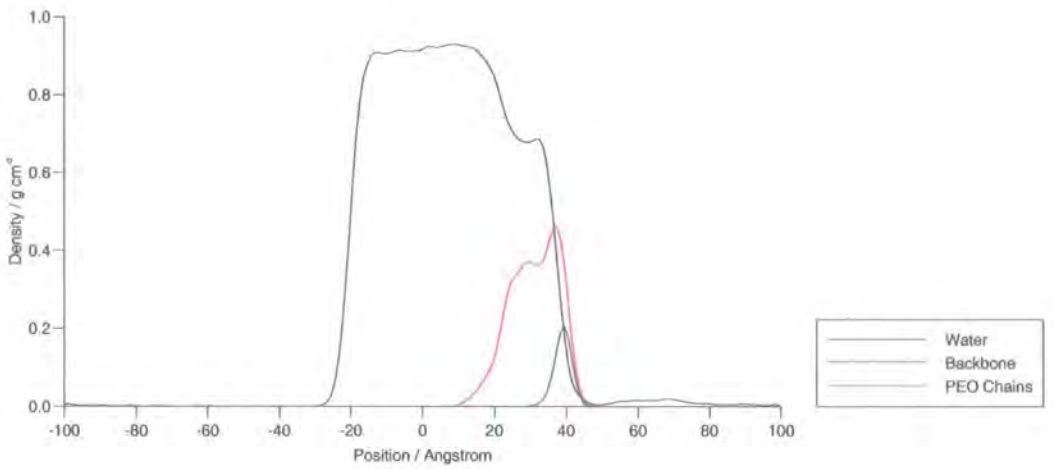

Figure 5.26: Density profile of the three components from the simulation of four amphiphilic molecules at the water interface.

5.4.3 Dihedral Angle Analysis

The major dihedrals in the PEO side chains have been categorised according to the distribution of *trans* and *gauche* conformations, using data from the final 1 ns of simulation time. Table 5.4 shows a sample of the data, collected for the four molecule simulation, and encompassing all time steps in the final 1 ns. Most of the other simulations yield data similar to this, except the two molecule simulation.

The two molecule simulation differs from the others in that the average conformational distribution for internal O-C-C-O units was $g^- = 47.32\%$, $t = 10.46\%$ and $g^+ = 42.21\%$. This appears to be due to an unusually large number of O-C-C-O dihedrals (rather than just one or two) being in the *trans* state throughout the chains. There appears to be no significant corresponding deviation in the C-O-C-C dihedral. The O-C-C-O *trans* population averaged throughout the entire simulation was over 20%, indicating that the starting conditions in this simulation were not particularly good.

Table 5.5 gives the conformational populations in the overlapping DME-like units that run along the PEO side chains.

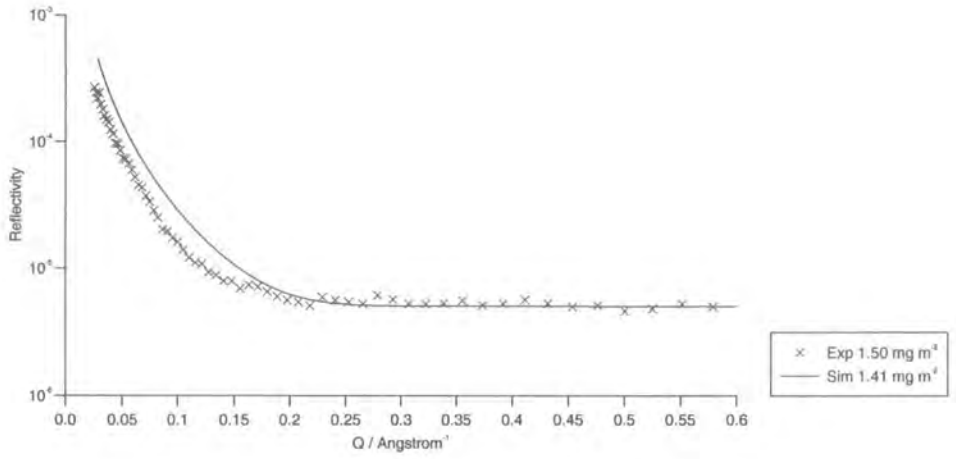

(a) deuterated on NRW

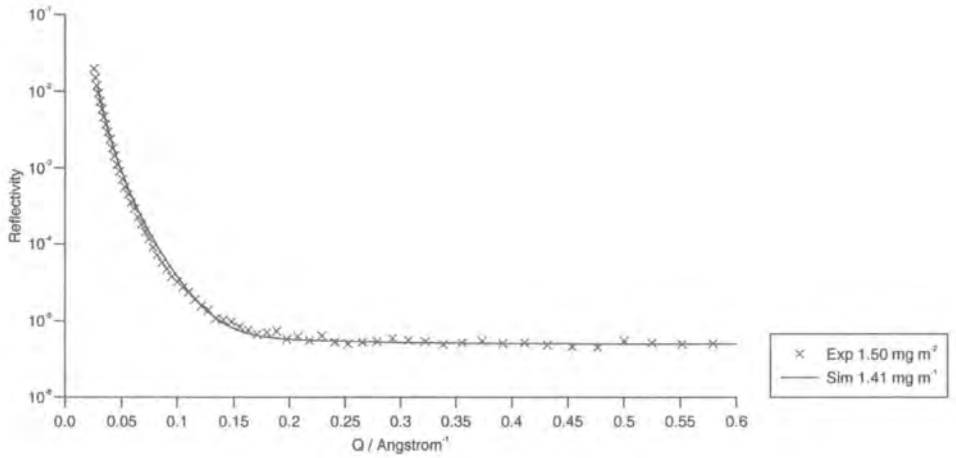

(b) protonated on D2O

Figure 5.27: Neutron reflectivity profiles for the simulation of four molecules at the water interface.

O-C-C-O	%			Flips
	g^-	t	g^+	
Internal	46.42	3.65	49.93	26
Terminal	53.90	0.15	45.95	25

C-O-C-C	%			Flips
	g^-	t	g^+	
Internal	4.67	90.72	4.61	9
Terminal	4.40	89.85	5.75	10

Table 5.4: Conformational distributions for the PEO side chains in the four molecule simulation (final 1 ns). *Terminal* indicates the last such dihedral in the chain (O-H end) while *internal* is the average of all other dihedrals in the chain. *Flips* represents the average number of conformational transitions per dihedral type during the simulation.

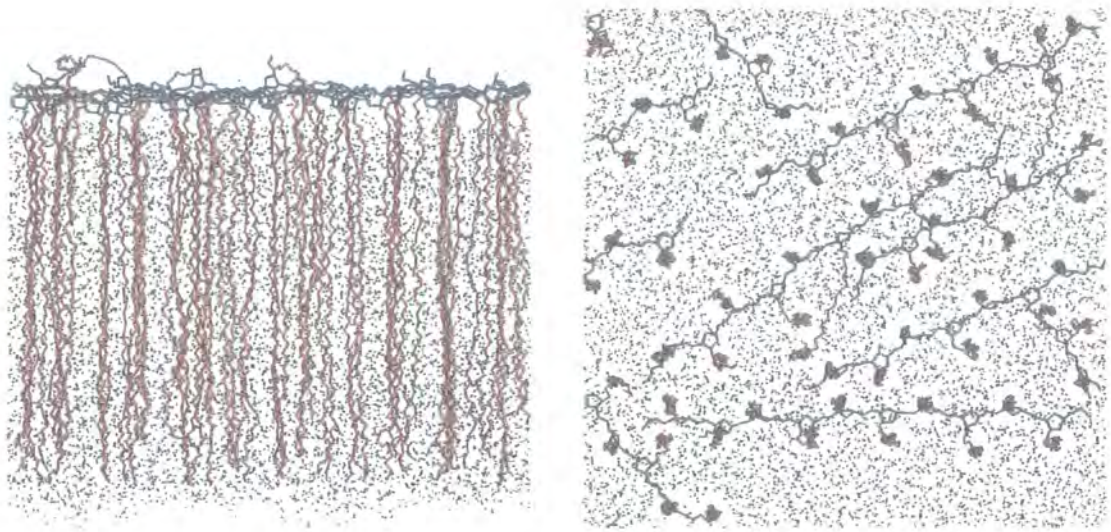

Figure 5.28: Side-view and top-view of six amphiphilic polymer molecules at the air water interface. This snapshot was taken from the beginning of the MD simulation. Colours as in figure 5.2.

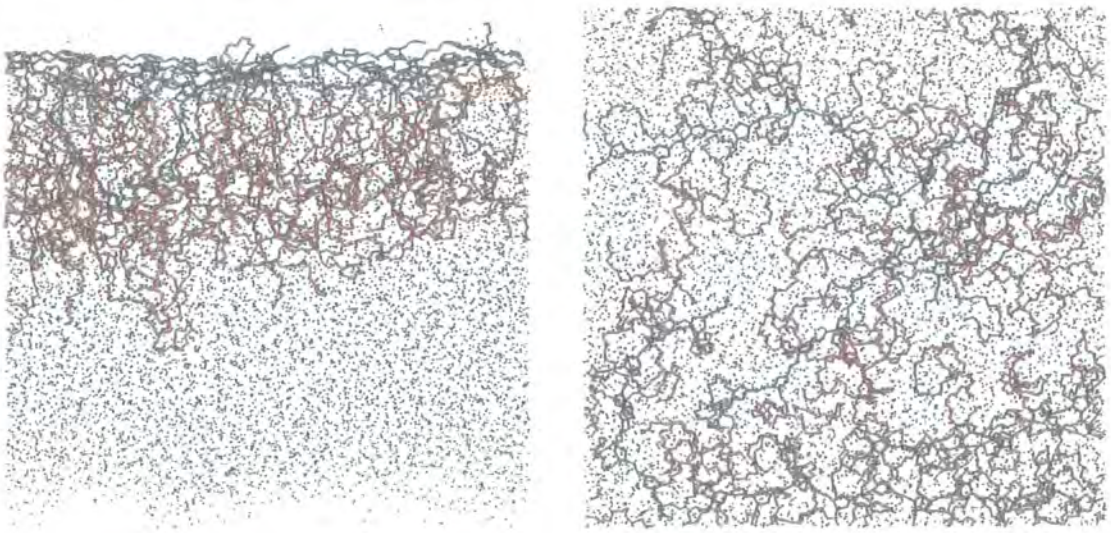

Figure 5.29: Side-view and top-view of six amphiphilic polymer molecules at the air water interface. This snapshot was taken from the end of the MD simulation. Colours as in figure 5.2.

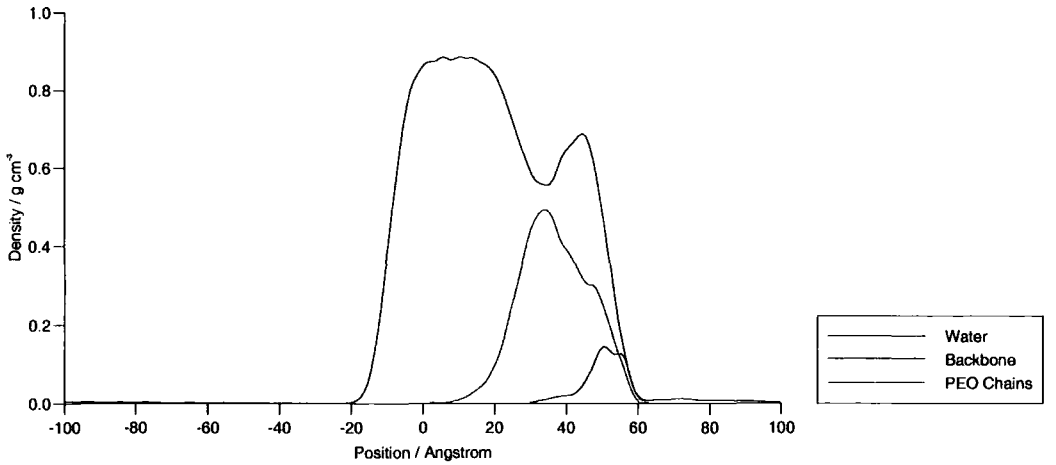

Figure 5.30: Density profile of the three components from the simulation of six amphiphilic molecule at the water interface.

N	ttt	tgt	ttg	tgg	tgg'	ggg	ggg'	gg'g	gtg	gtg'
1	3.80	76.27	0.96	8.96	8.50	0.19	1.06	0.23	0.00	0.04
2	8.46	70.85	1.89	12.35	5.24	0.49	0.59	0.01	0.08	0.04
3	3.66	77.56	0.90	8.82	7.41	0.47	1.03	0.15	0.00	0.00
4	2.76	80.15	0.84	8.74	6.04	0.32	0.92	0.18	0.03	0.03
6	3.46	77.61	1.11	10.09	6.27	0.41	0.75	0.20	0.05	0.04
8	5.69	73.09	1.75	10.42	7.11	0.46	1.10	0.23	0.11	0.06

Table 5.5: Conformational distribution in the sequence of overlapping DME-like units along the PEO side chains (final 1 ns). N is the number of polymer molecules at the interface.

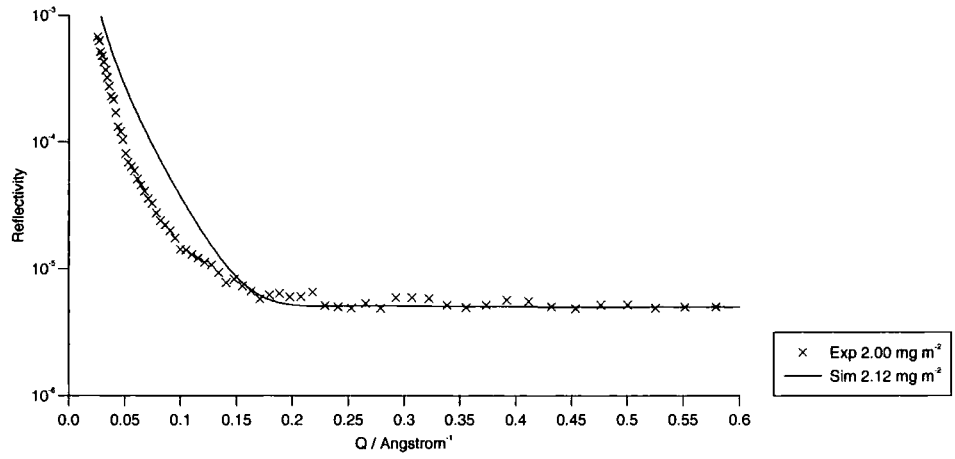

(a) deuterated on NRW

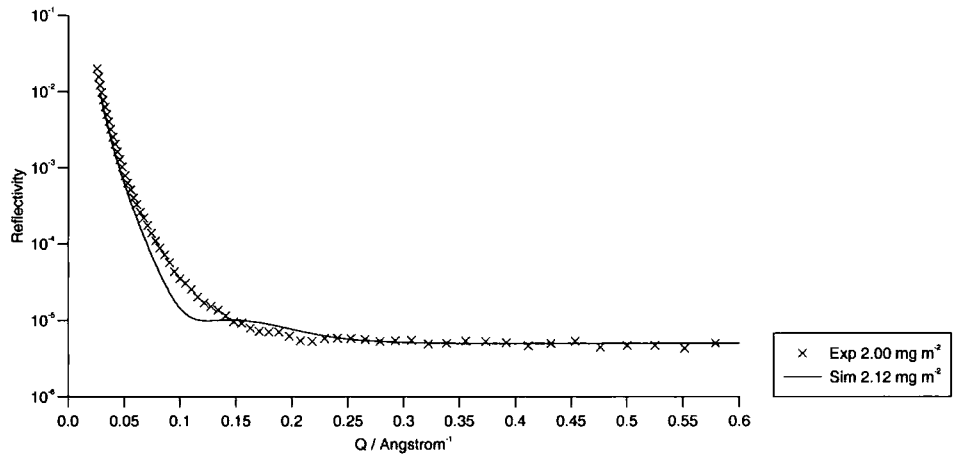

(b) protonated on D2O

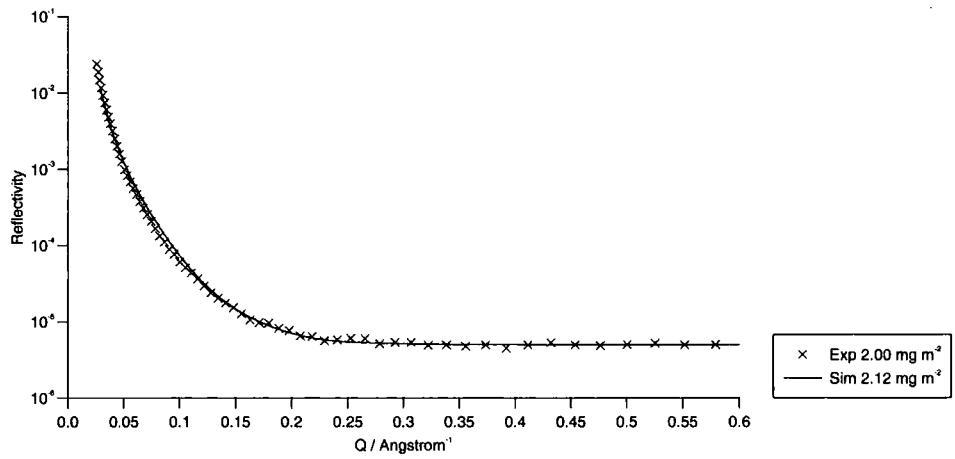

(c) deuterated on D2O

Figure 5.31: Neutron reflectivity profiles for the simulation of six molecules at the water interface.

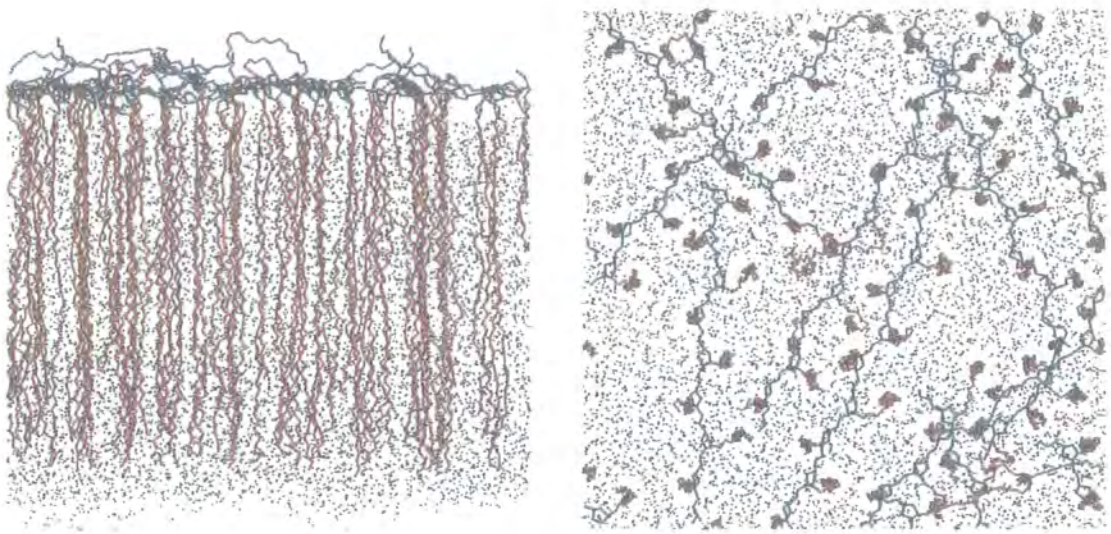

Figure 5.32: Side-view and top-view of eight amphiphilic polymer molecules at the air water interface. This snapshot was taken from the beginning of the MD simulation. Colours as in figure 5.2.

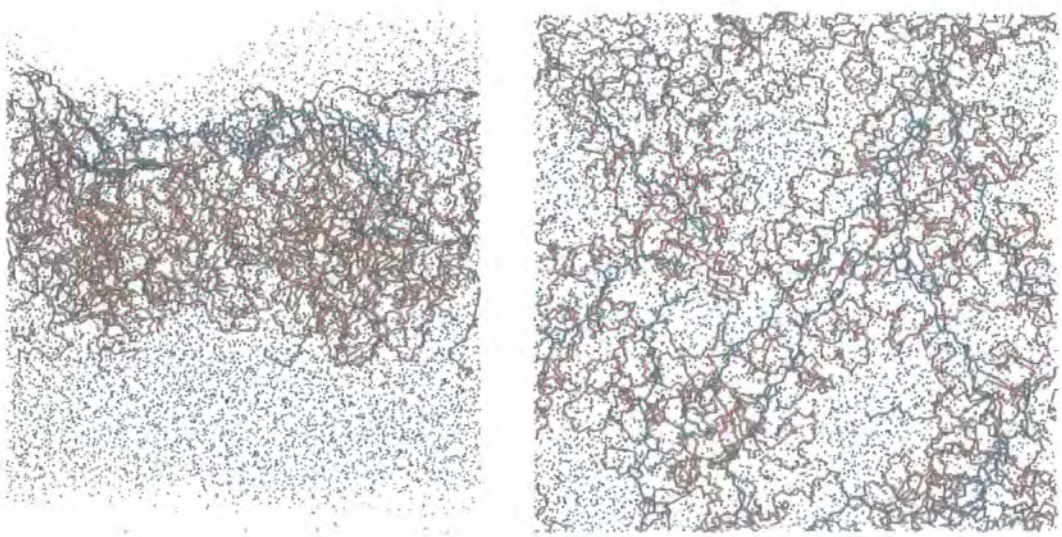

Figure 5.33: Side-view and top-view of eight amphiphilic polymer molecules at the air water interface. This snapshot was taken from the end of the MD simulation. Colours as in figure 5.2.

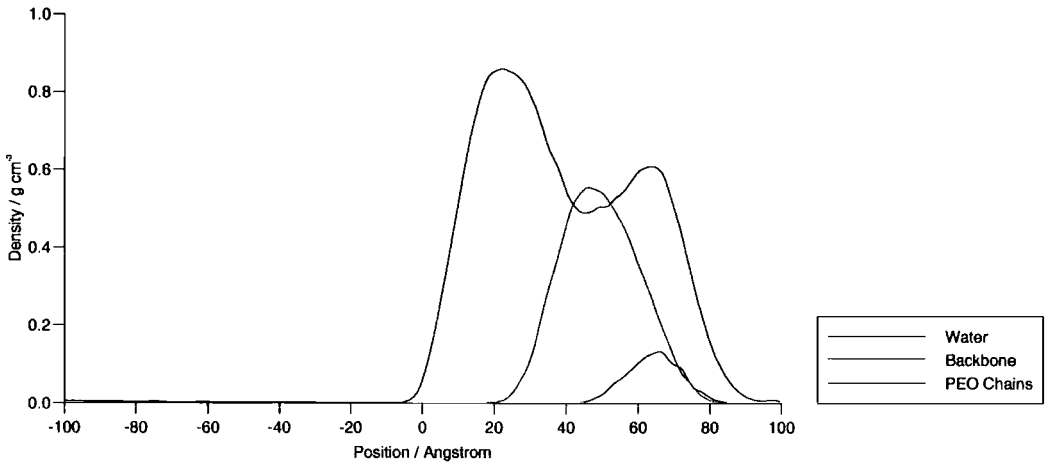

Figure 5.34: Density profile of the three components from the simulation of eight amphiphilic molecule at the water interface.

5.5 Discussion

5.5.1 Density Profiles

The end-point snapshots from the initial one molecule simulation (starting from a pancake structure, figure 5.3) and the second one molecule simulation (starting from a brush structure, figure 5.10) both show the same result, in that the system prefers to adopt a pancake structure at a water-air interface. This is encouraging, as it indicates that the system has reached its equilibrium structure which is independent of the starting configuration. In addition, figures 5.2 and 5.3 clearly show that the polymer molecule can find the interface, despite starting off at an unusual distance from (and angle to) the water surface.

The density profiles produced from the various simulation data reflect the structure of the polymer/interface system. For the one-molecule simulation, the maximum density in PEO and backbone are almost coincident, and neither component extends significantly into the bulk water region. The two-molecule profile shows a higher maximum density in PEO, which is to be expected as there are twice as many PEO grafts at the surface with two molecules. Also, the PEO chains extend much further into the bulk water as relaxation of the initial brush structure occurred at a reduced rate due to the increased number of chains in the box.

The three-molecule density profile shows a feature in the PEO profile not seen

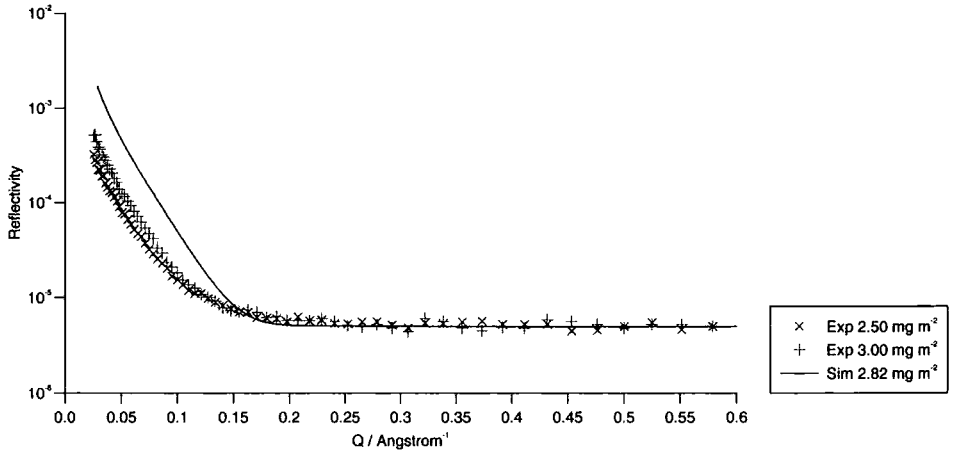

(a) deuterated on NRW

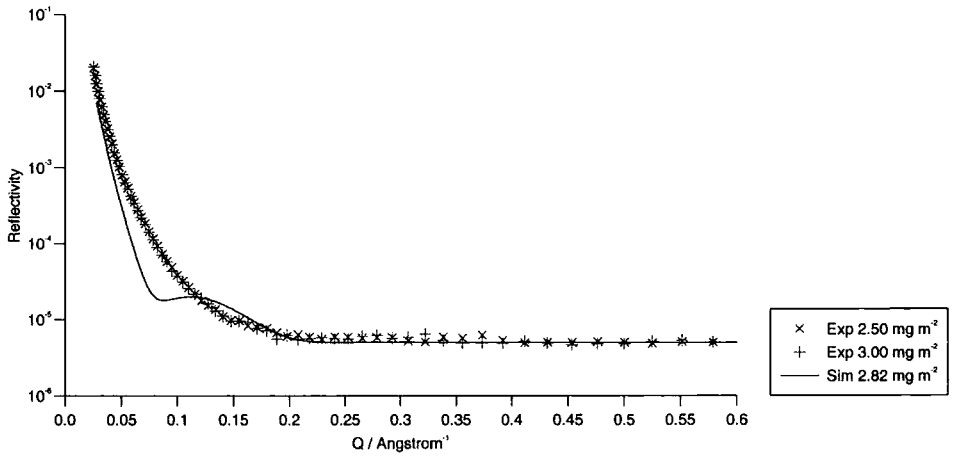

(b) protonated on D2O

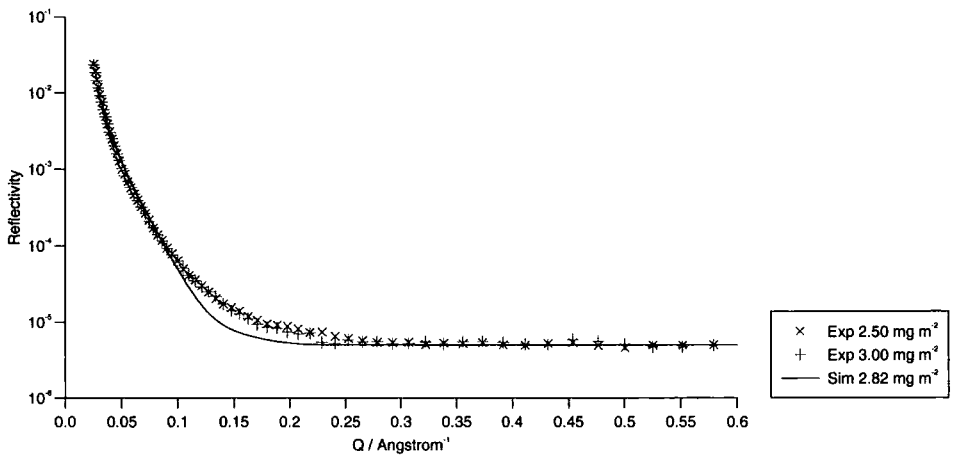

(c) deuterated on D2O

Figure 5.35: Neutron reflectivity profiles for the simulation of eight molecules at the water interface.

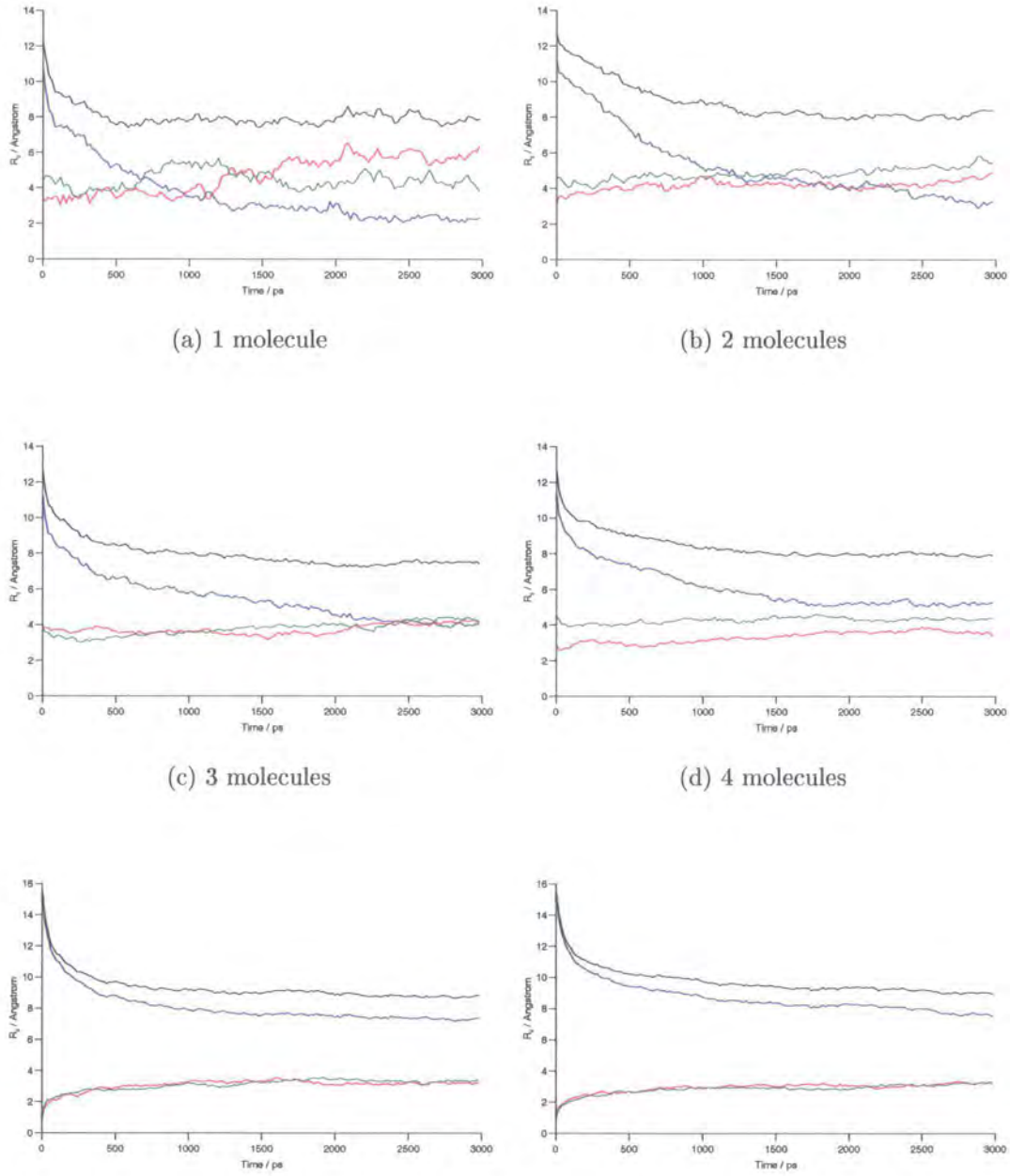

(a) 1 molecule

(b) 2 molecules

(c) 3 molecules

(d) 4 molecules

(e) 6 molecules

(f) 8 molecules

Figure 5.36: Variation in full and partial radii of gyration for the PEO chains in the amphiphilic polymer simulations. The radii of gyration are averaged across all chains in the system. R_g is shown in black, $R_{g,x}$ in red, $R_{g,y}$ in green and $R_{g,z}$ in blue.

in the previous simulations; a shoulder appears (at around z = 20-25 Å) where the rate of change in PEO density with respect to profile position differs. This shoulder becomes much more obvious in the four-molecule simulation, and a corresponding shoulder is evident in the water profile. These shoulders indicate regions where water is being excluded as the chain density increases.

The six- and eight-molecule density profiles show severe deviations from the established trend of the previous profiles. In particular, the maximum density in PEO is no longer near to the maximum density in backbone material. A distortion is obvious in the water interface, and the backbone material is no longer confined to the interfacial region as in previous simulations. Furthermore, a significant shift in the position of the water layer is evident in the latter two density profiles, indicating that the polymer layer is absorbing the water in a way similar to that seen in the earlier simulation where polymer-polymer interactions were reduced. In these latter two simulations, the reason for the observed distortions of the system is most likely the overcrowding of the simulation box. A great deal of pressure was applied, particularly in the eight-molecule system, to compress the molecules into a 76 Å by 76 Å area. In these cases, it would be of most advantage to be able to freeze the backbones and water molecules in the z-direction to prevent this distortion, and allow the system to relax somewhat before running the main data-gathering simulation. Unfortunately, due to the computational expense involved in these simulations and the bug in the constraint algorithm used by DL_POLY, there was no opportunity to attempt this.

Experimental observations indicate that the hydrophobic backbone occupies a narrow region no thicker than 5 Å at the water surface. Backbone density derived from simulation indicates that backbone density drops off to around a quarter of its maximum value at 2 Å away from this density maximum in both directions in the one molecule simulation (5 Å region overall). The corresponding region width for the four molecule simulation (same drop-off in density) is around 7 Å. These values are in good agreement with experiment. The exact thickness of the backbone layer is difficult to measure exactly, as the whole system may be undergoing slight translatory motion in the simulation box during the calculation.

5.5.2 Neutron Reflectivity

The reflectivity profiles (figures 5.15, 5.19, 5.23 and 5.27), generated from the 1-4 molecule simulations show good agreement with experiment. In particular, the one molecule simulation results fall between data for the two neighbouring experimental surface concentrations. As surface concentration increases, however, the agreement becomes slightly poorer. Despite this, the simulation data is excellent compared to the previous simulation model which neglected the solvent.[30] In the latter, the reflectivity varied by an order of magnitude at Q = 0.10 $Å^{-1}$ between experiment and simulation for a surface concentration of 1.5 mg m^{-2}. In the current study, there is a much smaller difference in reflectivity for this surface concentration (figure 5.27), indicating the current fully atomistic model is superior.

Plotting both simulated and experimental reflectivity profiles side by side (figure 5.37) allows analysis of the trends within the data. It is encouraging to note that the trend of increasing reflectivity with surface concentration seen experimentally is reproduced by the simulations. This trend is only to be expected, since the concentration of deuterium atoms (the only significantly reflecting species in the system) increases with surface concentration.

Plotting the difference in reflectivity between the protonated and deuterated species on D_2O (literally $R_D - R_H$) can show whether this system is behaving like its experimental counterpart. Figure 5.38 shows such a plot, and is in agreement with experimental observations suggesting that the protonated PEO chains result in a reduced concentration of deuterium atoms in the system, and therefore reduced reflectivity. Deuterated PEO has a scattering length density extremely close to that of D_2O, so the only real difference in reflectivity between this system and pure D_2O is the protonated polynorbornene backbone. Once again, the expected trend is reproduced by the simulations. The effect of isotopic substitution on reflectivity becomes more intense with increasing surface concentration of amphiphile on D_2O.

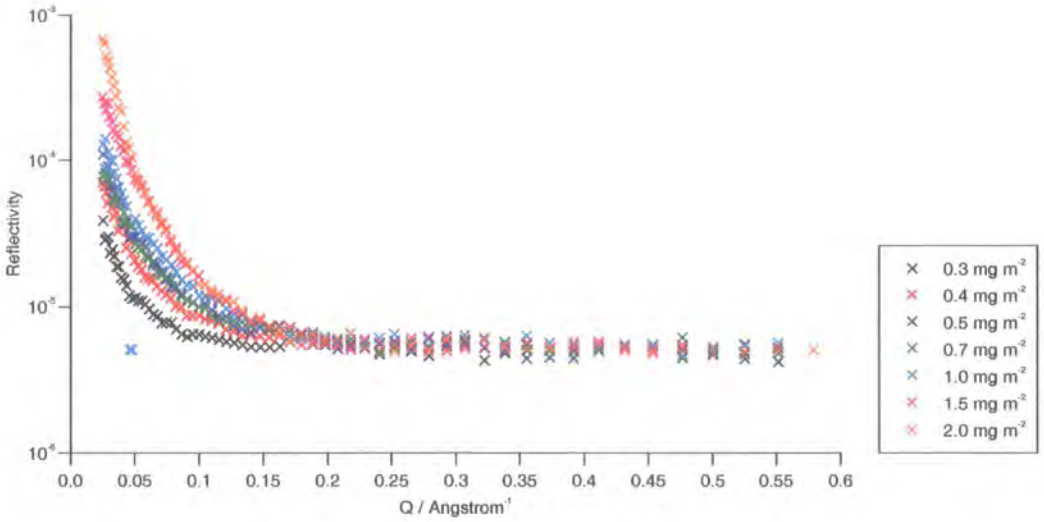

(a) experimental

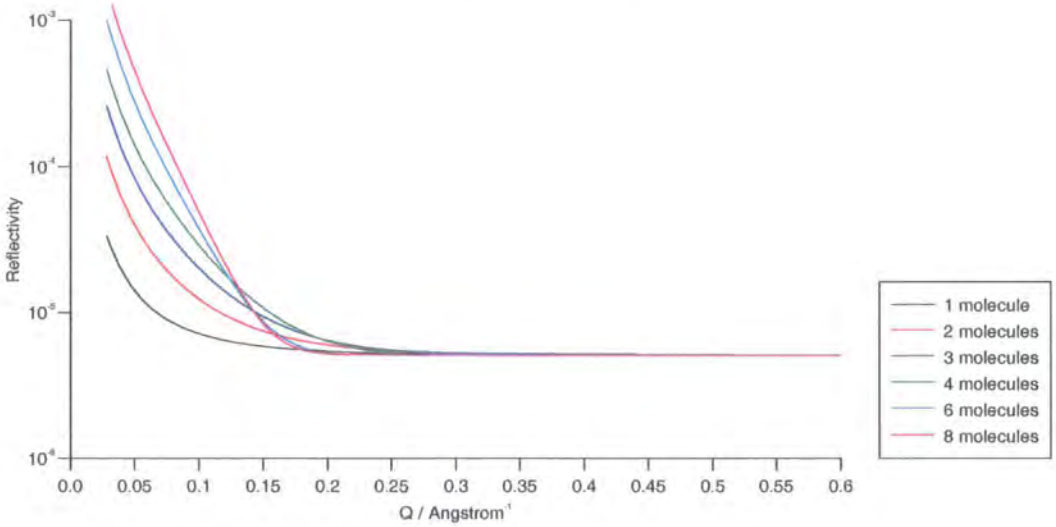

(b) simulated

Figure 5.37: Experimental and simulated reflectivity profiles for deuterated PEO on NRW. Plots are compared over the surface concentration range spanned by the simulations.

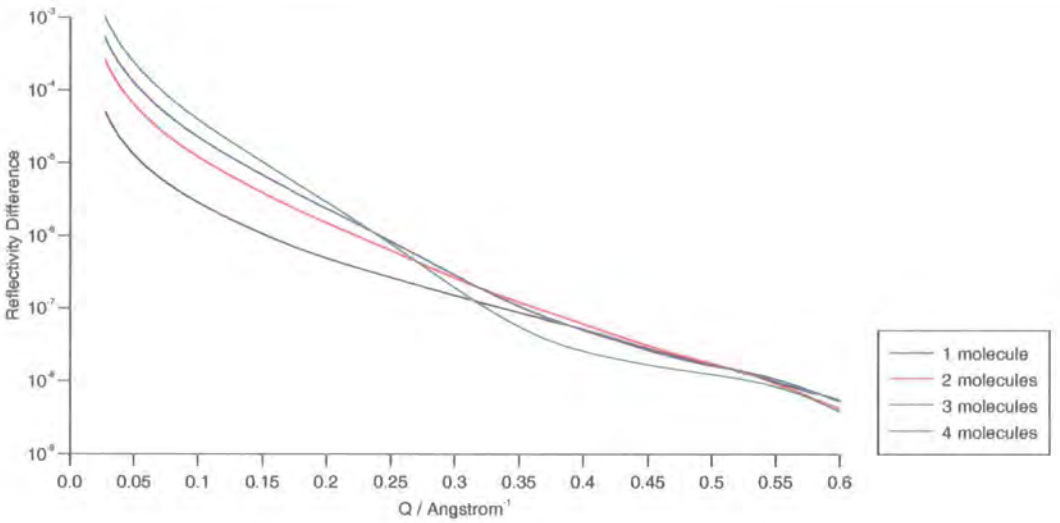

Figure 5.38: Difference in reflectivity between the protonated and deuterated species on D_2O.

5.5.3 Radii of Gyration

Figure 5.36 shows that the one, two, three and four molecule simulations all start off with the PEO radius of gyration around 12 Å. This is unsurprising since all four of these simulations were initiated with virtually identical conformations in the polymer molecules. The six and eight molecule simulations have larger radii of gyration (15 Å) as additional compression (and therefore PEO chain extension) was required to force the molecules into a satisfactorily sized simulation box. In all cases, $R_{g,z}$ starts off significantly larger than $R_{g,x}$ and $R_{g,y}$ which is only to be expected, again due to the initial conformation of the molecule at the beginning of the simulation.

In the case of one molecule at the water surface, $R_{g,z}$ takes a lower value at the end of the simulation than $R_{g,x}$ and $R_{g,y}$, indicating that the polymer has adopted a pancake structure (backed up by figure 5.10). A smaller, but still apparent difference in these partial radii of gyration is seen in the two molecule simulation. At a surface concentration of around 1.05 mg m^{-2} (3 molecules), the three partial radii of gyration appear roughly equal, indicating a possible transition point between the pancake and brush morphologies. All higher concentrations remain within the brush regime at the end of the simulation.

The rate at which the value of $R_{g,z}$ decays reduces with increasing surface con-

centration. In the case of the one molecule simulation, the polymer has conclusively entered the pancake regime only a short time after 1.0 ns, while the two molecule system is still at the brush-pancake transition after 1.5 ns. This reduction in relaxation rate is due to the excluded volume interaction between polymer chains. In the one molecule simulation, for example, the ten PEO chains can relax more easily without hindering one another than the twenty PEO chains in the two molecule simulation. The possibility has to be considered, therefore, that even after 3.0 ns of simulation time, the polymeric systems are still not necessarily fully relaxed and equilibrated. It is unfortunately not possible to test this in the present work due to the extreme computational cost that these simulations impose. Each nanosecond of simulation time required approximately sixteen days of computer time (two processor parallel calculations) on the fastest processors available to this study.

Calculation of the radius of gyration is not limited to use with the PEO side chains; the polynorbornene backbones can also be analysed. It is found that the simulations of one, two, three and four molecules in the simulation box all give rise to $R_g \approx 18.5$ Å and $R_{g,z} \approx 1.5$-2.0 Å. The latter value corresponds well to a polymer chain lying flat in the x-y plane (i.e. at the water surface). The larger simulations show deviations from these values, with $R_g \approx 17.5$ Å for both simulations. The six and eight molecule simulations have larger values of $R_{g,z}$, reflecting the observed distortion of the backbone structures as seen in figures 5.29 and 5.33. Results for $R_{g,z}$ (table 5.3) are very consistent across the four smaller simulations. These results are in agreement with the experimental thickness of 5 Å for the backbone layer.

With increasing surface concentration, the plots of radius of gyration become smoother. This is simply because of the fact that the calculated quantity is being averaged over a larger number of chains.

5.5.4 Dihedral Angle Analysis

The qualitative nature of the dihedral angle distributions is in agreement with the DME studies, however this system shows a more extreme g/t population difference. The O-C-C-O dihedrals favour the *gauche* conformation in PEO just as in DME, only to a much greater degree (≈95% *gauche* in PEO vs. ≈70-80% *gauche* in DME).

The same applies to the C-O-C-C dihedrals whose *trans* preference in PEO is much greater (≈90% *trans* in PEO vs. ≈80% *trans* in DME).

There is also a significant difference between the conformations of internal and terminal O-C-C-O dihedrals. The latter show typically <1% *trans* population while the former have populations closer to 5%. This is quite understandable, since the terminal dihedrals are very different in nature to the internal ones. Terminal dihedrals, for example, only have a single hydrogen atom sitting on one of the oxygens, which will in turn discourage a *gauche* conformation less in terms of unfavourable interactions than a larger group. In addition, the terminal O-C-C-O dihedral has a higher average oxygen charge than its internal counterparts, and this more highly charged system could be more easily stabilised by hydrogen bonding through one or more bridging water molecules. No such noticeable difference exists between internal and terminal C-O-C-C dihedrals, because the terminal dihedral is not as different from its internal neighbours.

The rate of conformational flipping in the C-O-C-C dihedral is significantly lower than that of the O-C-C-O dihedral. This can be attributed to the fact that the O-C-C-O dihedrals can flip between the equally favoured g^- and g^+ states while the C-O-C-C dihedral is trapped between these conformations in the singly degenerate t conformation.

In his 2 ns simulation of PEO in water,[56] Tasaki notes that the chain in general, and C-C bonds in particular only undergo a very small number of conformational flips (<5). However in the current simulations of the amphiphile/interface system, the average O-C-C-O dihedral undergoes at least 25 flips (table 5.4) over the course of the final 1 ns of simulation. It is therefore reasonable to assume that it is the interactions between PEO chains that increase the rate of dihedral flipping. The conformational restrictions imposed by the tethering of PEO chains to a stationary backbone will also affect the rate of conformational change. Because of the low resolution in data collection (one snapshot every 10,000 time-steps), it is very likely that the true number of conformational flips is significantly higher, further increasing the differences between this system and the isolated PEO chain in water.

The breakdown of the PEO chains into DME-like units does not indicate any con-

formational dependence on surface concentration (table 5.5). Once again the results for the two molecule simulation are somewhat anomalous, however the remaining data are fairly consistent. The same five key conformations from DME dominate in PEO, however their ratios are quite different. The restrictions imposed by these units being bonded to one another is the most likely reason for the differences from free DME molecules. Because of the length of the chain, it becomes more difficult for a stabilising 1,5-O...H close contact (hydrogen bond) to form, resulting in a drop in *tgg'* population compared to liquid DME. The *tgt* conformation is enhanced in population, possibly due to the fact that water molecules can bridge the two oxygen atoms, forming stabilising hydrogen-bonds.

5.6 Conclusions

Atomistic simulation of a large amphiphilic molecule at a water-air interface has been carried out at a range of surface concentrations. Density profiles generated from these simulations for surface concentrations in the range 0.35-1.40 mg m^{-2} show excellent agreement with experimental studies, indicating that the PEO side chains extend further into the bulk water subphase as surface concentration increases. However, simulations at the highest surface concentrations attempted failed due to overcrowding of the simulation box. It is expected that better results could be obtained from these simulations if the molecules therein underwent a more rigorous relaxation procedure (perhaps involving the use of tethers and constrained atoms) prior to data-gathering simulations.

Density profiles have been successfully converted to scattering length density profiles, although some correction was required to account for the difference between the experimental and simulated density of water, and therefore differing scattering length densities. These latter profiles were in turn used to generate simulated neutron reflectivity plots, using the optical matrix method. The reflectivity data from simulation show excellent agreement with experiment at lower surface concentrations. Agreement at higher concentrations is significantly better than in a previous model which neglected water.[161]

Partial and full radius of gyration calculations show an increasing value for the z-direction extent of PEO, in agreement with observation and theory regarding the pancake-brush transition. Interactions between PEO chains also appear to slow the collapse of the artificially imposed brush conformation into a pancake structure. The rate of transition reduces as the concentration of PEO chains increases.

Finally, conformational distributions in the O-C-C-O and C-O-C-C dihedrals are in qualitative agreement with those in the DME molecule. The g/t ratios in PEO are more extreme, however, due to the extended length of the chains. The dominant (in population) conformations in DME (*ttt*, *tgt*, *ttg*, *tgg* and *tgg'*) are also dominant in the C-O-C-C-O-C sequences along the PEO sidechains. There is qualitative agreement between the experimental DME and simulated PEO conformational population for these sequences.

For the first time, a molecular-level picture of the behaviour of these amphiphilic systems has been produced using simulation methods. Previously, these systems could only be studied experimentally, and their structures could only be deduced through the fitting of structural parameters (layer composition and thickness) to neutron reflectivity data. It has been shown that it is possible to use molecular dynamics simulation to investigate the behaviour of the individual molecules and chains themselves. It is hoped that this technique will be used extensively in the future, in the study of a wide range of other related systems.

Chapter 6

Aqueous Poly(ethylene Oxide) Simulations

6.1 Introduction

In the previous chapter, an amphiphilic molecule was simulated at a water/air interface. Poly(ethylene oxide) (PEO) is itself an amphiphilic material that can be completely dissolved in water as well as a range of hydrophobic solvents.

Computer simulations have been extensively used to study solutions of PEO in a range of solvents including water,[56,167] benzene[57] and toluene.[168] Conformational changes as a result of instantaneous switching of solvent have been analysed,[56] as have the hydrogen-bonding properties of the aqueous solution.[167] The conformation of PEO in the melt and in water has also been looked at experimentally, using Raman spectroscopy.[169]

The work in this chapter describes a set of MD simulations that were performed on PEO in solution, to give a basis for comparison between tethered (chapter 5) and free PEO chains. In addition, four different force fields were employed, to yield insight into the applicability of each to aqueous PEO simulation.

6.2 Method

A PEO chain of structure $CH_3 - (-O - CH_2 - CH_2-)_{15} - O - CH_3$ was subject to a gas phase MD simulation, in order to encourage the initially linear chain to collapse into a random coil. Once this random coil was obtained, the PEO chain was placed in a box of TIP4P water molecules, and any overlapping water molecules were removed to ensure that the starting configuration was not too highly strained.

This initial system, composed of one PEO chain and 1711 water molecules, was subject to a very brief MD run at 0 K, in order to further relax the system and remove any remaining high-energy close-contacts. After an energetically acceptable configuration had been obtained, it was used as the starting point in four separate MD simulations. Each simulation was run under identical conditions, but each used a different force field; the four force fields used were standard OPLS-AA, Smith's DME/PEO force field[49] with appropriate polymer-water interaction parameters,[135] the fitted force field used in the amphiphilic polymer simulations (chapter 5), and the reverse-engineered force field that gave the best agreement in DME conformational populations between simulation and experiment (chapter 4).

Each simulation lasted 1,000,000 steps of 2 fs, and employed a 7 Å charge-group based cutoff. Due to the significantly smaller size of the system (compared to the simulations in chapter 5), a much smaller trajectory dumping interval of 200 steps was possible. The NpT ensemble (Hoover thermostat and barostat, both with time constants of 0.5 ps) was used to allow density fluctuations to take place and the SHAKE algorithm was once again employed to maintain bond lengths at each force field's respective equilibrium values. As each of the simulations had the same starting configuration, brief MD simulations with small time-steps were required to allow each system to adjust itself according to its own potential functions. This was particularly necessary in the case of Smith's force field, where many of the equilibrium bond lengths are different to those in the other three force fields.

Analysis of the simulation trajectories was performed using many of the same criteria as in the study in the previous chapter. Radii of gyration, conformational behaviour and density can all be calculated from these simulations. The four force fields used will be referred to as OPLS-AA, Smith, Amphiphile (fitted force field used

in previous chapter) and Engineered (reverse engineered force field from chapter 4). Analysis is based on the second half of the simulation, giving the system 1 ns of equilibration time.

6.3 Results

The starting configuration used in all four simulations is shown in figure 6.1. The ending configurations can be seen in figures 6.2, 6.3, 6.4 and 6.5.

Each of the simulated systems has a unique ending configuration, despite all sharing a common starting configuration. The simulation trajectories have clearly diverged from one another, and resulted in four quite different ending structures; this shows that the potential functions used are all sufficiently different from one another that the molecules simulated under them all follow different trajectories through phase-space.

Calculation of density has also been carried out. Results can be seen in table 6.1.

	Density / g cm $^{-3}$
OPLS-AA	0.992
Smith	0.994
Amphiphile	0.992
Engineered	0.991

Table 6.1: System density calculated for each of the four simulations.

The radius of gyration has been calculated for each of the simulations. Results are presented in figure 6.6, which shows the variation in instantaneous value across the whole simulation, as well as the run-average value during the 1 ns of data-gathering simulation.

The conformational populations of all major dihedrals in each of the four simulations has been calculated for the final 1 ns of simulation, and the results are shown in table 6.2. The conformational distribution in DME-like sequences throughout the PEO chain has also been calculated for each of the simulations (table 6.3). A more detailed analysis of the conformational transitions occurring throughout the

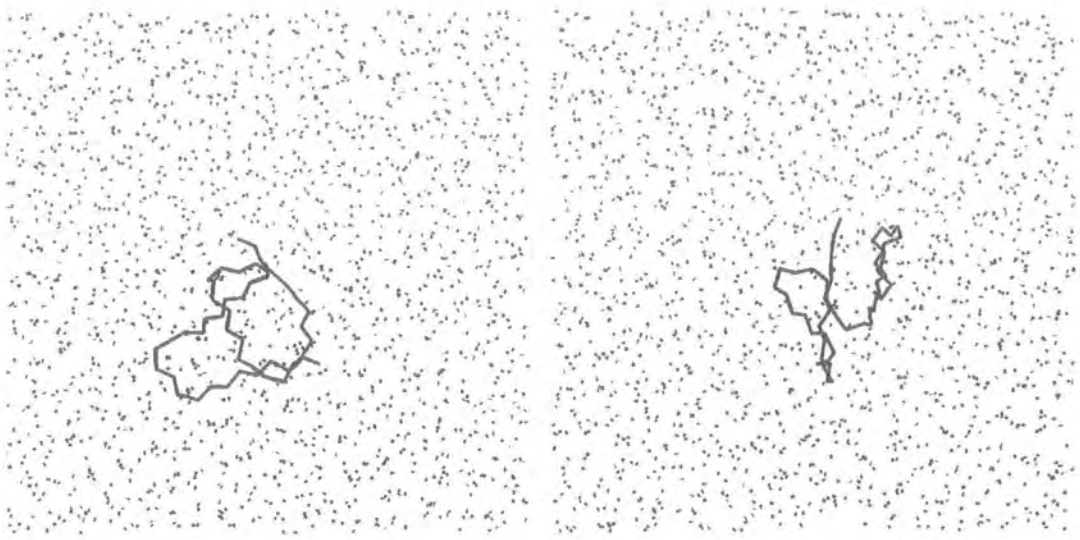

(a) x axis

(b) y axis

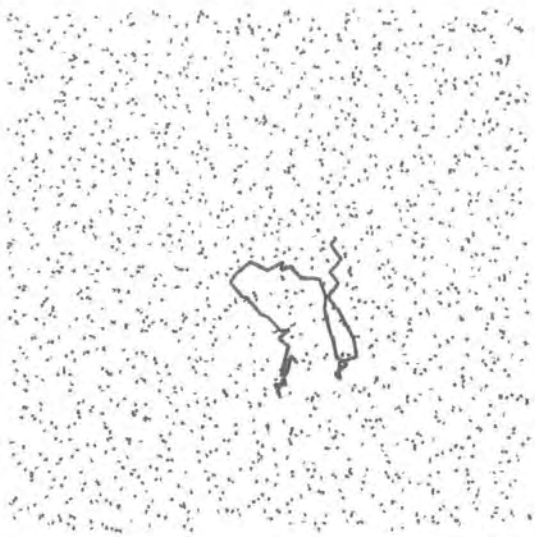

(c) z axis

Figure 6.1: Starting configuration of simulation, as viewed along the x, y and z axes. Black dots represent water molecules.

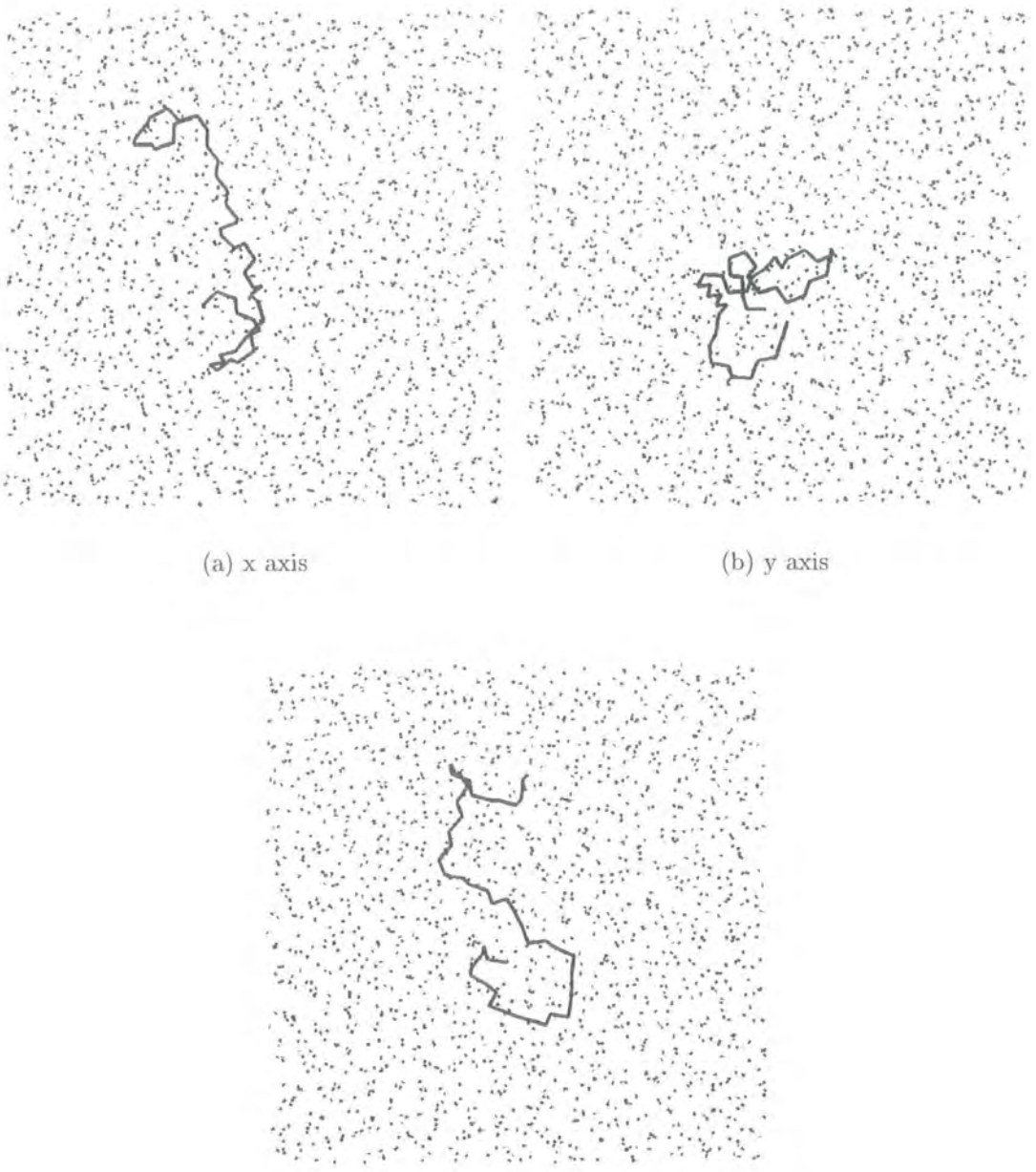

(a) x axis

(b) y axis

(c) z axis

Figure 6.2: Final configuration of simulation using OPLS-AA force field, as viewed along the x, y and z axes. Black dots represent water molecules.

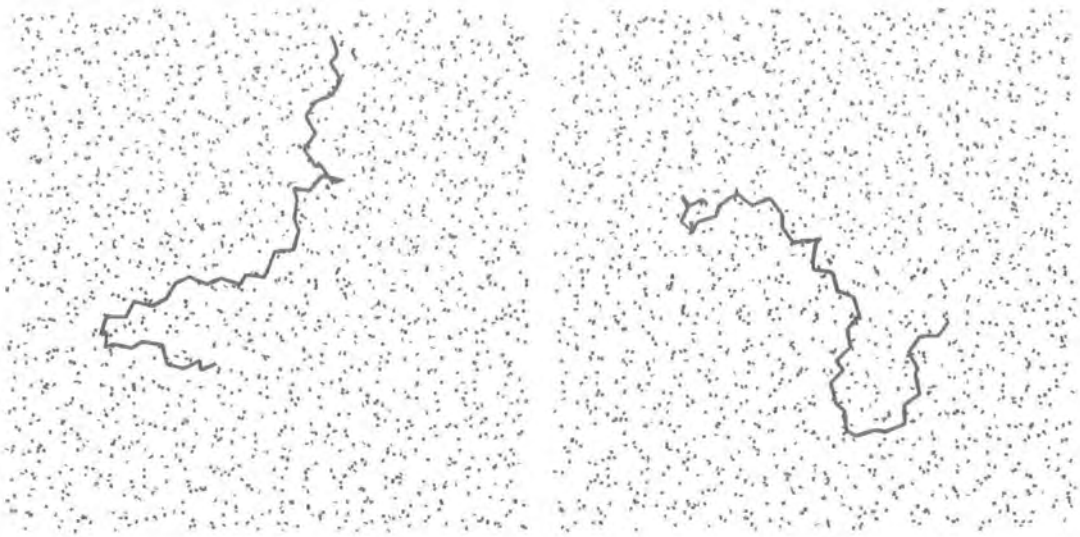

(a) x axis

(b) y axis

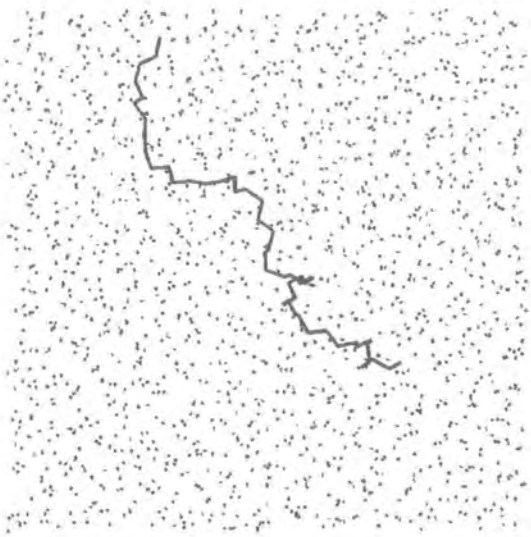

(c) z axis

Figure 6.3: Final configuration of simulation using Smith's force field, as viewed along the x, y and z axes. Black dots represent water molecules.

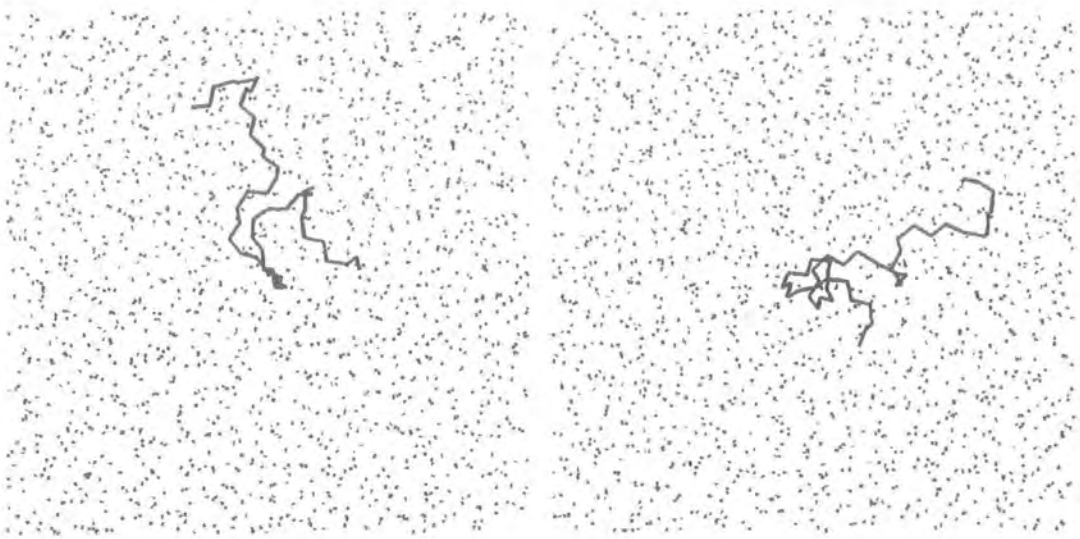

(a) x axis

(b) y axis

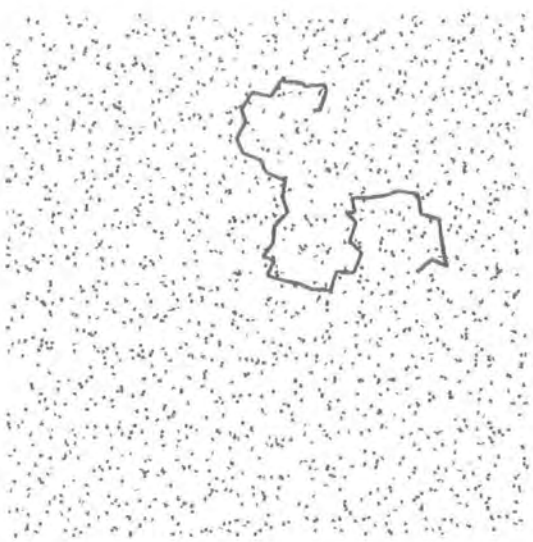

(c) z axis

Figure 6.4: Final configuration of simulation using fitted force field (also used in amphiphilic polymer simulations), as viewed along the x, y and z axes. Black dots represent water molecules.

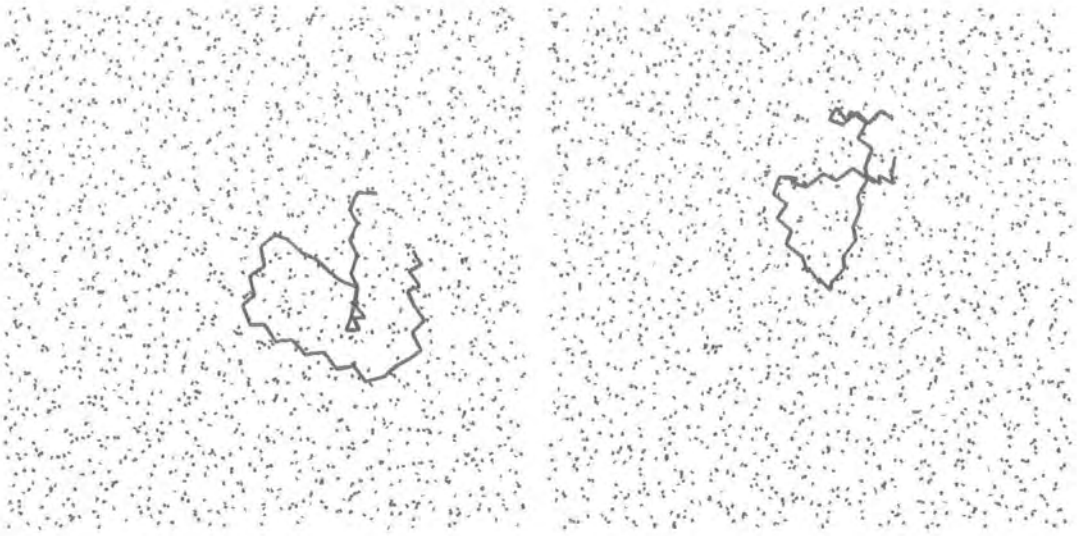

(a) x axis

(b) y axis

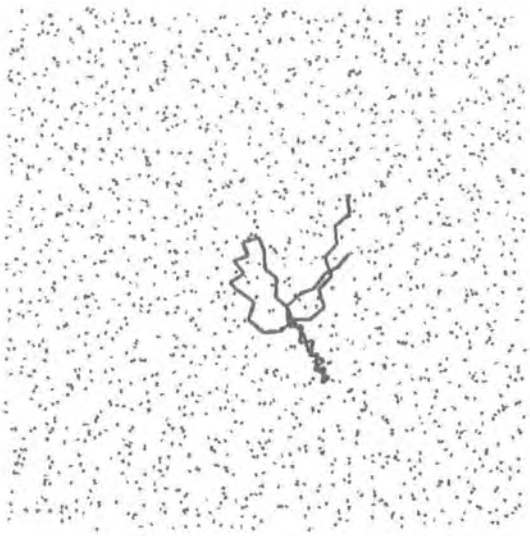

(c) z axis

Figure 6.5: Final configuration of simulation using reverse-engineered force field, as viewed along the x, y and z axes. Black dots represent water molecules.

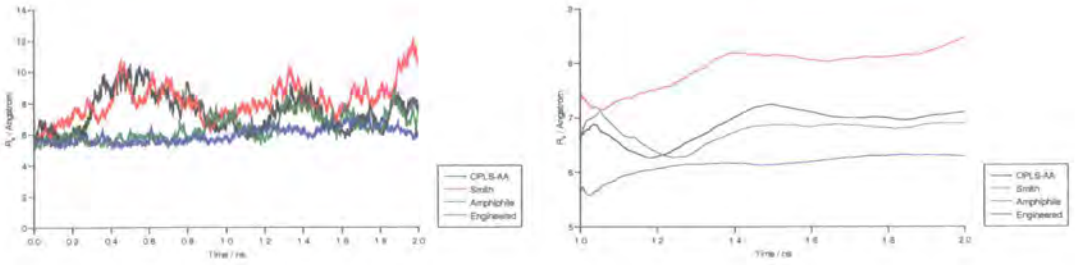

(a) instantaneous values (whole simulation)

(b) run-average values (final 1 ns)

Figure 6.6: Variation of radius of gyration over the course of the four simulations.

simulations has been performed, giving insight into which transitions in particular are most active (table 6.4).

6.4 Discussion

6.4.1 Density and General Observations

The initial configuration for all simulations involves a very compact PEO random coil. Smith's force field results in an ending configuration with a significantly extended chain. The OPLS-AA and Amphiphile force fields also show some degree of uncoiling of the chain, but the PEO chain is still fairly coiled after simulation with the Engineered force field

Since the PEO chain comprises just over 2% of the total mass of the system, it is not surprising that it has very little effect on the system density. The simulation using Smith's force field produces a marginally more dense system, but with such a tiny difference (of the order of 10^{-3} g cm $^{-3}$), that it is barely worth noting. All densities are extremely close to those obtained in chapter 3 for pure TIP4P water, and also the experimental value of 0.997 g cm $^{-3}$ for pure water.

6.4.2 Radii of Gyration

Figure 6.6 suggests that the molecules simulated under the OPLS-AA and Smith force fields are significantly more flexible than those under the other two potential

O-C-C-O	%			Flips
	g^-	t	g^+	
Internal (O)	48.77	2.16	49.07	10
Terminal (O)	35.74	6.38	57.88	15
Internal (S)	57.24	5.48	37.28	24
Terminal (S)	55.80	5.00	39.20	24
Internal (A)	54.04	2.14	43.82	5
Terminal (A)	26.00	2.18	71.82	6
Internal (E)	38.46	38.46	23.08	0
Terminal (E)	0.00	100.00	0.00	0

C-O-C-C	%			Flips
	g^-	t	g^+	
Internal (O)	6.24	89.46	4.30	35
Terminal (O)	6.18	90.08	3.74	47
Internal (S)	8.13	88.28	3.59	60
Terminal (S)	5.34	90.78	3.88	99
Internal (A)	7.63	89.56	2.81	92
Terminal (A)	4.28	89.98	5.74	168
Internal (E)	7.85	88.58	3.57	1
Terminal (E)	5.90	75.18	18.92	1

Table 6.2: Conformational distributions for each PEO simulation, calculated from the final 1 ns of simulation. *Terminal* indicates the last such dihedrals in the chain (both ends) while *internal* is the average of all other dihedrals in the chain. Force fields are O(PLS-AA), S(mith), A(mphiphile) and E(ngineered). *Flips* represents the average number of conformational transitions per dihedral type during the simulation, rounded up to the nearest integer.

Terminal	ttt	tgt	ttg	tgg	tgg'	ggg	ggg'	gg'g	gtg	gtg'
OPLS-AA	3.44	80.10	2.86	9.76	2.08	0.84	0.84	0.00	0.00	0.08
Smith	3.34	76.94	1.62	12.66	3.54	0.84	0.98	0.04	0.04	0.00
Amphiphile	1.66	82.26	0.42	10.42	4.20	0.52	0.34	0.08	0.02	0.08
Engineered	75.18	0.00	22.38	0.00	0.00	0.00	0.00	0.00	2.44	0.00

Internal	ttt	tgt	ttg	tgg	tgg'	ggg	ggg'	gg'g	gtg	gtg'
OPLS-AA	1.80	79.25	0.27	14.12	2.08	2.18	0.18	0.03	0.05	0.03
Smith	3.83	74.89	1.41	13.24	4.58	1.19	0.58	0.03	0.06	0.18
Amphiphile	1.80	78.12	0.34	11.74	6.69	0.69	0.47	0.15	0.00	0.00
Engineered	38.46	37.31	0.00	8.84	15.38	0.00	0.00	0.00	0.00	0.00

Table 6.3: Conformational distribution (%) in the sequences of internal and terminal DME-like units in the PEO chain during the final 1 ns of simulation.

O-C-C-O	$g^+ \leftrightarrow g^-$	$t \leftrightarrow g^\pm$	Total
Internal (O)	124	13	137
Terminal (O)	25	4	29
Internal (S)	0	306	306
Terminal (S)	0	48	48
Internal (A)	0	62	62
Terminal (A)	0	12	12
Internal (E)	0	0	0
Terminal (E)	0	0	0

C-O-C-C	$g^+ \leftrightarrow g^-$	$t \leftrightarrow g^\pm$	Total
Internal (O)	0	959	959
Terminal (O)	0	93	93
Internal (S)	0	1653	1653
Terminal (S)	0	198	198
Internal (A)	1	2570	2570
Terminal (A)	0	335	335
Internal (E)	0	5	5
Terminal (E)	0	2	2

Table 6.4: Breakdown of conformational transitions for the four simulations (during the final 1 ns simulation time). Transitions shown as totals, summed over all dihedrals of a particular type.

functions. The Amphiphile force field simulation first exhibits significant flexibility after 0.9 ns, and the engineered force field simulation barely shows any variation in R_g at all. The simulations of amphiphilic molecules performed in the previous chapter yielded values mainly in the range 7.5-9.0 Å for R_g. Given that the PEO grafts in the amphiphilic molecules are of comparable length to the current PEO chains, the R_g values for the OPLS-AA and Smith force field simulations agree well with the values calculated for the side-chains in the previous chapter. By around 1.0 ns, a steady increase in R_g for the Amphiphile force field is apparent. The instantaneous values of R_g are in excess of 8.0 Å towards the end of the simulation, again in good agreement with the amphiphilic polymer simulations. There appears to be very little change in the value for the Engineered force field, like the Amphiphile force field, until roughly half way through the simulation. Longer simulations are required in order to test for any long-term variations in the latter two force fields, and also to provide better convergence in the OPLS-AA and Smith simulations which seem to be competing with one another for the highest R_g value.

6.4.3 Dihedral Angle Analysis

There appears to be much less difference between terminal and internal O-C-C-O dihedral angles than in the amphiphilic polymer simulations (except in the case of the Engineered force field). In those previous simulations, the terminal O-C-C-O dihedral was significantly different to its internal counterpart, however in the current simulations, this does not seem to be the case. This can be explained once again by the unique nature of the terminal dihedrals in the PEO side chains which end in a hydroxyl group. Generally, there is good agreement between the O-C-C-O and C-O-C-C dihedral populations in the simulations of *PNB-g-PEO* (chapter 5) and the current simulations with the OPLS-AA, Smith and Amphiphile force fields.

The rate of dihedral angle flipping shows some interesting variation between the different simulations. In the *PNB-g-PEO* simulations, the O-C-C-O dihedral underwent more conformational transitions (≈25) than the C-O-C-C dihedrals (≈10 transitions). In the current simulations, the situation has reversed, and now the C-O-C-C dihedrals have significantly increased their number of transitions while the

flips in O-C-C-O dihedrals have reduced in number. This is unusual because the earlier simulations were run with a much greater trajectory-dumping interval, but the data-gathering period of 1 ns is the same length as in the current simulations. It is reasonable to assume that this effect is not arising due to the differing rates of trajectory-dumping specified in the two simulated systems, since dihedral conformation flips are expected to occur randomly but with an even distribution throughout time. Therefore it seems that tethering of the PEO chains, as well as interactions between separate chains have a significant effect on the behaviour of the internal dihedral angles.

In the *PNB-g-PEO* simulations, there appeared to be no significant difference in the number of transitions between terminal and internal dihedrals. In the aqueous PEO simulations, however, all four force fields show more frequent flipping by terminal dihedrals of the C-O-C-C type than internal ones. This would be expected, since the flipping of an internal dihedral potentially involves dragging a long chain of atoms through a dense solvent, whereas terminal C-O-C-C dihedrals have only three hydrogen atoms associated with them. There is no significant difference between the flipping rates of internal and terminal O-C-C-O dihedrals.

A more detailed analysis of these transitions (table 6.4) reveals further interesting information. The OPLS-AA force field appears to be unique in that $g^+ \leftrightarrow g^-$ transitions (that is, those across the *cis* barrier) for the O-C-C-O dihedral are far more frequent than $t \leftrightarrow g^\pm$ transitions. This can be attributed to the fact that the $g^+ \leftrightarrow g^-$ barrier is smaller in OPLS-AA (at 5.12 kcal mol^{-1}, based upon the energy of the *tct* conformation of DME) than in the other force fields (7.98 kcal mol^{-1} in Smith, 9.31 kcal mol^{-1} in Amphiphile and 9.21 kcal mol^{-1} in Engineered). The *ab initio* energy value for this barrier was around 9 kcal mol^{-1} (chapter 4). Similarly, Smith's force field has the lowest $t \leftrightarrow g^\pm$ barrier in O-C-C-O (1.93 kcal mol^{-1}), resulting in more transitions across this barrier than in the other force fields. C-O-C-C dihedrals seem to follow the same pattern, with more $t \leftrightarrow g^\pm$ flips occurring in force fields with lower barriers. The $g^+ \leftrightarrow g^-$ barrier in C-O-C-C for each of the four force fields is of roughly the same energy (around 7-8 kcal mol^{-1}).

Although the number of transitions in the O-C-C-O dihedrals is lower here than

in the amphiphile simulations (again, except the Smith simulation), they are still more frequent than those reported by Tasaki.[56] However Tasaki used a modified version of Smith's force field, and in a separate study showed that the rate of dihedral flipping is dependent on the interactions between solvent and solute.[57]

The conformational distribution in the DME-like units along the PEO chain (table 6.3) is in good agreement with that of the PEO grafts in the previous chapter. There are some slight differences, such as a heightened *ttg* population here compared to the previous study, but these are only small differences, and are possibly due to the low temporal resolution in the recorded trajectories of the amphiphilic molecules. The high *tgt* population is in good agreement with the observations of Smith[135] who suggests that this is due to the "compatibility of the DME *tgt* geometry with the structure of liquid water." In other words, the *tgt* conformation has a large dipole moment, and can therefore be stabilised by water molecules through solvation.

An experimental study using Raman spectroscopy aimed to determine the effect of hydration on conformational population in DME. This analysis[131] indicates that as concentration decreases, the *tgt* and *tgg* conformations increase in population while the *ttt* and *tgg'* conformations become less populated. The *ttg* conformation remains at a steady population. Results from the current simulations (excluding the Engineered force field) are in good agreement with these observations for all conformations except *ttg*, which reduces in population slightly from pure DME to aqueous PEO simulation. Another Raman spectroscopic experimental study, focusing on PEO solutions and melts[169] indicates that the former is dominated by the *tgt* conformation while the *tgg'* sequence makes up the majority of the latter, again in agreement with the current results, and those from chapter 5 where the PEO chains can be considered more concentrated.

6.5 Conclusions

Simulations of a PEO chain in aqueous solution have been performed using four different force fields. Densities calculated for all four simulations are very close to that of pure water.

Measurements of the radius of gyration for the various force fields indicate that the simulations have not reached convergence in this property. This is particularly apparent with the Smith force field, where a sharp increase in the running average R_g occurs in the final 0.1 ns of simulation time. Longer simulations are required to determine whether there is any difference in the true (converged) value of R_g, particularly between the OPLS-AA and Smith force fields which use different PEO-water interaction parameters. The large difference between the final averaged values for these two force fields suggests that there may be a significant difference (figure 6.6) in the converged values.

Conformational properties agree well with other experimental and computational studies, which predict that the *tgt* conformational sequence is the most common in dilute solution. There is surprisingly little difference in conformational distributions under the OPLS-AA, Smith and Amphiphile force fields, and all show very similar g/t population ratios for the O-C-C-O and C-O-C-C dihedrals. Differences in rotational energy barrier heights have affected the rates of the various conformational transitions in the different force fields. The agreement between the force fields (excluding Engineered) in conformational populations is particularly interesting as it occurs in spite a wide range of transition rates for the two dihedrals, and a difference in the relative rates of the two types of transition for the OPLS-AA force field in the O-C-C-O dihedral in particular.

Comparisons between these simulations and those presented in the previous chapter show good agreement in conformational distribution in the g/t ratios for the two dihedral types. DME-like sequences along the PEO chains are also in good agreement between both sets of simulation, for most of the key conformations. In general, the rate of dihedral flipping is lower for O-C-C-O and higher for C-O-C-C in the PEO solutions than in the amphiphile simulations (chapter 5). This could be due to the difference in concentration of PEO chains; in the amphiphile simulations there are several PEO chains in close proximity, whereas in the current simulations there is only a single molecule. Also the conformational restrictions imposed by tethering the PEO chains to the water interface via the polynorbornene backbone will have an effect on the structural behaviour of the PEO.

The only disappointment was that the Engineered force field did not perform as well as was hoped in the simulation of PEO in solution. This was most likely due to heightening of $t \leftrightarrow g^{\pm}$ barriers which were not part of the original fitting/reverse-engineering procedure.

Chapter 7

Summary and Outlook

7.1 Summary

This thesis describes the various stages involved in preparing for, and performing molecular dynamics simulations on amphiphilic polymer molecules at a water/air interface.

The first stage involved in this study was the assessment of some common water models in simulation, to test for reproducibility in physical properties of water, and computational expense. Various equilibrated water systems were set up in this stage, including bulk water for use in simulations of solutions, and a water/air interface for use with amphiphilic polymer molecules. It was found that the TIP4P water model was the most appropriate as it reproduces the physical properties of water better than SPC/E, but is less computationally expensive than TIP5P.

High-level *ab initio* optimisations and energy evaluation calculations were performed on 1,2-dimethoxyethane, a model molecule for poly(ethylene oxide), in the next stage of the project. It was found that even with the highest levels of theory and largest basis sets accessible with the available hardware, suitable convergence in conformational energies was not found. However, fitting torsion parameters to this data (all other parameters and functional forms from the OPLS-AA force field) resulted in a new force field (Amphiphile force field) with a slight improvement in conformational populations with respect to those determined experimentally. Further investigation and reverse-engineering of the force field yielded another set of

torsional parameters (Engineered force field) which gave much better agreement in conformational populations between simulation and experiment for liquid DME.

Simulations were then performed on an amphiphilic polymer at the water/air interface, spanning a range of surface concentrations, using the Amphiphile force field. Neutron reflectivity profiles generated from these simulations showed excellent agreement with experiment, particularly at low surface concentrations. With increasing surface concentration, it was found that the PEO chains undergo a transition from the pancake regime to a brush structure, again in agreement with results from previous experiments. The conformational populations of the two main-chain dihedral types in the PEO side chains were found to be in good agreement with those of free PEO in solution from previous simulations. However the rate of conformational transitions was somewhat higher than expected, indicating that the tethering of the chains to the molecular backbones at the water surface, and the increased concentration in PEO affect the conformational behaviour.

The final stage was the simulation of PEO solutions, using four different force fields. It was found that although the Engineered force field performs very well in reproducing the conformational populations of DME in the bulk liquid, it is not so good for the simulation of PEO in solution. The Smith, OPLS-AA and Amphiphile force fields all showed excellent agreement with one another in terms of conformational populations, indicating that the subtle differences in conformational energies between them may not be as important as previously suspected for PEO in solution. This agreement was observed in spite of radically different conformational transition rates between the force fields. The Engineered force field did not allow the O-C-C-O and C-O-C-C dihedrals to undergo sufficient conformational transitions to produce meaningful averages. However with a significantly longer simulation, it is possible that this force field will produce conformational averages in agreement with the other studies. The wide variation in conformational transition rates was attributed to the differences in rotational barrier heights between the four force fields, with the Engineered force field showing the highest barriers (and therefore the lowest transition rates).

For the first time, detailed atomistic simulations have been performed on an

amphiphilic polymer molecule sitting at a water-air interface. These simulations provide invaluable insight into exactly what the molecules are doing, and how they are behaving. Previous experiments have only been able to observe secondary effects, such as neutron reflectivity, and workers have had to fit this reflectivity data to structural models. In these simulations, however, the molecules themselves can be observed directly, and various data such as dihedral angle distributions and rates of relaxation can be extracted.

7.2 Outlook

Available computer time placed some restrictions on what was possible in this work. The simulations of the amphiphiles at the water interface were found to converge more slowly (with respect to the radius of gyration) as surface concentration increased. These systems would therefore benefit from longer simulation times to ensure that equilibrium has been reached. In addition, the simulations at highest surface concentrations failed to produce adequate results due to a bad starting configuration. More time invested in setting up these systems may allow these more crowded simulations to be performed correctly. Also, by setting up individual water interfaces of varying dimensions, it is possible to tailor a simulation specifically to any experimentally studied surface concentration, making comparisons more convenient.

Other related systems can also be studied using simulation methods. For example, experimental studies have been performed on a graft copolymer at the PEO solution/air interface.[170] Experiments have been performed also on a variant of the molecule studied in the current work, with hydrophobic groups capping the PEO side chains.[171] Differences in the behaviour of the two systems could be studied using free energy perturbation calculations, for example.

The behaviour of a methacrylate/PEO copolymer at the water/air interface has been looked at previously,[172] as has the structure of an amphiphilic diblock copolymer.[173] Applicability and success of simulation methods in these systems can be assessed by comparing simulation results to those obtained experimentally.

As more computer time becomes available, the detail in which one can study these systems will increase significantly. Further development in force fields may produce an energy function capable of reproducing the conformational populations and behaviour of both DME and PEO, in the gas, liquid and solution phases. Finally, continued development in computer power should allow simulation times to be lengthened in the near future. Faster simulations will facilitate comparison with experiment for those systems where equilibration times are currently too long to allow good data to be obtained.

References

[1] F. W. Billmeyer. *Textbook of Polymer Science*. John Wiley and Sons, Singapore (1984).

[2] M. E. Kouali, M. Salouhi, F. Labidi, M. E. Brouzi and J. M. Vergnaud, Polymers and Polymer Composites **11**, 301 (2003).

[3] L. Colombo, S. Busetti, A. DiPasquale and B. Miani, Kautschuk Gummi Kunststoffe **46**, 458 (1993).

[4] R. Engehausen, A. Rawlinson and J. Trimbach, Kautschuk Gummi Kunststoffe **54**, 528 (2001).

[5] A. Breitenbach, K. F. Pistel and T. Kissel, Polymer **41**, 4781 (2000).

[6] A. Malzert, F. Boury, P. Saulnier, J. P. Benoit and J. E. Proust, Langmuir **16**, 1861 (2000).

[7] Q. Cai, Y. L. Zhao, J. Z. Bei, F. Xi and S. G. Wang, Biomacromolecules **4**, 828 (2003).

[8] G. J. Fleer, M. A. C. Stuart, J. M. H. M. Scheutjens, T. Cosgrove and B. Vincent. *Polymers at Interfaces*. Chapman and Hall, London (1993).

[9] R. A. L. Jones and R. W. Richards. *Polymers at Surfaces and Interfaces*. Cambridge University Press (1999).

[10] J. Klein, Journal of Physics-Condensed Matter **12**, A19 (2000).

[11] Z. Z. Zhang, Q. J. Xue, W. M. Liu and W. C. Shen, Journal of Applied Polymer Science **76**, 1240 (2000).

[12] R. Tadmor, J. Janik, J. Klein and L. J. Fetters, Phys. Rev. Lett. **91**, 115503 (2003).

[13] L. Leger, E. Raphael and H. Hervet, Adv. Poly. Sci. **138**, 185 (1999).

[14] J. B. Kim, H. J. Yun, Y. G. Kwon and B. W. Lee, Polymer **41**, 8035 (2000).

[15] G. Allegra, G. Raos and C. Manassero, J. Chem. Phys. **119**, 9295 (2003).

[16] R. B. Dabke, A. Dhanabalan, S. Major, S. S. Talwar, R. Lal and A. Q. Contractor, Thin Solid Films **335**, 203 (1998).

[17] D. Xie, Y. D. Jiang, W. Pan, D. Li, Z. M. Wu and Y. R. Li, Sensors and Actuators B-Chemical **81**, 158 (2002).

[18] I. Szleifer, Europhys. Lett. **44**, 721 (1998).

[19] J. T. E. Cook and R. W. Richards, European Physical Journal E **8**, 111 (2002).

[20] B. Guckenbiehl, M. Stamm and T. Springer, Physica B **198**, 127 (1994).

[21] J. Penfold and R. K. Thomas, J. Phys.: Condens. Matter **2**, 1369 (1990).

[22] J. Penfold, R. M. Richardson, A. Zarbakhsh, J. R. P. Webster, D. G. Bucknall, A. R. Rennie, R. A. L. Jones, T. Cosgrove, R. K. Thomas, J. S. Higgins, P. D. I. Fletcher, E. Dickinson, S. J. Roser, I. A. McLure, A. R. Hillman, R. W. Richards, E. J. Staples, A. N. Burgess, E. A. Simister and J. W. White, J. Chem. Soc. Faraday Trans. **93**, 3899 (1997).

[23] J. A. Hunt and N. Cowlam, J. Non-Cryst. Solids **156**, 812 (1993).

[24] M. M. Neilson, J. Bowers, E. Manzanares-Papayanopoulos, J. R. Howse, M. C. Vergara-Gutierrez, P. J. Clements, A. N. Burgess and I. A. McLure, Phys. Chem. Chem. Phys. **1**, 4635 (1999).

[25] Y. Y. Huang, G. P. Felcher and S. S. P. Parkin, J. Magn. Magn. Mater. **99**, L31 (1991).

[26] F. Canet, C. Bellouard, S. Mangin, C. Chatelain, C. Senet, R. Siebrecht, V. Leiner and M. Piecuch, Euro. Phys. J. B **34**, 381 (2003).

[27] S. Rivillon, M. G. Munoz, F. Monroy, F. Ortega and R. G. Rubio, Macromolecules **36**, 4068 (2003).

[28] S. K. Peace, R. W. Richards and N. Williams, Langmuir **14**, 667 (1998).

[29] M. Goldmann, P. Nassoy and F. Rondelez, Physica A **200**, 688 (1993).

[30] A. F. Miller. Ph.D. thesis, University of Durham (2000).

[31] A. F. Miller, R. W. Richards and J. R. P. Webster, Macromolecules **33**, 7618 (2000).

[32] A. F. Miller, R. W. Richards and J. R. P. Webster, Macromolecules **34**, 8361 (2001).

[33] N. Metropolis and S. Ulam, J. Am. Stat. Ass. **44**, 335 (1949).

[34] N. Metropolis, A. W. Rosenbluth, M. N. Rosenbluth, A. H. Teller and E. Teller, J. Chem. Phys. **21**, 1087 (1953).

[35] W. W. Wood and F. R. Parker, J. Chem. Phys. **27**, 720 (1957).

[36] B. J. Alder and T. E. Wainwright, J. Chem. Phys. **27**, 1208 (1957).

[37] B. J. Alder and T. E. Wainwright, J. Chem. Phys. **31**, 459 (1959).

[38] A. Rahman, Phys. Rev. **136A**, 405 (1964).

[39] D. J. Earl, J. Ilnytskyi and M. R. Wilson, Mol. Phys. **99**, 1719 (2001).

[40] M. R. Wilson, J. M. Ilnytskyi and L. M. Stimson, J. Chem. Phys. **119**, 3509 (2001).

[41] D. L. Cheung, S. J. Clark and M. R. Wilson, Chem. Phys. Lett. **356**, 140 (2002).

[42] F. Guillaume, J. P. Ryckaert, V. Rodriguez, L. G. MacDowell, P. Girard and A. J. Dianoux, Phase Transitions **76**, 823 (2003).

[43] K. Sugio and H. Fukushima, Solid State Phenomena **93**, 381 (2003).

[44] J. Ram and P. A. Egelstaff, Physics and Chemistry of Liquids **14**, 29 (1984).

[45] W. L. Jorgensen, D. S. Maxwell and J. Tirado-Rives, J. Am. Chem. Soc. **118**, 11225 (1996).

[46] N. L. Allinger, Y. H. Yuh and J. H. Lii, J. Am. Chem. Soc. **111**, 8551 (1989).

[47] J. H. Lii and N. L. Allinger, J. Phys. Org. Chem. **7**, 591 (1994).

[48] N. A. McDonald and W. L. Jorgensen, J. Phys. Chem. B **102**, 8049 (1998).

[49] G. D. Smith, R. L. Jaffe and D. Y. Yoon, J. Phys. Chem. **97**, 12752 (1993).

[50] G. D. Smith, O. Borodin and D. Bedrov, J. Phys. Chem. A **102**, 10318 (1998).

[51] P. Dauber-Osguthorpe, V. A. Roberts, D. J. Osguthorpe, J. Wolff, M. Genesy and A. T. Hagler, Proteins: Structure Function and Genetics **4**, 31 (1988).

[52] S. J. Weiner, P. A. Kollman, D. A. Case, U. C. Singh, C. Ghio, G. Alagona, S. Profeta and P. J. Weiner, J. Am. Chem. Soc. **106**, 765 (1984).

[53] S. J. Weiner, P. A. Kollman, D. T. Nguyen and D. A. Case, J. Comput. Chem. **7**, 230 (1986).

[54] S. Barlow, A. L. Rohl, S. G. Shi, C. M. Freeman and D. O'Hare, J. Am. Chem. Soc **118**, 7578 (1996).

[55] M. Born and T. V. Karman, Physik. Z. **13**, 297 (1912).

[56] K. Tasaki, J. Am. Chem. Soc. **118**, 8459 (1996).

[57] K. Tasaki, Macromolecules **29**, 8922 (1996).

[58] G. D. Smith, D. Y. Yoon, R. L. Jaffe, R. H. Colby, R. Krishnamoorti and L. J. Fetters, Macromolecules **29**, 3462 (1996).

[59] O. Borodin and G. D. Smith, J. Phys. Chem. B **104**, 8017 (2000).

[60] B. A. Ferreira, F. Muller-Plathe, A. T. Bernardes and W. B. D. Almeida, Solid State Ionics **147**, 361 (2002).

[61] B. Nick and U. W. Suter, Computational and Theoretical Polymer Science **11**, 49 (2001).

[62] E. Kucukpinar and P. Doruker, Polymer **44**, 3607 (2003).

[63] W. K. Kim and W. L. Mattice, Macromolecules **31**, 9337 (1998).

[64] A. Stroobants, H. N. W. Lekkerkerker and D. Frenkel, Phys. Rev. Lett. **57**, 1452 (1986).

[65] J. G. Gay and B. J. Berne, J. Chem. Phys. **74**, 3316 (1981).

[66] D. Andrienko, G. Germano and M. P. Allen, Phys. Rev. E **63**, 041701 (2001).

[67] F. T. Wall and F. Mandel, J. Chem. Phys. **63**, 4592 (1975).

[68] H. Fried and K. Binder, J. Chem. Phys. **94**, 8349 (1991).

[69] I. Carmesin and K. Kremer, Macromolecules **21**, 2819 (1988).

[70] K. Hagita and H. Takano, J. Phys. Soc. Jap. **72**, 1824 (2003).

[71] K. Hagita and H. Takano, J. Phys. Soc. Jap. **68**, 401 (1999).

[72] P. Y. Lai and E. B. Zhulina, Macromolecules **25**, 5201 (1992).

[73] M. Wittkop, T. Holzl, S. Kreitmeier and D. Goritz, Journal of Non-Crystalline Solids **201**, 199 (1996).

[74] M. Rubinstein, Phys. Rev. Lett. **59**, 1946 (1987).

[75] A. van Heukelum and G. T. Barkema, J. Chem. Phys. **119**, 8197 (2003).

[76] W. Bruns and R. Bansal, J. Chem. Phys. **75**, 5149 (1981).

[77] A. Milchev and K. Binder, Macromolecules **29**, 343 (1996).

[78] R. Rzehak and W. Zimmermann, Phys. Rev. E **68**, 021804 (2003).

[79] P. J. Hoogerbrugge and J. M. V. A. Koelman, Europhys. Lett. **19**, 155 (1992).

[80] J. M. V. A. Koelman and P. J. Hoogerbrugge, Europhys. Lett. **21**, 363 (1993).

[81] R. D. Groot, T. J. Madden and D. J. Tildesley, J. Chem. Phys. **110**, 9739 (1999).

[82] H. J. C. Berendsen, J. P. M. Postma, W. F. van Gunsteren and J. Hermans. In B. Pullman, editor, *Intermolecular Forces*, page 331. Reidel, Dordrecht, Holland (1981).

[83] V. P. Sokhan and D. J. Tildesley, Mol. Phys. **92**, 625 (1997).

[84] H. Kuhn and H. Rehage, Phys. Chem. Chem. Phys. **2**, 1023 (2000).

[85] A. R. van Buuren, S. J. Marrink and H. J. C. Berendsen, Colloids and Surfaces A **102**, 143 (1995).

[86] A. R. van Buuren, S. J. Marrink and H. J. C. Berendsen, J. Phys. Chem. **97**, 9206 (1993).

[87] T. Somasundaram, R. M. Lynden-Bell and C. H. Patterson, Phys. Chem. Chem. Phys. **1**, 143 (1999).

[88] T. Somasundaram, M. in het Panhuis, R. M. Lynden-Bell and C. H. Patterson, J. Chem. Phys. **111**, 2190 (1999).

[89] W. L. Jorgensen and C. Jensen, J. Comp. Chem. **19**, 1179 (1998).

[90] J. D. Bernal and R. H. Fowler, J. Chem. Phys. **1**, 515 (1933).

[91] H. J. C. Berendsen, J. R. Grigera and T. P. Straatsma, J. Phys. Chem. **91**, 6269 (1987).

[92] W. L. Jorgensen, J. Chandrasekhar, J. D. Madura, R. W. Impey and M. L. Klein, J. Chem. Phys. **79**, 926 (1983).

[93] M. W. Mahoney and W. L. Jorgensen, J. Chem. Phys. **112**, 8910 (2000).

[94] S. B. Zhu, S. Singh and G. W. Robinson, J. Chem. Phys. **95**, 2791 (1991).

[95] I. M. Svishchev, P. G. Kusalik, J. Wang and R. J. Boyd, J. Chem. Phys. **105**, 4742 (1996).

[96] K. Kiyohara, K. E. Gubbins and A. Z. Panagiotopoulos, Mol. Phys. **94**, 803 (1998).

[97] Y. L. Yeh, C. Zhang, H. Held, A. M. Mebel, X. Wei, S. H. Lin and Y. R. Shen, J. Chem. Phys. **114**, 1837 (2001).

[98] P. Auffinger and D. L. Beveridge, Chem. Phys. Lett. **234**, 413 (1995).

[99] A. Ben-Naim and F. H. Stillinger. In R. A. Horne, editor, *Structure and Transport Processes in Water and Aqueous Solutions*, page 295. Wiley-Interscience, New York (1972).

[100] J. A. Barker and R. O. Watts, Chem. Phys. Lett. **3**, 144 (1969).

[101] A. Rahman and F. H. Stillinger, J. Chem. Phys. **55**, 3336 (1971).

[102] H. Saint-Martin, C. Medinas-Lianos and I. Ortega-Blake, J. Chem. Phys. **93**, 6448 (1990).

[103] U. Niesar, G. Corongiu, E. Clementi, G. R. Kneller and D. K. Bhattacharya, J. Phys. Chem. **94**, 7949 (1990).

[104] G. Corongiu, Int. J. Quantum Chem. **42**, 1209 (1992).

[105] J. R. Errington and A. Z. Panagiotopoulos, J. Phys. Chem. B **102**, 7470 (1998).

[106] P. Barnes, J. L. Finney, J. D. Nicholas and J. E. Quinn, Nature **282**, 459 (1979).

[107] M. Sprik, J. Phys. Chem. **95**, 2283 (1991).

[108] B. Guillot, J. Mol. Liq. **101**, 219 (2002).

[109] J. R. Reimers, R. O. Watts and M. L. Klein, Chem. Phys. **64**, 95 (1982).

[110] K. Toukan and A. Rahman, Phys. Rev. B **31**, 2643 (1985).

[111] S. B. Zhu, S. Yao, J. B. Zhu, S. Singh and G. W. Robinson, J. Phys. Chem. **95**, 6211 (1991).

[112] S. W. Rick, S. J. Stuart and B. J. Berne, J. Chem. Phys. **101**, 6141 (1994).

[113] P. Ahlstrom, A. Wallqvist, S. Engstrom and B. Jonsson, Mol. Phys. **68**, 563 (1989).

[114] F. H. Stillinger and A. Rahman, J. Chem. Phys. **60**, 1545 (1974).

[115] T. Head-Gordon and F. H. Stillinger, J. Chem. Phys. **98**, 3313 (1993).

[116] W. L. Jorgensen, J. Am. Chem. Soc. **103**, 335 (1981).

[117] W. L. Jorgensen, J. Chem. Phys. **77**, 4156 (1982).

[118] K. Laasonen, M. Sprik, M. Parrinello and R. Car, J. Chem. Phys. **99**, 9080 (1993).

[119] M. Sprik, J. Hutter and M. Parrinello, J. Chem. Phys. **105**, 1142 (1996).

[120] P. L. Silvestrelli and M. Parrinello, J. Chem. Phys. **111**, 3572 (1999).

[121] R. D. Broadbent and G. W. Neilson, J. Chem. Phys. **100**, 7543 (1994).

[122] E. J. W. Wensink, A. C. Hoffmann, P. J. van Maaren and D. van der Spoel, J. Chem. Phys. **119**, 7308 (2003).

[123] E. Hawlicka and D. Swiatla-Wojcik, Chem. Phys. **232**, 361 (1998).

[124] A. Trokhymchuk and J. Alejandre, J. Chem. Phys. **111**, 8510 (1999).

[125] T. R. Forester and W. Smith, DL_POLY_2.0 is a package of molecular simulation routines written by W. Smith and T. R. Forester, copyright The Council for the Central Laboratory of the Research Councils, Daresbury Laboratory at Daresbury, Nr. Warrington (1996). .

[126] P. Ewald, Ann. Phys. **64**, 253 (1921).

[127] M. Lisal, J. Kolafa and I. Nezbeda, J. Chem. Phys. **117**, 8892 (2002).

[128] Y. Ogawa, M. Ohta, M. Sakakibara, H. Matsuura, I. Harada and T. Shimanouchi, Bull. Chem. Soc. Jap. **50**, 650 (1977).

[129] E. E. Astrup, Acta Chim. Scand. A **33**, 655 (1979).

[130] H. Yoshida, T. Tanaka and H. Matsuura, Chem. Lett. **8**, 637 (1996).

[131] N. Goutev, K. Ohno and H. Matsuura, J. Phys. Chem. A **104**, 9226 (2000).

[132] K. Inomata and A. Abe, J. Phys. Chem. **96**, 7934 (1992).

[133] H. Yoshida, I. Kaneko, H. Matsuura, Y. Ogawa and M. Tasumi, Chem. Phys. Lett. **196**, 601 (1992).

[134] D. Bedrov, O. Borodin and G. D. Smith, J. Phys. Chem. B **102**, 5683 (1998).

[135] D. Bedrov, M. Pekny and G. D. Smith, J. Phys. Chem. B **102**, 996 (1998).

[136] D. Bedrov and G. D. Smith, J. Chem. Phys. **109**, 8118 (1998).

[137] G. D. Smith and D. Bedrov, Macromolecules **35**, 5712 (2002).

[138] H. Yoshida and H. Matsuura, J. Phys. Chem. A **102**, 2691 (1998).

[139] M. A. Murcko and R. A. DiPaola, J. Am. Chem. Soc. **114**, 10010 (1992).

[140] D. Bedrov and G. D. Smith, J. Phys. Chem. B **103**, 3791 (1999).

[141] T. Arikawa, N. Tajima, S. Tsuzuki, K. Tanabe and T. Hirano, Journal of Molecular Structure (Theochem) **339**, 115 (1995).

[142] G. D. Smith, R. L. Jaffe and D. Y. Yoon, J. Am. Chem. Soc **117**, 530 (1995).

[143] H. Liu, F. Muller-Plathe and W. F. van Gunsteren, J. Chem. Phys. **102**, 1722 (1995).

[144] D. J. Williams and K. B. Hall, J. Phys. Chem. **100**, 8224 (1996).

[145] R. L. Jaffe, G. D. Smith and D. Y. Yoon, J. Phys. Chem. **97**, 12745 (1993).

[146] B. Ganguly and B. Fuchs, J. Org. Chem. **65**, 558 (2000).

[147] O. Engkvist, G. Karlstrom and P. O. Widmark, Chem. Phys. Lett **265**, 19 (1997).

[148] N. C. Craig, A. Chen, K. H. Suh, S. Klee, G. C. Mellau, B. P. Winnewisser and M. Winnewisser, J. Phys. Chem. A **101**, 9302 (1997).

[149] K. M. Marstokk and H. Mollendal, Acta Chimica Scandinavica **50**, 875 (1996).

[150] P. J. Flory. *Statistical Mechanics of Chain Molecules.* Wiley (1969).

[151] M. J. Frisch, G. W. Trucks, H. B. Schlegel, G. E. Scuseria, M. A. Robb, J. R. Cheeseman, V. G. Zakrzewski, J. A. M. Jr., R. E. Stratmann, J. C. Burant, S. Dapprich, J. M. Millam, A. D. Daniels, K. N. Kudin, M. C. Strain, O. Farkas, J. Tomasi, V. Barone, M. Cossi, R. Cammi, B. Mennucci, C. Pomelli, C. Adamo, S. Clifford, J. Ochterski, G. A. Petersson, P. Y. Ayala, Q. Cui, K. Morokuma, D. K. Malick, A. D. Rabuck, K. Raghavachari, J. B. Foresman, J. Cioslowski, J. V. Ortiz, A. G. Baboul, B. B. Stefanov, G. Liu, A. Liashenko, P. Piskorz, I. Komaromi, R. Gomperts, R. L. Martin, D. J. Fox, T. Keith, M. A. Al-Laham, C. Y. Peng, A. Nanayakkara, M. Challacombe, P. M. W. Gill, B. Johnson, W. Chen, M. W. Wong, J. L. Andres, C. Gonzalez, M. Head-Gordon, E. S. Replogle and J. A. Pople, Gaussian, Inc., Pittsburgh PA (1998).

[152] D. J. Tozer, Chem. Phys. Lett. **308**, 160 (1999).

[153] N. L. Allinger, J. T. Fermann, W. D. Allen and H. F. Schaefer, J. Chem. Phys. **106**, 5143 (1997).

[154] A. Salam and M. S. Deleuze, J. Chem. Phys. **116**, 1296 (2002).

[155] D. L. Cheung, S. J. Clark and M. R. Wilson, Phys. Rev. E **65**, 051709 (2002).

[156] H. Tanaka and K. Nakanishi, Fluid Phase Equilibria **83**, 77 (1993).

[157] A. Pohorille and I. Benjamin, J. Phys. Chem. **97**, 2664 (1993).

[158] S. Karaborni, Langmuir **9**, 1334 (1993).

[159] D. Duchs and F. Schmid, Journal of Physics-Condensed Matter **13**, 4853 (1993).

[160] H. H. Pan, H. R. Li, D. X. Liu and S. J. Han, Mol. Sim. **29**, 797 (2003).

[161] A. F. Miller, M. R. Wilson, M. J. Cook and R. W. Richards, Mol. Phys. **101**, 1131 (2003).

[162] M. Born and E. Wolf. *Principles of Optics*. Pergamon (1980).

[163] F. Abeles, Ann. de Physique **3**, 504 (1948).

[164] O. S. Heavens. *Optical Properties of Thin Films*. Butterworths (1955).

[165] T. J. H. Vlugt and B. Dunweg, J. Chem. Phys. **115**, 8731 (2001).

[166] R. A. Orwoll. In J. Brandrup, E. H. Immergut and E. A. Gralke, editors, *Polymer Handbook*. Wiley, New York, 4th edition (1999).

[167] G. D. Smith, D. Bedrov and O. Borodin, Phys. Rev. Lett. **85**, 5583 (2000).

[168] M. M. Fuson and M. D. Ediger, Macromolecules **30**, 5704 (1997).

[169] X. Z. Yang, Z. H. Su, D. C. Wu, S. L. Hsu and H. D. Stidham, Macromolecules **30**, 3796 (1997).

[170] A. F. Miller, R. W. Richards and J. R. P. Webster, J. Phys. Chem. B **107**, 6717 (2003).

[171] R. W. Richards, J. Sarica, J. R. P. Webster and S. A. Holt, Langmuir **19**, 7768 (2003).

[172] S. K. Peace, R. W. Richards, M. R. Taylor, J. R. P. Webster and N. Williams, Macromolecules **31**, 1261 (1998).

[173] J. K. Cox, K. Yu, B. Constantine, A. Eisenberg and R. B. Lennox, Langmuir **15**, 7714 (1999).

Appendix A

Conferences, Courses and Seminars Attended

A.1 Conferences

Liquid Crystal Colloids

Sheffield Hallam University, UK, 24th April, 2002

CCP5 Summer School on Molecular Simulation

King's College London, UK, 8th-16th July, 2002

CCP5 Annual Conference: Advances in Simulations of Molecules and Materials

Durham University, UK, 9th-12th September, 2002

New Challenges in Computational Chemistry

Imperial College, London, UK, 11th April, 2003

Young Materials Modellers Forum

Daresbury Laboratory, UK, 15th May, 2003

International School of Liquid Crystals 10th Workshop: Computational

Methods for Polymers and Liquid Crystalline Polymers

Erice, Sicily, Italy, 16th-22nd July, 2003

A.2 Courses

FORTRAN Programming

Information Technology Service, University of Durham

Diffraction and Scattering Methods

Department of Chemistry, University of Durham

Practical Spectroscopy

Department of Chemistry, University of Durham

A.3 Seminars

Recent Developments in Organic LED Technology: Organolanthanide Phosphors

Dr. V. Christou, 11th October, 2000

Science, Art and Drug Discovery: a Personal Perspective

Dr. S. F. Campbell, 25th October, 2000

Label-Free Detection of Interfacial Chemistry in Scanning Microprobe and Biosensor Formats

Prof. M. Thompson, 1st November, 2000

Cosmic: a Universal, DNA-Based Language for Communicating with Aliens and Other Intelligent Lifeforms

Dr. J. P. L. Cox, 8th November, 2000

Synthesis of Novel Dendrimers and Hyperbranched Polymers

Dr. W. Hayes, 22nd November, 2000

Dual Activation Approaches to Electroanalysis: Ultrasound, Microwaves and Laser Activation

Prof. R. Compton, 6th December, 2000

The Mechanism of Swelling and Diffusion in Polymer Hydrogels Studied by NMR Methods

Dr. A. Whittaker, 11th January, 2001

Chemical Integrated Circuits: Organic Synthesis and Analysis on a Small Scale

Dr. A. deMello, 24th January, 2001

Liquid Crystals of All Shapes and Sizes

Prof. R. Richardson, 21st February, 2001

Modelling Meso- and Molecular Scale Interactions in Polymeric Systems

Prof. A. Balazs, 28th February, 2001

The Effect of Flexibility on the Phase Diagram of Simple Molecular Models

Dr. C. Vega, 30th April, 2001

Escapades with Arenes and Transition Metals: from Laser Spectroscopy to Synthetic Applications

Prof. R. Perutz, 2nd May, 2001

Conjugated Rigid-Rods as Multifunctional Materials: Applications in Photonics and Molecular and Nanoscale Electronics

Prof. T. Marder, 14th June, 2001

Towards Accurate *ab Initio* Electronic Structure for Large Molecules

Prof. P. Knowles, 17th October, 2001

Supermolecular Liquid Crystals, Multipodes and Dendrimers

Prof. J. Goodby, 14th November, 2001

Laser Probing the Gas Phase Chemistry Involved in Diamond Chemical Vapour Deposition

Prof. M. Ashfold, 6th March, 2002

Simple and Complex Fluids Under Extreme Confinement

Prof. J. Klein, 20th March, 2002

Covalent Effects in "Ionic" Systems

Dr. P. Madden, 8th May, 2002

Introducing Soft Nanotechnology

Prof. A. Ryan, 19th February, 2003

Exchange and Correlation in Atoms and Molecules

Prof. N. C. Handy, 20th March, 2003